Bandlimited Optical Intensity Modulation Under Average and Peak Power Constraints

BANDLIMITED OPTICAL INTENSITY MODULATION UNDER AVERAGE AND PEAK POWER CONSTRAINTS

BY

DINGCHEN ZHANG, B.Sc., M.Eng

A THESIS

SUBMITTED TO THE DEPARTMENT OF ELECTRICAL & COMPUTER ENGINEERING

AND THE SCHOOL OF GRADUATE STUDIES

OF MCMASTER UNIVERSITY

IN PARTIAL FULFILMENT OF THE REQUIREMENTS

FOR THE DEGREE OF

MASTER OF APPLIED SCIENCE

Master of Applied Science (2016)   McMaster University

(Electrical & Computer Engineering)   Hamilton, Ontario, Canada

TITLE: Bandlimited Optical Intensity Modulation Under Average and Peak Power Constraints

AUTHOR: Dingchen Zhang

                         B.Sc., (Electrical Engineering),

                         M.Eng., (Electrical Engineering),

                         Fudan University, Shanghai, China

SUPERVISOR: Dr. Steve Hranilovic

NUMBER OF PAGES: xxi, 106

ii

Dedication

I dedicate my thesis work to my family. A specially feeling of gratitude to my loving spouse, Ting Zhang whose words of encouragement and push for tenacity rising in my ears. My parents have never left my side. They all are very special to support me throughout the process.

Abstract

Bandlimited optical intensity channels, arising in applications such as indoor infrared communications and visible light communications (VLC), require that all signals satisfy a bandwidth constraint as well as average, peak and non-negative amplitude constraints. However, the signaling designed for conventional radio frequency (RF) electrical channels cannot be applied directly, since they take energy constraints into consideration instead of amplitude constraints. In addition, conventional transmission techniques optimized for broad-band optical channels such as fiber optics, terrestrial/satellite-to-satellite free-space optical (FSO) communications are typically not bandwidth efficient.

In this thesis, a two-dimensional signal space for bandlimited optical intensity channels is presented. A novel feature of this model is that the non-negativity and peak amplitude constraints are relaxed. The signal space parameterizes the likelihood of a negative or peak amplitude excursions in the output. Although the intensity channel only supports non-negative amplitudes, the impact of clipping on system performance is shown to be negligible if the likelihood of negative amplitude excursion is small enough. For a given signal space, a tractable approximation approach using a finite series is applied to accurately compute the likelihood of clipping under average and peak optical power constraints. The uncoded asymptotic optical power and

spectral efficiencies using two-dimensional lattice constellations are computed. The Monte-Carlo (MC) simulation results show that for a given average or peak optical power, schemes designed in the presented signal space haver higher spectral efficiency than M-ary pulse amplitude modulation (PAM) using previously established techniques.

Acknowledgements

First and foremost, I would like to express my sincere thanks to my supervisor, Dr. Steve Hranilovic, for his productive advices, useful discussions and invaluable guidance. I learned from him how to solve problems independently. It also gives me great pleasure to acknowledge him for his generous support and encouragement both in life and research during my study at McMaster University.

Also I want to show my gratitude to Dr. Jun Chen, Dr. Shiva Kumar, and Dr. Tim Davidson for their valuable suggestions, encouraged words, and insightful comments as well on my project. In addition, I would like to thank Dr. Jim Reilly, Dr. Terence Todd, and Dr. Aleksandar Jeremic to provide me opportunity to work as teaching assistant with them and obtain soft skills on communication and organization.

My thankfulness also goes to those administrative and technical staff in the Department of Electrical and Computer Engineering for their consistent help. I would like to thank in particular Mrs. Cheryl Gies for her great help and encouragement. I will also appreciate all my colleagues in the lab: Boxiao Han, Min Lu, Eric Edwards, Ahmed Darwish, Mohammed Mossaad, Michael Taylor, and Mohamed El-Shimy, for their friendship and pleasant discussions.

Most importantly, the deepest gratitude to my wife and parents for their understanding and encouragement. They have always been the source of motivation!

Acronyms

AWGN additive white Gaussian noise

BER bit error rate

ccdf complementary cumulative distribution function

cdf cumulative distribution function

DC direct current

FSO free-space optical

IM/DD intensity-modulation direct-detection

ISI inter-symbol interference

LD laser diode

LED light emitting diode

MC Monte-Carlo

OFDM orthogonal frequency-division multiplexing

OOK On-Off keying

PAM pulse amplitude modulation

pdf probability density function

PL parametric linear

PSD power spectral density

PSK phase-shift keying

QAM quadrature amplitude modulation

RC raised-cosine

RF radio frequency

RV random varaible

SER symbol error rate

S2 squared sinc

SNR signal-to-noise ratio

VLC visible light communications

Notations

$d_{\min}$ minimum distance between any two arbitrary points in a constellation

η spectral efficiency

$\hat{\phi}_1$ maximum amplitude of $\phi_1(t)$

κ ratio of the energy of truncated basis to the energy of non-truncated basis

Λ_n N-dimensional lattice

$\mathbb{R}$ real numbers set

$\mathbb{Z}$ integers set

$\mathrm{E}[\cdot]$ statistical expectation

$\mathrm{Kurt}[\cdot]$ Pearson measure of kurtosis

$\mathrm{Skew}[\cdot]$ skewness

$\mathrm{Var}[\cdot]$ variance

μ_0 DC bias

$\mu_{i,j,k}(X,Y,Z)$ the (i,j,k) multivariate moment about the $(\mathrm{E}[X],\mathrm{E}[Y],\mathrm{E}[Z])$

$\mu_{j,k}(X, Y)$ the (j, k) bivariate moment about the $(\mathrm{E}[X], \mathrm{E}[Y])$

$\mu_n(\cdot)$ n-th central moment

N_T number of one-sided truncated lobes

Ω constellation

Ω^a constellation under average optical power constraint

Ω^p constellation under peak optical power constraint

Ω^ref baseline constellation

P_e probability of bit error

$\Phi_1(f)$ Fourier transform of $\phi_1(t)$

$\phi_1(t)$ first basis function

$\Phi_2(f)$ Fourier transform of $\phi_2(t)$

$\phi_2(t)$ second basis function

$\Pi_\varepsilon(p)$ essentially peak-limited bounding region parameterized by ε and p

$\overline{P}_\mathrm{o}$ average optical power

$\overline{P}_\mathrm{o}^\mathrm{ref}$ average optical power of baseline

$\overline{P}_\mathrm{o,gain}$ average optical power gain over baseline

$\hat{P}_\mathrm{o,gain}$ peak optical power gain over baseline

$\hat{P}_\mathrm{o}$ peak optical power

$\hat{P}_{\mathrm{o}}^{\mathrm{ref}}$ peak optical power of baseline

P_{s} probability of symbol error

$\psi(\nu)$ characteristic function of random variable

$\Psi^{\star}$ optimum shaping region in the sense of minimum average power

σ^2 variance of AWGN

θ half the apex angle

Υ_{ε} essentially non-negative admissible region parameterized by ε

ε signal space parameter

ϱ photodiode detector responsivity

$\vec{\phi}_1$ unit vector in ϕ_1 direction

A_2 two-dimensional hexagonal lattice

a_i ϕ_1 direction component of the symbol drawn from constellation during i-th symbol interval

B one-sided bandwidth

b_i ϕ_2 direction component of the symbol drawn from constellation during i-th symbol interval

C electro-optical conversion factor

$F_X(x)$ cumulative distribution function of the random variable X

$f_X(x)$ probability density function of the random variable X

$G_1(f)$ Fourier transform of $g_1(t)$

$g_1(t)$ first branch receive filter

$G_2(f)$ Fourier transform of $g_2(t)$

$g_2(t)$ second branch receive filter

$H(f)$ Fourier transform of channel response $h(t)$

$h(t)$ channel response

$I(t)$ instantaneous optical intensity

$n(t)$ channel noise

$n_{1,i}$ output sample noise after filter $g_1(t)$ at i-th symbol interval

$n_{2,i}$ output sample noise after filter $g_2(t)$ at i-th symbol interval

$n_{c,1,i}$ clipping distortion after filter $g_1(t)$ at i-th symbol interval

$n_{c,2,i}$ clipping distortion after filter $g_2(t)$ at i-th symbol interval

q variable defined as the ratio of t to symbol period T

$Q(\cdot)$ tail probability of the standard normal distribution

R residual sum

$r_1(t)$ output waveform of filter $g_1(t)$

$r_2(t)$ output waveform of filter $g_2(t)$

R_b bit rate

T symbol period

T_Nyq Nyquist sampling period

$V(\cdot)$ volumn of the region

$x(t)$ output electrical current signal

$x_\mathrm{c}^\mathrm{a}(t)$ clipped negative current excursion under average optical power constraint

$x_\mathrm{c}^\mathrm{p}(t)$ clipped current excursion under peak optical power constraint

$y(t)$ received photocurrent

$y_{1,\mathrm{i}}$ discrete output of $g_1(t)$ sampled at i-th symbol interval

$y_{2,\mathrm{i}}$ discrete output of $g_2(t)$ sampled at i-th symbol interval

Contents

List of Figures

Chapter 1

Introduction

1.1 Background

Detection methods for modulated optical signals are mostly classified into two categories: *noncoherent detection* and *coherent detection*. In coherent detection, a signal is detected using both the amplitude and phase of a carrier which also implies the usage of coherent receiver and synchronization requirement. In coherent optical applications such as long-haul optic fiber and free-space optical (FSO) links [1], the transmission system requires a narrow-band laser and an external Mach-Zehnder (MZ) modulator [2] and coherent detection can be implemented using homodyne or heterodyne downconversion by a local-oscillator laster and balanced optical receiver, followed by an electrical-domain detector [3]. Experimental optical links on coherent channels by using phase-shift keying (PSK) modulation have been investigated and realized in the past two decades [2, 4–8]. However, this type of detection has relatively high complexity.

In contrast, noncoherent detection can be implemented at lower complexity using

direct detection (DD). Intensity modulation (IM) is a technique which conveys the information by modulating the instantaneous radiated intensity of an optical source. IM/DD are widely used in many low-complexity, cost-effective optical communications links such as short-haul fiber optics [9, 10], indoor visible light communications (VLC) [11–15], in-house infrared data transmissions [16–19], free-space optical (FSO) communications [20–22], and even long-distance fiber optical links combined with orthogonal frequency-division multiplexing technique (OFDM) [23, 24].

For IM links, all emitted signals are restricted to be non-negative since intensity is a non-negative physical quantity. However, IM/DD channels are often bandwidth limited due to device limitations or multipath distortion in diffuse indoor wireless optical intensity links [19]. Although the design of signal sets for bandlimited electrical channels has been extensively studied, comparatively little has been investigated on bandlimited optical intensity signaling under average, peak and non-negativity amplitude constraints.

1.2   Previous Work

Many research has been done on the signaling design for IM/DD channels. In [25], an indoor wireless infrared communications channel model considering the non-negativity and average optical power constraints was studied. The dominant shot-noise generated at photodetector is modelled as an additive white Gaussian noise (AWGN) plus a direct current (DC) offset. Power and bandwidth efficiency of several forms of pulse-position modulation (PPM) schemes, including uncoded PPM, multiple PPM, overlapping PPM, and convolutional coded PPM, were compared and

analyzed. The trade-off between power efficiency and bandwidth efficiency were examined. In [19], physical characteristics of infrared channels including path losses and multipath response were presented. In addition, the performance of various modulation formats such as on-off keying (OOK), PPM, and subcarrier modulation in the presence of multipath distortion for short-range wireless infrared channels were discussed in detail. The use of rectangular pulse sets were studied for bandwidth-efficient signaling. A signal space model for optical intensity channels was presented in [26] and a geometric representation of non-negativity and average optical power constraints were provided. The performance of lattice code for optical IM/DD systems with AWGN were quantified for raised-quadrature amplitude modulation (QAM). Coding and shaping gain over the baseline scheme were computed. Examples of bandwidth-efficient modulation for high data-rate applications were presented. The result was extended to lattice codes in related direct-detection optical channels with amplified spontaneous emission noise in [27]. The difference is that the dominant noise considered is a form of signal-dependent noise. An N-dimensional signal space was formed by using a sequence of N time-disjoint pulses. It was shown that the ultimate shaping gain is 1.53 dB as $N \to \infty$ and can be approached when the 1-dimensional constituent constellation follows a truncated half-Gaussian distribution. Karout *et al.* proposed a novel quaternary subcarrier modulation format for IM/DD systems which is a hybrid between OOK and ternary PSK [28]. It was shown that a 0.6 dB average optical power gain over OOK can be obtained at asymptotically high signal-to-noise ratio (SNR). The scheme was also demonstrated to be more power efficient than other known formats with a spectral efficiency of 1 bit/s/Hz. The optimization of a set of M-ary (e.g. $M = 4, 8, 16$) single-subcarrier modulation formats for IM/DD systems

with and without confining them to a lattice structure was studied in [29] and a wider class of pulse sets were considered. The gain of the optimized formats over previously known formats range from 0.3 dB to 1 dB. A simplified two-dimensional signal space with reduced complexity compared to the three-dimensional formats studied in [29] was presented in [30]. It was shown that the two-dimensional formats wee good for single-wavelength optical systems since the formats have superior performance if the bandwidth is measured as 90% in-band power. In all of above studies, signals were strictly duration-limited and bandwidth was quantified by a fractional power bandwidth.

For signaling on bandlimited IM/DD channels, the squared sinc (S2) pulse was shown to be the minimum bandwidth optical intensity intersymbol interference (ISI) free Nyquist pulse and it was further shown that there is no bandlimited optical intensity root-Nyquist pulse [31]. The minimum bandwidth required was shown to be twice that of conventional electrical channels. In addition, a trade-off between bandwidth and average optical power efficiency in pulse design was quantified. In [32], non-negative OOK and 4-ary pulse amplitude modulation (PAM) for bandlimited IM/DD channels with dominant AWGN was developed using electrical Nyquist and root-Nyquist pulses with a DC bias to satisfy non-negativity constraint. A bandwidth versus average optical power efficiency trade-off was investigated. In the case of OOK with no excess bandwidth, S2 pulse has the highest power efficiency. As an extension to Tavan's work which introduces a constant bias to satisfy non-negativity constraint, a time-varying bias is added to the output to guarantee non-negativity [33]. The optimal bias was searched numerically. After pulse design, the authors showed a gain of about 0.6 dB power gain over S2 OOK with a matched filter receiver and no gain

when using a sampling receiver.

1.3 Contributions of the Thesis

A two-dimensional signal space is presented based on amplitude and derivative modulation for optical IM/DD systems in which all constructed signals are strictly bandlimited [34]. A novel feature of this model is that the strict non-negativity and peak amplitude constraints are relaxed. The probability that the resulting output amplitude is negative or exceeding the peak limitation is parameterized in the signal space [35]. The motivation for this relaxation is that even if the optical intensity channel only supports non-negative amplitudes due to devices limitation, the impact of clipping on system performance will be negligible if the clipping distortion is small enough.

Lattice codes to construct essentially non-negative and peak-limited signals for optical IM/DD channels are defined. The likelihood of negative amplitude excursion under average optical power constraint is rigorously upperbounded for a given signal space. In addition, an efficient and accurate approach to numerically compute the likelihood of clipping under average and peak amplitude constraints is applied.

Compared to previously studied schemes (e.g., [31, 32]), such relaxation of strict non-negativity and peak amplitude constraints provides more degrees of freedom per second and Monte-Carlo simulation results demonstrate that modulation based on the essentially non-negative and peak-limited signal space and optical lattice codes in the thesis has better uncoded power and spectral efficiencies.

1.4   Organization of the Thesis

The reminder of this thesis is organized as follows. The IM/DD system model is presented in Chapter 2. Chapter 3 presents the signal space model as well as a geometric representation of average and peak amplitude constraints. The lattice codes are defined and analyzed in Chapter 4.1. Upper bound of likelihood of clipping is derived and a tractable finite series approach applied to numerically compute the likelihood of clipping are discussed in Chapter 4.2. Chapter 5 presents system performance under average optical power constraint with and without added DC bias as well as under peak optical power constraint. Conclusions are drawn in Chapter 6 with some directions for future work. The derivation of first four central moments of residual sum in detail is presented in appendix.

Chapter 2

System Model

The system model including transceiver and channel is presented in this chapter. Two different channel models are defined under average and peak optical power constraints, respectively. A sub-optimal sampling receiver is designed to get estimation of transmitted symbol.

Consider the reconstruction of a finite energy bandlimited function $f(t)$ with bandwidth B in Fig.2.1. The Shannon-Nyquist Theorem states that $f(t)$ can be reconstructed from amplitude samples taken every $T_{\mathrm{Nyq}} = \frac{1}{2B}$ seconds as follow:

$$f(t) = \sum_{i=-\infty}^{\infty} f(iT_{\mathrm{Nyq}})\mathrm{sinc}(t/T_{\mathrm{Nyq}} - i)$$

where $\mathrm{sinc}(x) \triangleq \sin \pi x/(\pi x)$ is the normalized sinc function. The bandwidth constraint can be viewed as imposing a limit on the number of degrees of freedom per second which can be modulated. A generalized sampling theorem showed that $f(t)$ can be reconstructed from samples of *amplitude* and *first derivative* every $2T_{\mathrm{Nyq}}$ seconds [36, 37] which leads to the study of this thesis.

7
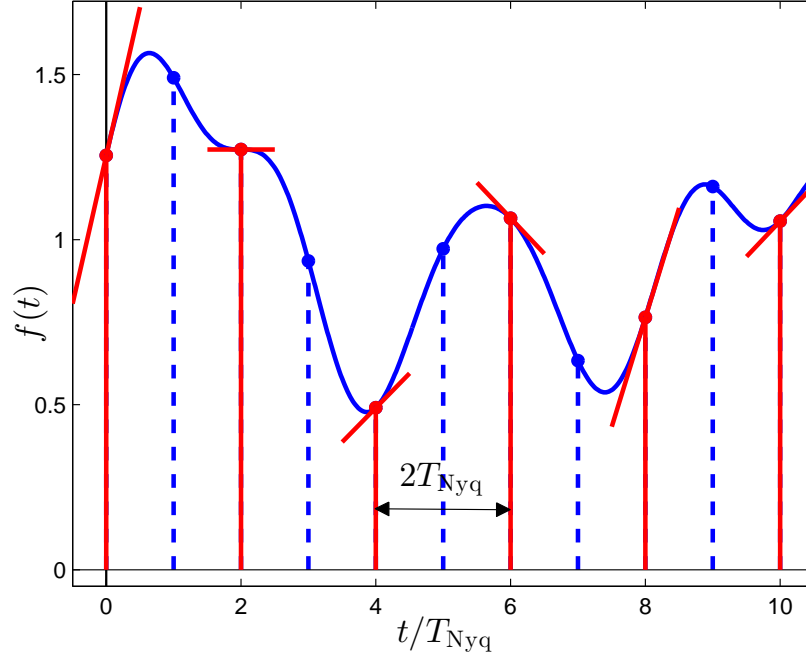
Figure 2.1: Bandlimited function $f(t)$ can be reconstructed by the amplitude samples every T_{Nyq} seconds (blue dashed) or by amplitude and first derivative samples every $2T_{\text{Nyq}}$ seconds (red solid).

As illustrated in Fig. 2.1, a bandlimited signal $f(t)$ with bandwidth B can be expressed in terms of its amplitude and derivative sampled at half the Nyquist rate [37, eq.14]

$$
\begin{aligned}
f(t) &= \sin^2 \frac{\pi t}{T} \sum_{i=-\infty}^{\infty} \frac{f(iT)}{\left(\frac{\pi t}{T} - \pi i\right)^2} + \frac{f'(iT)}{\frac{\pi}{T}\left(\frac{\pi t}{T} - \pi i\right)} \\
&= \text{sinc}^2(t/T - i) \sum_{i=-\infty}^{\infty} f(iT) + (t - iT)f'(iT) \qquad (2.1)
\end{aligned}
$$

where $T = 2T_{\text{Nyq}} = 1/B$ is the symbol period, $f(\cdot)$ and $f'(\cdot)$ are samples of amplitude and first derivative at $t = iT$, respectively. Thus to reconstruct a B-band limited signal, two basis functions are defined in terms of $\text{sinc}^2(t/T)$ and $t\text{sinc}^2(t/T)$.

2.1   Transmitter

Define two orthogonal basis functions $\phi_1(t)$ and $\phi_2(t)$ as

$$\phi_1(t) \;=\; \sqrt{\frac{2}{T}}\mathrm{sinc}^2\left(\frac{t}{T}\right) \quad, \tag{2.2}$$

$$\phi_2(t) \;=\; \sqrt{\frac{8\pi^2}{3T}}\frac{t}{T}\mathrm{sinc}^2\left(\frac{t}{T}\right) \quad. \tag{2.3}$$

Notice that $\phi_1(t)$ is even and $\phi_2(t)$ is odd. For any $i \in \mathbb{Z}$,

$$\phi_1(iT) = \begin{cases} \sqrt{\dfrac{2}{T}}, & i = 0 \quad, \\ 0, & i \neq 0 \quad. \end{cases}$$

And $\phi_1^{'}(iT) = 0, \forall i \in \mathbb{Z}$, where $\phi_1^{'}(t)$ is the first derivative of $\phi_1(t)$. Similarly, for derivative of $\phi_2(t)$

$$\phi_2^{'}(iT) = \begin{cases} \sqrt{\dfrac{8\pi^2}{3T^3}}, & i = 0 \quad, \\ 0, & i \neq 0 \quad. \end{cases}$$

And $\phi_2(iT) = 0$ for all $i \in \mathbb{Z}$. Thus, $\phi_1(t)$ and $\phi_2^{'}(t)$ satisfy the Nyquist criterion [38]. Fig 2.2 presents the waveform of $\phi_1(t)$ and $\phi_2(t)$. At each symbol instance, the derivative of $\phi_1(t)$ and the amplitude of $\phi_2(t)$ are all zeros.

Let $\Phi_1(f)$ and $\Phi_2(f)$ be the Fourier transforms of $\phi_1(t)$ and $\phi_2(t)$, respectively. It can be shown that $\phi_1(t)$ and $\phi_2(t)$ are bandlimited to $1/T$ Hz, i.e.

$$\Phi_m(f) = 0, \quad |f| > 1/T, \; m = 1, 2 \quad.$$

9
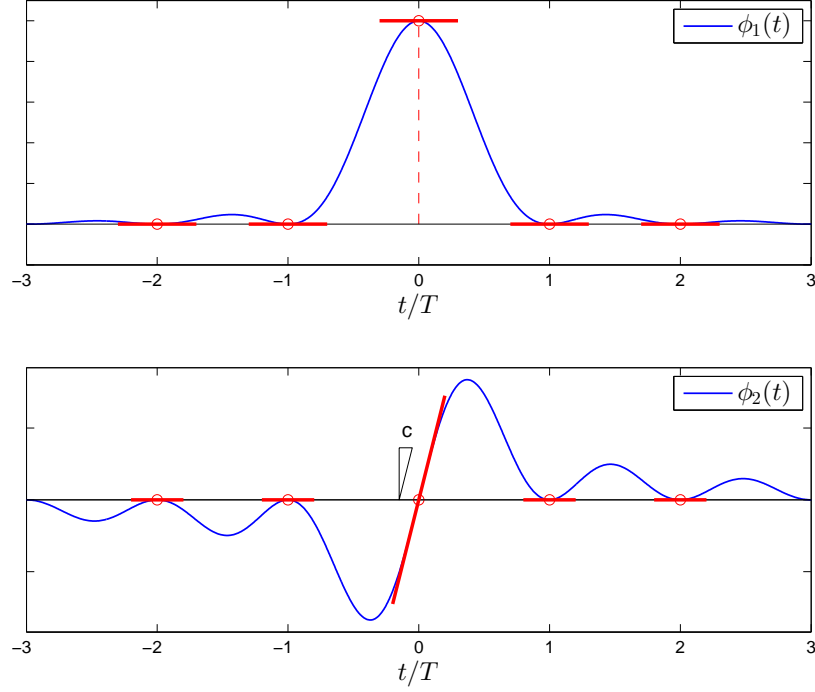
Figure 2.2: Waveforms of $\phi_1(t)$ and $\phi_2(t)$, where $\phi_2'(0) = \sqrt{8\pi^2/(3T^3)}$.

Fig. 2.3 presents the spectrum of $\Phi_1(f)$ and $\Phi_2(f)$. From (2.1), *every* bandlimited signal with one-sided bandwidth $B = 1/T$ lies in the span of the set of time shifted basis functions $\{\phi_1(t - iT)\}$ and $\{\phi_2(t - iT)\}$.

Fig. 2.4 presents the model of a baseband IM/DD system based on $\phi_1(t)$ and $\phi_2(t)$. The bandlimited electrical current signal $x(t)$ is generated as a linear combination of $\{\phi_1(t - iT)\}$ and $\{\phi_2(t - iT)\}$ and takes the form

$$x(t) = \sum_{i=-\infty}^{\infty} a_i \phi_1(t - iT) + b_i \phi_2(t - iT) \tag{2.4}$$

where $(a_i, b_i) \in \mathbb{R}^2$ are two-tuples drawn from a constellation Ω. Symbols are assumed to be independently and equiprobably drawn from Ω for each symbol period.

Since $\phi_1(t)$ and $\phi_2'(t)$ are scaled Nyquist pulses, the amplitude and derivative of
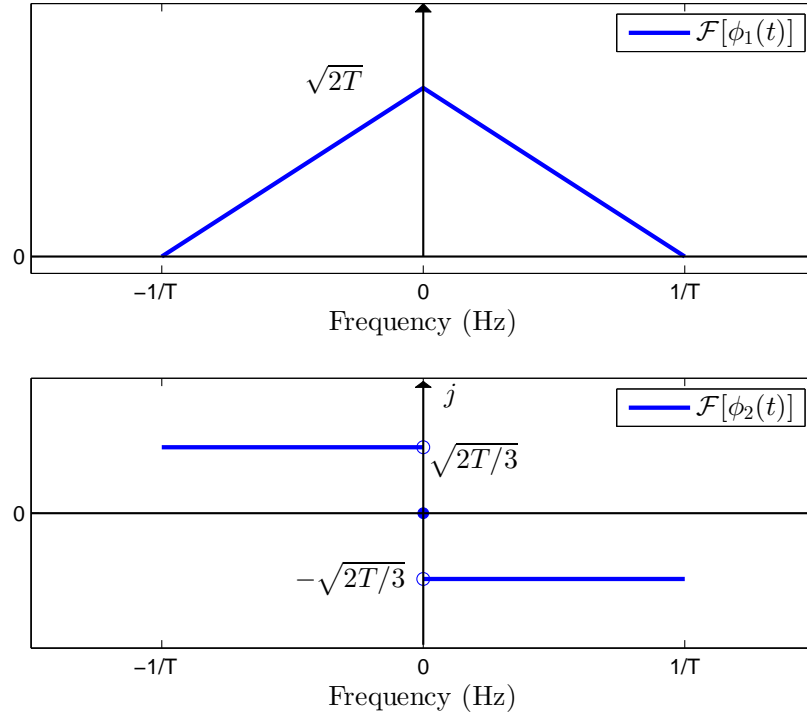
Figure 2.3: Fourier transform of the basis functions $\phi_1(t)$ and $\phi_2(t)$.

$x(t)$ at each symbol instant can be expressed as

$$
\begin{aligned}
x(t)\big|_{t=iT} &= a_i\sqrt{\frac{2}{T}} \quad, \\
\frac{d}{dt}x(t)\bigg|_{t=iT} &= b_i\sqrt{\frac{8\pi^2}{3T^3}} \quad.
\end{aligned}
$$

That is, at every symbol instant the amplitude of $x(t)$ is defined by the coefficients of $\phi_1(t-iT)$ and the derivative of $x(t)$ is fixed by coefficients of $\phi_2(t-iT)$, respectively.

In practical applications, a light emitting diode (LED) or laser diode (LD) is often used to modulate the instantaneous *optical intensity*, $I(t)$ in Fig. 2.4, which is defined as the optical power emitted per solid angle [26]. Thus the constraints on optical power can be equivalently viewed as constraints on the amplitude of $I(t)$. Clearly,
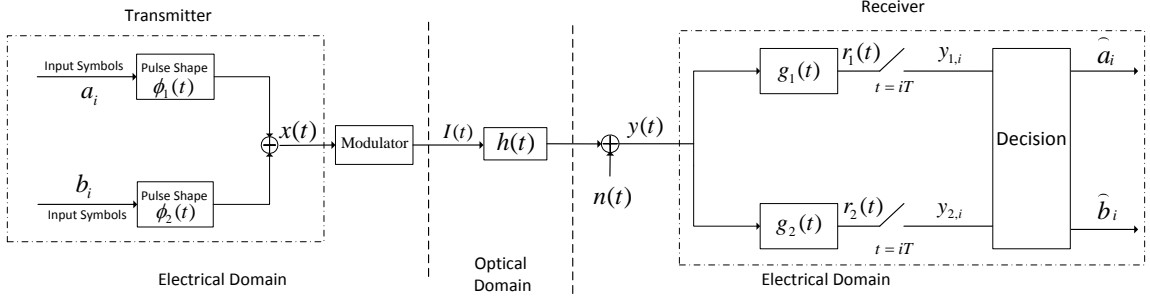
Figure 2.4: Diagram of the based IM/DD system model.

since $I(t)$ is an optical intensity, it must remain non-negative for all $t \in \mathbb{R}$. The optical intensity $I(t)$ has a nonlinear relation to the modulator input electrical current $x(t)$ due to the device limitations. The device nonlinear characteristic transfer functions of LEDs are studied in [39–42]. In addition, amplitude constraints on $I(t)$ are also be imposed for safety reasons. In this thesis, we consider two particular amplitude constraints: average and peak optical power limitations.

2.1.1 Average Optical Power Constraint

The emitted optical intensity must be non-negative and the electro-optical conversion process can be modelled as

$$
I(t) = \begin{cases}
0, & \text{if } x(t) < 0 \\
Cx(t), & \text{if } x(t) \geq 0
\end{cases} \tag{2.5}
$$

where C is the electro-optical conversion factor in units of watts per ampere [W/A]. Without loss of generality, let $C = 1$. In many applications, especially in the infrared band, the average optical power must be bounded for eye- and skin-safety concerns or to control illumination levels in VLC systems [19]. The modulator outputs zero

12

optical intensity in response to the negative current amplitude and an output optical intensity in response to non-negative current is linear. The nonlinear characteristic can be viewed equivalently as the clipping of all the negative amplitude excursion.

The average optical power is given by

$$\overline{P}_{\mathrm{o}} = \lim_{\tau \to \infty} \frac{1}{2\tau} \int_{-\tau}^{\tau} I(t)dt \quad . \tag{2.6}$$

The definition of average optical power is in contrast to the case of conventional radio frequency (RF) channels where the average emitted power is proportional to the squared amplitude. Using (2.5) and (2.4), the average optical power can be simplified as

$$
\begin{aligned}
\overline{P}_{\mathrm{o}} &= \lim_{\tau \to \infty} \frac{1}{2\tau} \int_{-\tau}^{\tau} x(t) - x_{\mathrm{c}}^{\mathrm{a}}(t) \\
&= \lim_{j \to \infty} \frac{1}{2jT} \sum_{k=-j}^{j-1} \int_{kT}^{(k+1)T} x(t)dt - \lim_{\tau \to \infty} \frac{1}{2\tau} \int_{-\tau}^{\tau} x_{\mathrm{c}}^{\mathrm{a}}(t) \\
&= \lim_{j \to \infty} \frac{1}{2j} \sum_{i=-\infty}^{\infty} a_i \overline{\phi}_1 + b_i \overline{\phi}_2 - \overline{P}_{\mathrm{o,c}}^{\mathrm{a}} \tag{2.7} \\
&= \mathrm{E}\left[a_i\right] \overline{\phi}_1 + \mathrm{E}\left[b_i\right] \overline{\phi}_2 - \overline{P}_{\mathrm{o,c}}^{\mathrm{a}} \tag{2.8} \\
&= \mathrm{E}\left[a_i\right] \overline{\phi}_1 - \overline{P}_{\mathrm{o,c}}^{\mathrm{a}} \tag{2.9}
\end{aligned}
$$

where

$$
\begin{aligned}
\overline{P}_{\mathrm{o,c}}^{\mathrm{a}} &= \lim_{\tau \to \infty} \frac{1}{2\tau} \int_{-\tau}^{\tau} x_{\mathrm{c}}^{\mathrm{a}}(t)dt \quad , \\
\overline{\phi}_1 &= \frac{1}{T} \int_{-\infty}^{\infty} \phi_1(t)dt = \sqrt{\frac{2}{T}} \quad , \\
\overline{\phi}_2 &= \frac{1}{T} \int_{-\infty}^{\infty} \phi_2(t)dt = 0 \quad .
\end{aligned}
$$

13

Notice that $x_\text{c}^\text{a}(t)$ is a non-positive signal representing any clipped negative current excursion in the amplitude of $x(t)$ which is performed by the modulator and thus $\overline{P}_\text{o,c}^\text{a}$ is the time-average of clipped amplitude. In (2.7) the infinite integral is transformed into an infinite sum, when it exists. (2.8) arises by using the strong low of large numbers since each 2-tuples (a_i, b_i) is selected independently and equiprobably. $\text{E}\left[\cdot\right]$ denotes the statistical expectation. Both $\overline{\phi}_1$ and $\overline{\phi}_2$ are constants. As in (2.9), the average optical power $\overline{P}_\text{o}$ can be represented by the constellation and the clipped component of the electrical current.

2.1.2 Peak Optical Power Constraint

In many practical optical communications systems, particularly in illumination, a constraint is placed on the peak amplitude emitted from the source. In particular, the dynamic range of the input is limited to ensure high efficacy of the luminary or to limit non-linear distortion [43]. In contrast to the case under solely average optical power constraint, the electro-optical conversion process in this case is modelled as:

$$I(t) = \begin{cases} 0, & \text{if } x(t) < 0 \\ Cx(t), & \text{if } 0 \le x(t) \le p\hat{\phi}_1 \\ p\hat{\phi}_1, & \text{if } x(t) > p\hat{\phi}_1 \end{cases} \tag{2.10}$$

where $C = 1$ without loss of generality, p is a parameter selecting the current saturation threshold of the modulator and

$$\hat{\phi}_1 = \max_{t \in \mathbb{R}} \phi_1(t) = \sqrt{\frac{2}{T}} \quad . \tag{2.11}$$

Similarly, the device input current to output intensity transfer characteristic is equivalently viewed as the clipping of all the negative amplitude excursion and the amplitude exceeding saturation level. The modulator output satisfies linearity of input over the region $[0, p\hat{\phi}_1]$.

The peak optical power is defined as the maximum possible amplitude of intensity and takes the form as

$$\hat{P}_{\text{o}} = \max_{t \in \mathbb{R}} I(t) = \max_{t \in \mathbb{R}} x(t) - x_{\text{c}}^{\text{p}}(t) \leq p\hat{\phi}_1 \tag{2.12}$$

where the maximum is imposed by channel. $x_{\text{c}}^{\text{p}}(t)$ denotes the clipped current excursion of $x(t)$ which is negative or exceeding $p\hat{\phi}_1$. Notice additionally, that the imposition of a peak amplitude constraint imposes an implicit constraint on the average optical power.

2.2 Channel

The modulator converts electrical current to optical intensity as the input of channel. The received photocurrent $y(t)$ in Fig. 2.4 can be modeled as

$$
\begin{aligned}
y(t) &= \varrho I(t) * h(t) + n(t) \\
&= \varrho(x(t) - x_{\text{c}}(t)) * h(t) + n(t) \tag{2.13}
\end{aligned}
$$

where ϱ is the photodiode detector responsivity in units of ampere per watt [A/W] which can also be set as 1 without loss of generality and $x_{\text{c}}(t)$ represents clipping distortion that is either $x_{\text{c}}^{\text{a}}(t)$ or $x_{\text{c}}^{\text{p}}(t)$ depending on the constraint imposed. The

channel response, $h(t)$, is assumed to be bandlimited and flat within the bandwidth of interest $[-1/T, 1/T]$ Hz. Let $H(f)$ be the Fourier transform of $h(t)$ and $H(f) = 1, f \in [-1/T, 1/T]$. The channel noise $n(t)$ is independent to $x(t)$ and is modelled as a zero-mean AWGN process with double-sided power spectral density (PSD) $N_0/2$ [19]. Given that $x(t)$ is bandlimited to bandwidth of the channel, $y(t)$ can be simplified as

$$y(t) = x(t) + n(t) + n_c(t) \tag{2.14}$$

where $n_c(t) = -x_c(t) * h(t)$ is the filtered clipping distortion at the receiver.

2.3   Sampling Receiver

The receiver used in this thesis is a generalized *sampling receiver* which is assumed to have ideal synchronization. As shown in Fig. 2.4, $y(t)$ passes through two receive filters $g_1(t)$ and $g_2(t)$ which are designed to detect amplitude and derivative samples of $x(t)$ at each symbol instance, respectively. The filters are defined as

$$g_1(t) = \sqrt{\frac{2}{T}} \text{sinc}\left(\frac{2t}{T}\right) \tag{2.15}$$

$$g_2(t) = \sqrt{\frac{3T}{2\pi^2}} \frac{d}{dt} \text{sinc}\left(\frac{2t}{T}\right) \tag{2.16}$$

Let $G_1(f)$ and $G_2(f)$ denote the Fourier transform of $g_1(t)$ and $g_2(t)$, respectively. Using the properties of Fourier transform [44, Chp.4], it can be shown that the two filters are bandlimited to $1/T$ Hz. Fig. 2.5 illustrates the Fourier transform of $g_1(t)$ and $g_2(t)$, where $G_1(f)$ has a rectangular spectrum and $G_2(f)$ is the scaled product of $j2\pi$ and spectrum of $d\text{sinc}(2t/T)/dt$. The energy of $G_1(f)$ and $G_2(f)$ in frequency

16
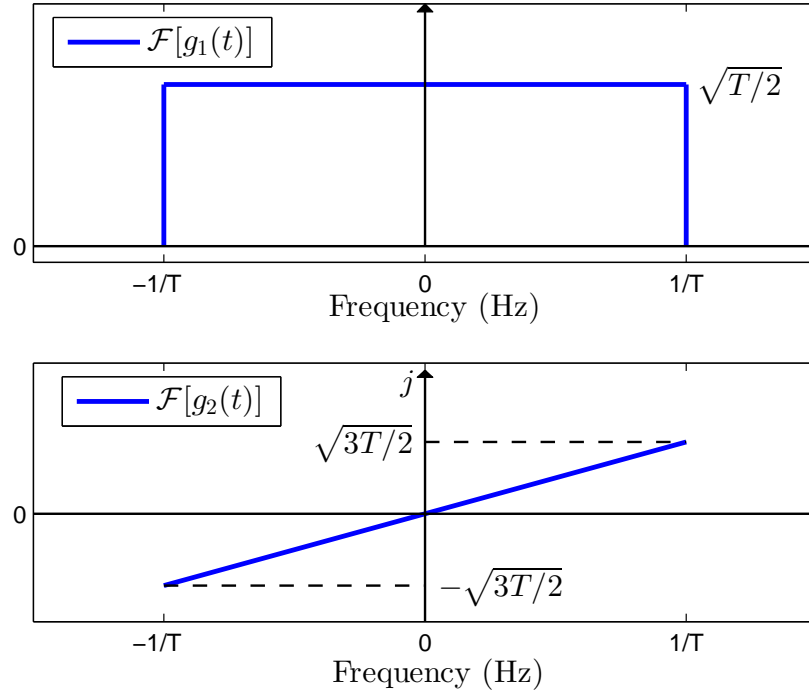
Figure 2.5: Fourier transform of the two receive filters $g_1(t)$ and $g_2(t)$.

domain can be calculated:

$$\int_{-\infty}^{\infty} |G_1(f)|^2 df = \int_{-1/T}^{1/T} \frac{T}{2} df = 1$$

$$\int_{-\infty}^{\infty} |G_2(f)|^2 df = 2 \int_{0}^{1/T} \frac{3T^3 f^2}{2} df = 1$$

From Plancherel's theorem [45–47], we have

$$\int_{-\infty}^{\infty} g_1(t) g_2^*(t) dt = \int_{-\infty}^{\infty} G_1(f) G_2^*(f) df = 0$$

since $G_1(f)$ is even and $G_2(f)$ is odd. Thus, $g_1(t)$ and $g_2(t)$ have unit energy and are orthonormal.

The Fourier transform of the filtered waveforms, i.e. $\phi_1(t) * g_1(t)$ and $\phi_2(t) * g_2(t)$,

17

are presented in Fig. 2.6. The Fourier transform of the convolution between two functions in time-domain is the product of Fourier transform of each function in frequency-domain. Thus, $\Phi_1(f)G_1(f)$ has a triangular spectrum and $\Phi_2(f)G_2(f)$ is an flipped triangular spectrum, which are both bandlimited to $1/T$ Hz. Let $P_1(f) = \Phi_1(f)G_1(f)$ and $P_2(f) = \Phi_2(f)G_2(f)$, it can be shown that $\phi_1(t)*g_1(t)$ and $\phi_2(t)*g_2(t)$ are Nyquist pulses since they satisfy the Nyquist criterion in frequency domain [48, Chp.5]:

$$\frac{1}{T}\sum_{k=-\infty}^{\infty} P_m(f - k/T) = 1, \quad m = 1, 2$$

The system is inter-symbol interference (ISI) free in a straightforward manner since $\phi_1(t) * g_1(t)\big|_{t=iT} = \delta_{i0}$ and $\phi_2(t) * g_2(t)\big|_{t=iT} = \delta_{i0}$, where δ_{kl} is the Kronecher delta function

$$\delta_{kl} = \begin{cases} 1, & \text{if } k = l \\ 0, & \text{otherwise} \end{cases}$$

On the other hand, the spectrum of $\phi_2(t) * g_1(t)$ and $\phi_1(t) * g_2(t)$ are presented in Fig. 2.7. Similarly, Let $P_3(f) = \Phi_2(f)G_1(f)$ and $P_4(f) = \Phi_1(f)G_2(f)$ as the Fourier transforms of $\phi_2(t) * g_1(t)$ and $\phi_1(t) * g_2(t)$, respectively. It can be shown that

$$\sum_{k=-\infty}^{\infty} P_m(f - k/T) = 0, \quad k = 3, 4 \quad .$$

Thus the cross-correlation of two filter branches at each symbol instant are zero since $\phi_1(t) * g_2(t)\big|_{t=iT} = 0$ and $\phi_2(t) * g_1(t)\big|_{t=iT} = 0$ for all $i \in \mathbb{Z}$.

The outputs of the filters, $r_1(t)$ and $r_2(t)$, are sampled at the symbol interval to
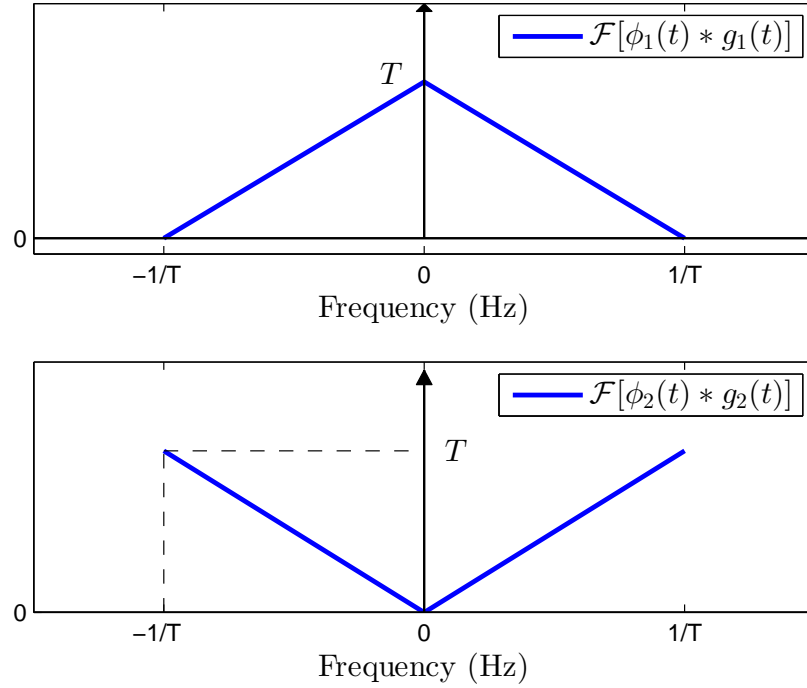
Figure 2.6: Fourier transforms of the output waveforms $\phi_1(t) * g_1(t)$ and $\phi_2(t) * g_2(t)$.

yield discrete samples $y_{1,i}$ and $y_{2,i}$, where

$$r_1(t) = y(t) * g_1(t) = \int_{-\infty}^{\infty} y(t - \tau)g_1(\tau)d\tau \quad ,$$

$$r_2(t) = y(t) * g_2(t) = \int_{-\infty}^{\infty} y(t - \tau)g_2(\tau)d\tau \quad .$$

Denote $n_{1,i}$ and $n_{2,i}$ as the output sample noises of processes $n(t) * g_1(t)$ and $n(t) * g_2(t)$ at $t = iT$, respectively. Since $g_1(t)$ and $g_2(t)$ are both linear time-invariant (LTI) systems and unit energy, and also channel noise $n(t)$ is a stationary white Gaussian process, $n_{1,i}$ and $n_{2,i}$ are both Gaussian random variables (RV) with zero-mean and variance $\sigma^2 = N_0/2$.
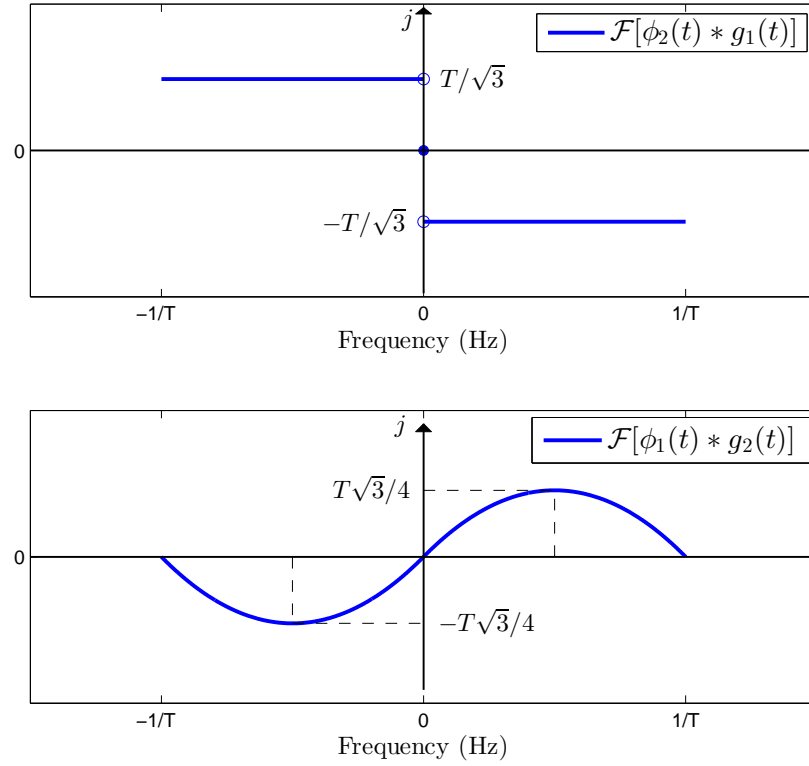
Figure 2.7: Fourier transforms of the output waveforms $\phi_2(t) * g_1(t)$ and $\phi_1(t) * g_2(t)$.

Computing the cross-correlation of $n_{1,i}$ and $n_{2,i}$ at each sampling instant:

$$
\begin{aligned}
E[n_{1,i}n_{2,i}] &= E\left[\int\int n(t_1)g_1(iT - t_1)n(t_2)g_2(iT - t_2)dt_1 dt_2\right] \\
&= \int\int E\left[n(t_1)n(t_2)\right]g_1(iT - t_1)g_2(iT - t_2)dt_1 dt_2 \\
&= \frac{N_0}{2}\int\int \delta(t_2 - t_1)g_1(iT - t_1)g_2(iT - t_2)dt_1 dt_2 \qquad (2.17) \\
&= \frac{N_0}{2}\int g_1(iT - t_1)g_2(iT - t_1)dt_1 \\
&= 0 \qquad (2.18)
\end{aligned}
$$

It shows that noise sample $n_{1,i}$ and $n_{2,i}$ are uncorrelated and thus mutually independent since they are jointly Gaussian. The (2.17) in the above equation group arises

20

by applying $E\left[n(t_1)n(t_2)\right] = \frac{N_0}{2}\delta(t_2 - t_1)$ since $n(t)$ is a wide-sense stationary (WSS) white Gaussian process. And (2.18) is derived from the orthonormal property that

$$\int g_1(iT - t_1)g_2(iT - t_1)dt_1 = -\int g_1(t)g_2(t)dt = 0 \quad .$$

The autocorrelation of $n_{1,i}$ and $n_{2,i}$ are computed to characterize the output discrete noises of the two filter branches. Denote $N(f) = N_0/2$ as the PSD of $n(t)$. The PSD of $n(t)$ through filter $g_1(t)$ and $g_2(t)$ are $N(f)|G_1(f)|^2$ and $N(f)|G_2(f)|^2$, respectively. Denote $R_{n_1}(\tau)$ and $R_{n_2}(\tau)$ as the autocorrelation of $n(t)$ through $g_1(t)$ and $g_2(t)$, respectively. Since the autocorrelation of a stochastic process is the inverse Fourier transform of its PSD,

$$\begin{aligned} R_{n_1}(t) &= \mathcal{F}^{-1}\left[N(f)|G_1(f)|^2\right] \\ &= \frac{N_0}{2}\text{sinc}\left(\frac{2t}{T}\right) \end{aligned}$$

where $\mathcal{F}^{-1}[\cdot]$ denotes the inverse Fourier transform. The autocorrelation of $n_{1,i}$ is given by

$$R_{n_1}(iT) = \begin{cases} \dfrac{N_0}{2}, & i = 0 \\ 0, & i \neq 0 \end{cases} \quad ,$$

The sequence $\{n_{1,i}\}$ is uncorrelated to each other and thus white. Similarly, the autocorrelation of $n_{2,i}$ is given by

$$\begin{aligned} R_{n_2}(iT) &= \mathcal{F}^{-1}\left[N(f)|G_2(f)|^2\right]\Big|_{t=iT} \\ &= \frac{N_0}{2}3T^3\int_0^{1/T} e^{j2\pi f iT}f^2 df \quad . \end{aligned}$$
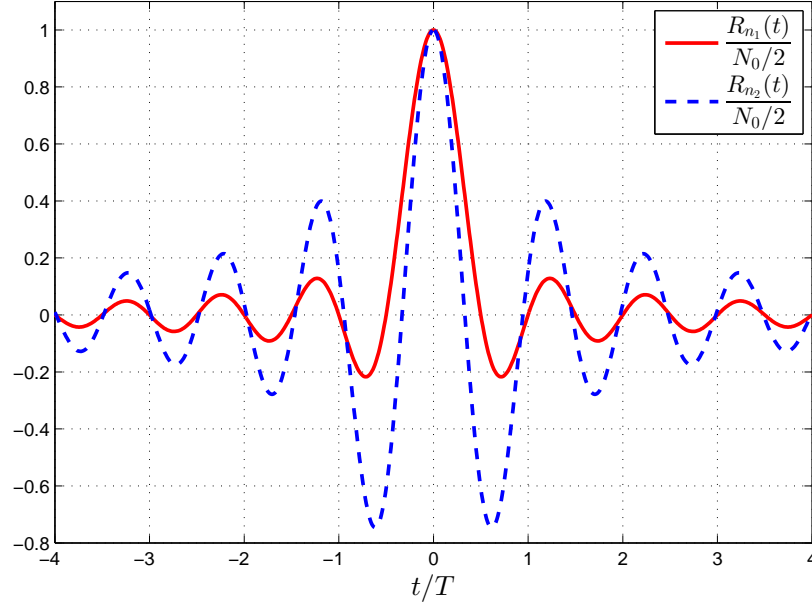
Figure 2.8: Scaled autocorrelation of $n(t)$ through filters $g_1(t)$ and $g_2(t)$ by factor $N_0/2$.

Fig. 2.8 presents the scaled autocorrelation of $n(t)$ through $g_1(t)$ and $g_2(t)$ and illustrates that sequence $\{n_{2,i}\}$ is correlated since $R_{n_2}(iT) \neq 0$ for $i \neq 0$ and thus colored noise.

The overall discrete outputs yielded by sampling at $t = iT$ can be expressed as:

$$y_{1,i} = a_i + n_{1,i} + n_{c,1,i} \tag{2.19}$$

$$y_{2,i} = b_i + n_{2,i} + n_{c,2,i} \tag{2.20}$$

where $n_{c,1,i}$ and $n_{c,2,i}$ are the sampled clipping distortions after $g_1(t)$ and $g_2(t)$, respectively. The system is impacted by clipping distortion $n_{c,1,i}$ and $n_{c,2,i}$, which depend on $x(t)$ and on the particular amplitude constraint of the channel.

In design of the receiver, the impact of clipping distortion is ignored and this assumption is shown to be good in simulation results in Chap. 5. The output sample

noises $n_{1,i}$ and $n_{2,i}$ are independent, Gaussian distributed with zero mean and variance $N_0/2$. The demodulation module is assumed to apply symbol-by-symbol maximum likelihood detection in the thesis. Thus, the receiver here is not optimal since the noise correlation of $\{n_{2,i}\}$ is ignored.

2.4   Summary

In this chapter, two orthogonal basis functions which represent the amplitude and first derivative of electrical current signal $x(t)$ are defined. The optical channel is modelled as interrupted by a signal-independent AWGN. Two input current to output intensity characteristic transfer functions under average and peak amplitude constraints are presented. Finally, a sub-optimal sampling receiver is designed based on the symbol-by-symbol maximum likelihood detection and the noise correlation of $\{n_{2,i}\}$ is ignored. Based on the two basis functions, a two-dimensional signal space under average and peak amplitude constraints will be defined in the next chapter.

Chapter 3

Essentially Non-negative and Peak-limited Signal Space

In this chapter, a signal space model for bandlimited optical intensity signals is defined by constraining a_i and b_i in (2.4). Strict non-negativity and peak amplitude constraints are, however, relaxed and the signal space parameterizes the likelihood of violating the constraints.

3.1 Essentially Non-negative Admissible Region

The non-negative amplitude constraint for optical intensity channels requires that

$$\forall t \in \mathbb{R} \quad x(t) \geq 0 \quad .$$

As $\phi_1(t)$ is a scaled minimum-bandwidth optical intensity Nyquist pulse [31], $\phi_1(t) \geq 0$ for all $t \in \mathbb{R}$. Thus $\sum_i a_i \phi_1(t - iT)$ is non-negative for all $t \in \mathbb{R}$ if $a_i \geq 0$. On the

other hand, $\phi_2(t)$ is odd and has zero average in time and necessarily assumes negative amplitudes.

For a given $\varepsilon > 0$, define a two-dimensional signal space spanned by bases $\phi_1(t)$ and $\phi_2(t)$. In [26], the *admissible region* is defined as the set of all points corresponding to non-negative signals time-limited to $t \in [0, T)$. In this thesis, the *essentially non-negative* admissible region, Υ_ε, is defined in an analogous fashion as

$$\Upsilon_\varepsilon = \left\{ (a, b) \in \mathbb{R}^2 : \min_{|t/T| \leq \frac{\sqrt{3}}{\varepsilon 2\pi}} a\phi_1(t) + b\phi_2(t) \geq 0 \right\} \tag{3.1}$$

Notice that Υ_ε contains the origin and for $\varepsilon_1 > \varepsilon_2$, $\Upsilon_{\varepsilon_2} \subset \Upsilon_{\varepsilon_1}$. In addition, Υ_ε is closed under scaling by a non-negative value and is located in the half plane $a \geq 0$.

Lemma 1. *For a fixed $\varepsilon > 0$, $(a, b) \in \Upsilon_\varepsilon$ if and only if $|b| \leq a\varepsilon$.*

Proof. Consider the symbol $s(t)$ represented by point (a, b) in the signal space,

$$s(t) = a\phi_1(t) + b\phi_2(t) = \left(a + b\frac{2\pi}{\sqrt{3}} \frac{t}{T} \right) \phi_1(t) \quad . \tag{3.2}$$

Since $\phi_1(t) \geq 0$ for all t and applying the definition in (3.1)

$$(a, b) \in \Upsilon_\varepsilon \iff \min_{|t| \leq \frac{1}{\varepsilon}} a + bt \geq 0 \quad . \tag{3.3}$$

For any given $a \geq 0$ and $\varepsilon > 0$, consider the range of allowable b in (3.3) for three sub-intervals of t: (i) $t = 0$, $b \in \mathbb{R}$; (ii) $t \in (0, \frac{1}{\varepsilon}]$, $b \in [-a\varepsilon, \infty)$; (iii) $t \in [-\frac{1}{\varepsilon}, 0)$, $b \in (-\infty, a\varepsilon]$. The constraint (a, b) to be in Υ_ε is the intersection of the range of b for all sub-intervals, i.e. $\{(a, b) \mid a \geq 0, |b| \leq a\varepsilon\}$. $\qquad \square$

Hence, Υ_ε is a two-dimensional cone with vertex at the origin, apex angle $2\theta =$
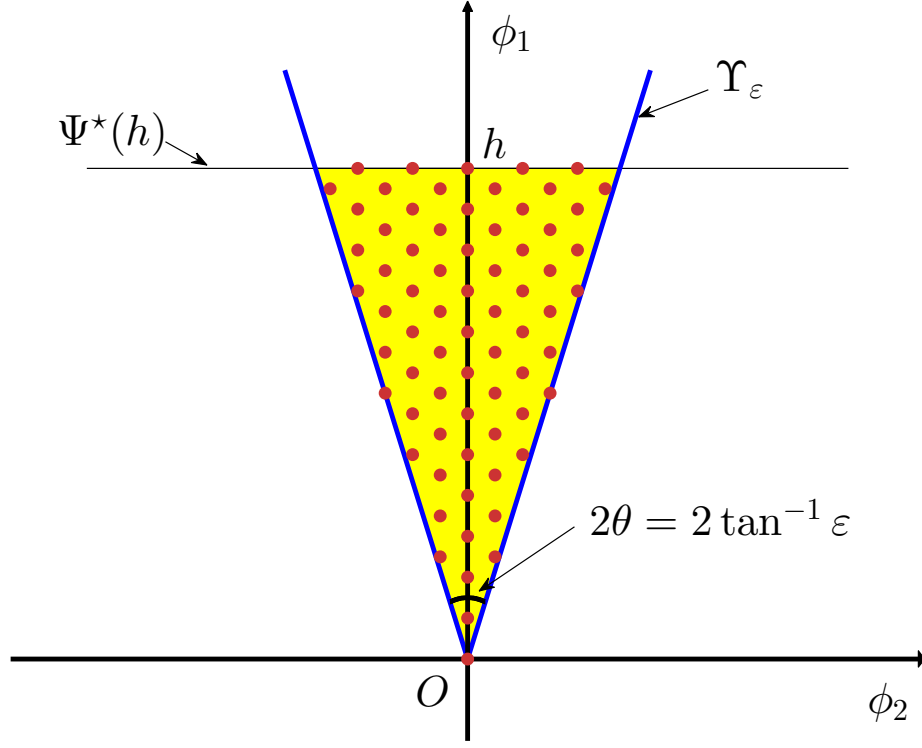
Figure 3.1: The admissible region is a cone with vertex at origin, apex angle $2\theta = 2\tan^{-1}\varepsilon$, and opening about the ϕ_1-axis ($\varepsilon = 0.4$ in plot). The highlighted average optical power bounding region $\Upsilon_\varepsilon \cap \Psi^\star(h)$ is a triangle, where $h/d_{\min} = 12$. A lattice code is defined by intersecting the bounding region with hexagonal lattice A_2 with minimum distance $d_{\min}$

$2\tan^{-1}\varepsilon$, opening about the ϕ_1-axis as illustrated in Fig. 3.1. By adjusting ε, the domain over which each transmitted symbol, $s(t)$, is guaranteed to be strictly non-negative can be controlled. In other words, ε parameterizes the degree of non-negativity that can be accepted for transmission.

Fig. 3.2 presents the waveform of $a\phi_1(t) \pm b\phi_2(t)$ where (a, b) is selected from boundary of Υ_ε to illustrate how *essentially non-negative* the signal is built. For example, when $\varepsilon = \sqrt{3}/(2\pi)$, the waveform is non-negative within the main lobes, i.e. $t \in [-T, T]$ as shown in Fig. 3.2(a). The smaller ε means that the domain of
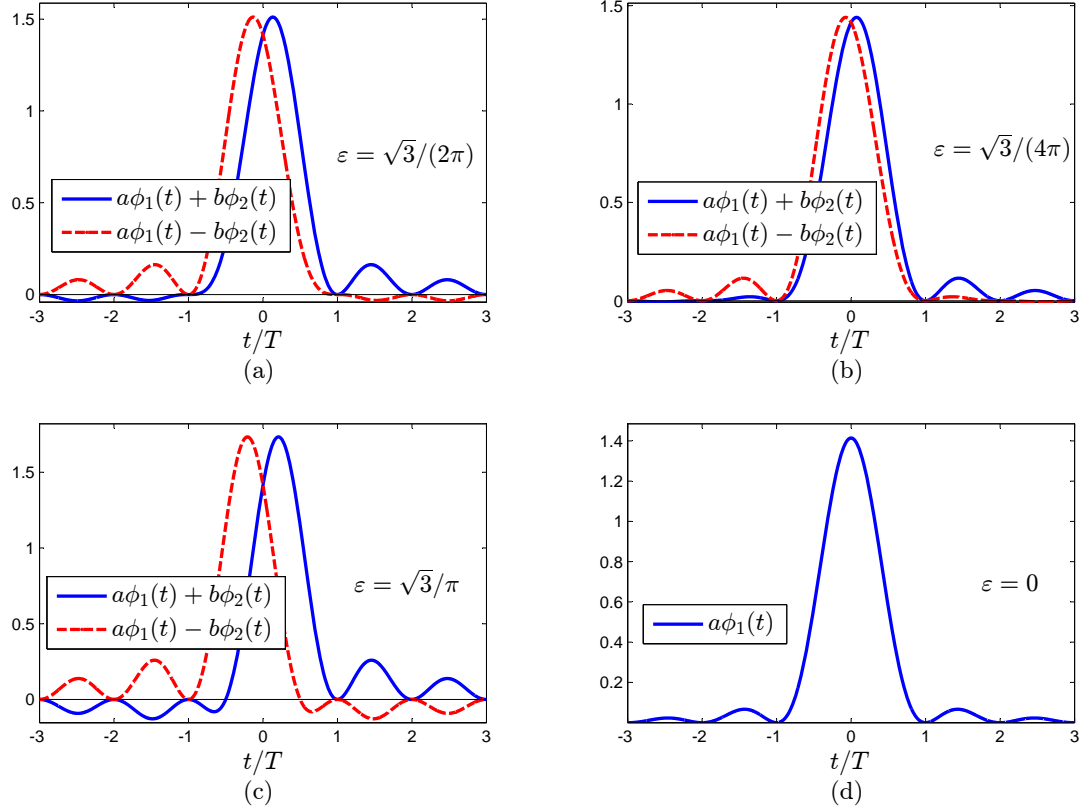
Figure 3.2: Time-domain waveform of $a\phi_1(t) \pm b\phi_2(t)$, where $a = 1$ and $b = \varepsilon a$ for a fixed ε where $\epsilon \in \{0, \sqrt{3}/(4\pi), \sqrt{3}/(2\pi), \sqrt{3}/\pi\}$.

t to guarantee the non-negativity of $s(t) = a\phi_1(t) + b\phi_2(t)$ is increased as shown in Fig. 3.2(b). In contrast, for a larger ε, the domain of t to guarantee the non-negativity of $s(t)$ is decreased as illustrated in Fig. 3.2(c). The extremal case occurs when $\varepsilon = 0$ such that $s(t)$ converges to a simple squared sinc (S2) pulse and thus strictly non-negative for all $t \in \mathbb{R}$.

Intuitively, when $\varepsilon \to 0$, $\Upsilon_{\varepsilon \to 0}$ approaches a one-dimensional non-negative half-infinite interval in ϕ_1-axis and $x(t)$ is guaranteed to be non-negative for all $t \in \mathbb{R}$. Larger values for ε provide more degrees of freedom for constellations, i.e. higher spectral efficiency, with the price of more negativity introduced into $x(t)$.

3.2 Average Optical Power Bounding Region

Analogous to the definition in [26], a *shaping region* must be defined to represent both average or peak optical power constraints. For the average optical power constraint, assuming that the impact of clipping negative excursions (2.9) is negligible, the average optical power is solely related to the component of each symbol in the ϕ_1-axis. In this case, the optimal shaping region in the sense of minimum average optical power, for a given volume and admissible region Υ_ε is [26, Sec.IV-H]

$$\Psi^\star(h) = \{(a, b) \in \mathbb{R}^2 \mid 0 \leq a \leq h, b \in \mathbb{R}\} \quad . \tag{3.4}$$

Notice that the geometric interpretation of $\Psi^\star(h)$ is a two-dimensional strip as illustrated in Fig. 3.1. Thus, the average optical power bounding region for a given $\varepsilon > 0$ is the intersection of essentially non-negative admissible region and optimal shaping region and takes the form as $\Upsilon_\varepsilon \cap \Psi^\star(h)$.

3.3 Essentially Peak-Limited Bounding Region

Similar to the definition in [26, Sec.III-C], define the *essentially peak-limited bounding region*, $\Pi_\varepsilon(p)$ for $p > 0$, as the set of all points in the signal space such that $s(t)$ is bounded from above by $p\hat{\phi}_1$ in the interval $|t/T| \leq \sqrt{3}/(2\pi\varepsilon)$. Formally, for $p > 0$

$$\Pi_\varepsilon(p) = \left\{(a, b) \in \mathbb{R}^2 : \max_{|t| \leq \frac{T\sqrt{3}}{\varepsilon 2\pi}} a\phi_1(t) + b\phi_2(t) \leq p\hat{\phi}_1\right\} \quad . \tag{3.5}$$
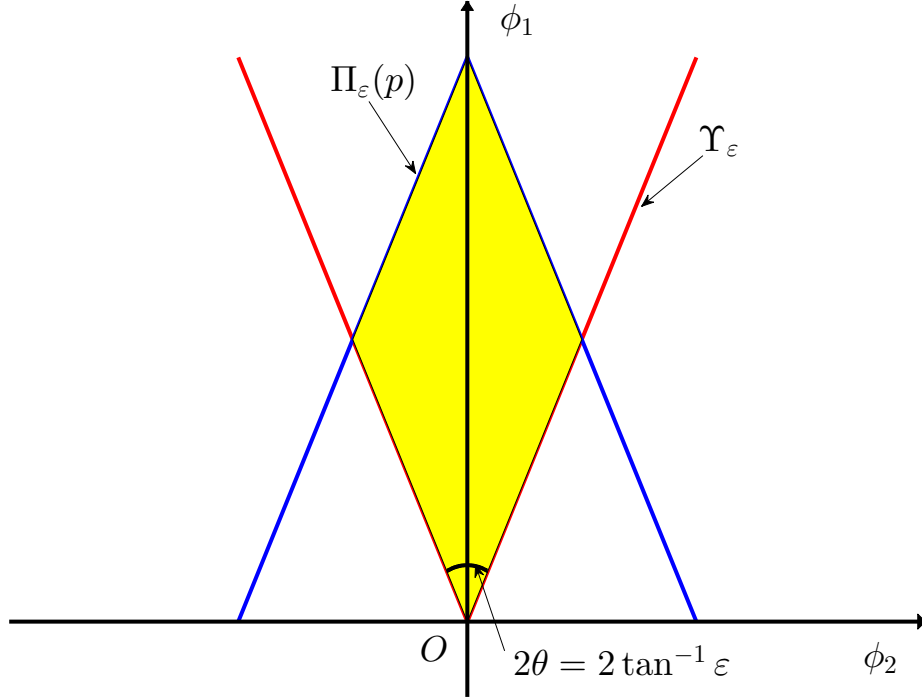
Figure 3.3: The essentially peak-limited bounding region $\Pi_\varepsilon(p)$ and admissible region Υ_ε, apex angle $2\theta = 2\tan^{-1}\varepsilon$ ($\varepsilon = 0.5$ in plot). The highlighted area is $\Upsilon_\varepsilon \cap \Pi_\varepsilon(p)$.

Similar to [26, Sec.III-C], it is possible to relate $\Pi_\varepsilon(p)$ to Υ_ε via the affine transform

$$\Pi_\varepsilon(p) = -\Upsilon_\varepsilon + p\vec{\phi}_1$$

where $\vec{\phi}_1$ is an unit vector in ϕ_1 direction.

Notice that although $\Pi_\varepsilon(p)$ constrains the peak amplitude of each symbol over a given time interval, this is not necessarily true for sequences of symbols used to construct $x(t)$ as in (2.4). However, at the sample instants, i.e., $x(iT)$, $i \in \mathbb{Z}$, the amplitude is determined only by the a_i component. Thus, selecting $(a_i, b_i) \in \Pi_\varepsilon(p)$ is sufficient to bound $x(iT) \leq p\hat{\phi}_1$. Excursions beyond the $p\hat{\phi}_1$ will be clipped by the modulator and will contribute to clipping distortion, as shown in (2.10). Intuitively,

29

to satisfy both constraints of *essentially non-negative* and *peak-bounded* from above by $p\hat{\phi}_1$, it is required to select (a_i, b_i) from the intersection of essentially peak-limited bounding region and essentially non-negative admissible region, i.e. $\Upsilon_\varepsilon \cap \Pi_\varepsilon(p)$ as shown in the highlighted region in Fig. 3.3. Chap. 4.2.3 quantifies the likelihood of peak amplitude clipping as a function of ε.

3.4   Summary

In this chapter, a two-dimensional signal space for bandlimited optical intensity channels is presented by relaxing the strict non-negative and peak optical power constraints. The essentially non-negative admissible region, average optical power bounding region, and the essentially peak-limited bounding region are defined. In next chapter, the lattice codes which satisfy essentially non-negative and peak-limited constraints will be provided and the performance will be analyzed.

Chapter 4

Lattice Codes and Likelihood of Clipping

In this chapter, *essentially non-negative* and *peak amplitude limited* lattice codes for bandlimited IM/DD channels are defined. The asymptotic average and peak optical power gain over a baseline scheme under the assumption of negligible clipping distortion are presented. The likelihood of clipping applying the continuous approximation [49] is used to quantify how the signals constructed using such essentially non-negative and peak-limited lattice codes violate the non-negativity and amplitude constraints. Numerically computed upper bound of the likelihood of clipping under average optical power constraint is presented. A tractable series approximation approach is applied to compute the likelihood of clipping under average and peak amplitude constraints.

4.1   Lattice Codes

An n-dimensional (n-D) *lattice* Λ_n is a discrete subset of $\mathbb{R}^n$ that has the group property. The points of the lattice then form a uniform infinite packing of $\mathbb{R}^n$. For example, the set of integers $\mathbb{Z}$ is a one-dimensional lattice since $\mathbb{Z}$ is a discrete subgroup of $\mathbb{R}$. Any 1-D lattice is in the form $\Lambda_1 = k\mathbb{Z}$ for some scalar $k > 0$.

The use of lattice codes over bandlimited conventional electrical channel has been explored in previous studies [49–52]. However, the optimized modulation techniques in these channels cannot be applied directly to bandlimited IM/DD channels, since the conventional electrical channels do not take the amplitude and non-negativity constraints into consideration. The lattice codes over optical intensity channel are investigated in literatures [26, 27]. Coding and shaping gain over a baseline for large constellation were derived and ultimate shaping gain was presented. However, lattice codes were used for time-limited signaling designed.

This chapter uses the signal space in Chap. 3 to define lattice codes which essentially satisfy the amplitude and non-negative constraints with high probability for bandwidth limited signaling since the current signal $x(t)$ in (2.4) is a strictly bandlimited output for a sequence of input symbols. Average, peak optical power gains with respect to a baseline scheme and spectral efficiency as measure of performance are derived by applying the continuous approximation [49] under the assumption of negligible clipping distortion. Numerical validation of these claims is provided in Chap. 5.

4.1.1   Definitions

To be consistent with previous work [31–33], the baseline scheme chosen is on-off keying (OOK) using S2 pulse shape $\phi_1(t)$ with a sampling receiver with front-end filter $g_1(t)$. The baseline constellation is denoted as $\Omega^{\text{ref}} = \{0, d_{\min}^{\text{ref}}\}$. Notice that this baseline outputs signals which are strictly non-negative and limited from above by $d_{\min}^{\text{ref}}\hat{\phi}_1$ since $\sum_{i=-\infty}^{\infty} \phi_1(t - iT) = \hat{\phi}_1$ for all $t \in \mathbb{R}$. Thus, the baseline does not suffer from any clipping distortion under average optical power constraint or the peak amplitude constraint either, if $p\hat{\phi}_1 \geq d_{\min}^{\text{ref}}\hat{\phi}_1$.

The spectral efficiency, η, is defined as the ratio of bit rate R_{b} to one-sided bandwidth B in units of bit per second per Hz, that is,

$$\eta = \frac{R_{\text{b}}}{B} \quad [\text{bit/s/Hz}] \tag{4.1}$$

where $R_{\text{b}} = \frac{1}{T}\log_2 |\Omega|$.

4.1.2   Average Optical Power Constraint

Under an average optical power constraint, an essentially non-negative lattice code can be defined as

$$\Omega^{\text{a}}(\Lambda_2, \Upsilon_\varepsilon, \Psi^\star(h)) = (\Lambda_2 + \mathbf{t}) \cap \Upsilon_\varepsilon \cap \Psi^\star(h) \tag{4.2}$$

where $\Lambda_2 + \mathbf{t}$ is a two-dimensional lattice translate. Thus, Ω^{a} is the intersection of $\Lambda_2 + \mathbf{t}$ and the average optical power bounding region $\Upsilon_\varepsilon \cap \Psi^\star(h)$, as shown in Fig. 3.1 for the case of a hexagonal lattice. Notice that the average optical power of Ω^{a} is controlled by the selection of h.

The average optical power gain of one scheme over the baseline scheme is defined as

$$\overline{P}_{\mathrm{o,gain}} = \frac{\overline{P}_{\mathrm{o}}^{\mathrm{ref}}}{\overline{P}_{\mathrm{o}}} \tag{4.3}$$

where $\overline{P}_{\mathrm{o}}$ and $\overline{P}_{\mathrm{o}}^{\mathrm{ref}}$ are the average optical powers required for the two schemes to achieve a given probability of bit error, P_{e}, given a fixed bandwidth B. For signal space model in Chap. 3.1, a modulation scheme is then described by Ω^{a}, bases ϕ_1, ϕ_2, and the two filters g_1, g_2. For schemes in this thesis using ϕ_1 and ϕ_2, the spectral efficiency is equal to $\log_2 |\Omega^{\mathrm{a}}|$ since $BT = 1$. Thus the spectral efficiency of baseline is thus 1 bit/sec/Hz.

For the baseline scheme, using (2.9), the average optical power is

$$\overline{P}_{\mathrm{o}}^{\mathrm{ref}} = \frac{d_{\min}(\Omega^{\mathrm{ref}})}{2} \overline{\phi}_1 \quad . \tag{4.4}$$

Notice that for the baseline this is not an approximation since the modulation output is strictly non-negative. In addition, this baseline does not suffer for any negative clipping distortion or clipping at the peak.

The expression for average optical power of Ω^{a} in (2.9) depends on the clipping distortion introduced by any negative excursions of $x(t)$. As will be shown in Chap. 4.2, the likelihood of clipping can be made small through the proper selection of ε. Ignoring clipping, $\overline{P}_{\mathrm{o}}$ in (2.9) can be approximated by applying the *continuous approximation* to estimate discrete sums over the constellation points by normalized integrals

over $\Upsilon_\varepsilon \cap \Psi^\star(h)$ [49]. Thus, using [26, (35)], $\overline{P}_o$ is approximated as

$$\overline{P}_o \approx \overline{\phi}_1 \int_{\Upsilon_\varepsilon \cap \Psi^\star(h)} \frac{a}{V(\Upsilon_\varepsilon \cap \Psi^\star(h))} da db = \frac{2}{3}\overline{\phi}_1 h \quad . \tag{4.5}$$

The continuous approximation is tight when $V(\Upsilon_\varepsilon \cap \Psi^\star(h)) \gg V(\Lambda_2)$, or equivalently when $|\Omega^a|$ is large.

For the baseline, the probability of a symbol error, P_s, is equal to P_e and can be related to the $d^{\text{ref}}_{\min}$ and Gaussian noise variance σ^2 by [48]

$$P_e(\Omega^{\text{ref}}, \sigma) = Q\left(\frac{d^{\text{ref}}_{\min}}{2\sigma}\right)$$

where $Q(\cdot)$ is the Gaussian tail function which takes the form as

$$Q(x) \triangleq \frac{1}{\sqrt{2\pi}} \int_x^\infty \exp(-u^2/2) du \quad .$$

Thus $d^{\text{ref}}_{\min}$ can be expressed in terms of P_e

$$d^{\text{ref}}_{\min} = 2\sigma Q^{-1}(P_e) \quad . \tag{4.6}$$

For the given scheme using Ω^a, P_e can be approximated by the relation

$$P_e(\Omega^a, \sigma) \approx \frac{\overline{N}(\Omega^a)}{\log_2 |\Omega^a|} \cdot Q\left(\frac{d_{\min}(\Omega^a)}{2\sigma}\right) \tag{4.7}$$

where $\overline{N}(\Omega^a)$ is the error coefficient related to the number of adjacent neighbors to each constellation point in Ω^a. The above equation arises under the assumption of Gray mapping [53, Chp.2], i.e. the binary number representing each symbol in any

given constellation Ω only differs by one bit to each adjacent symbol. Thus, at high signal-to-noise (SNR) scenario, the symbol error can be viewed most likely resulted from error decision to nearest symbol and the relation between bit error rate (BER) and symbol error rate (SER) is $P_{\mathrm{e}} \approx P_{\mathrm{s}}/\log_2 |\Omega|$. From (4.7),

$$d_{\min}(\Omega^{\mathrm{a}}) \approx 2\sigma Q^{-1} \left(\frac{P_{\mathrm{e}} \log_2 |\Omega^{\mathrm{a}}|}{\overline{N}(\Omega^{\mathrm{a}})} \right) \quad . \tag{4.8}$$

Similar to [26, 33], substituting (4.4) and (4.5) into (4.3), the asymptotic average optical power gain of a given scheme over baseline in the limit as $P_{\mathrm{e}} \to 0$ is

$$\overline{P}_{\mathrm{o,gain}} = \frac{3d_{\min}(\Lambda_2)}{4h} \quad . \tag{4.9}$$

The above equation takes advantage of the fact that as $\overline{P}_e \to 0$, $d_{\min}(\Omega^{\mathrm{ref}}) \to d_{\min}(\Omega^{\mathrm{a}}) = d_{\min}(\Lambda_2)$. Equation (4.9) shows that the asymptotic average optical power gain is independent of ε and channel noise.

The spectral efficiency (4.1) can also be approximated via the continuous approximation as,

$$\eta^a \approx \log_2 \frac{V(\Upsilon_\varepsilon \cap \Psi^\star(h))}{V(\Lambda_2)} = \log_2 \frac{\varepsilon h^2}{V(\Lambda_2)} \tag{4.10}$$

where the notation $V(\cdot)$ denotes the volume of a region and $V(\Upsilon_\varepsilon \cap \Psi^\star(h))/V(\Lambda_2)$ is the approximation of size of the constellation Ω^{a}.

4.1.3   Peak Amplitude Constraint

For case of peak optical power bounded above from by $p\hat{\phi}_1$, essentially peak amplitude limited lattice codes can be defined in a manner analogous to Chap. 4.1.2, as

$$\Omega^{\mathrm{p}}(\Lambda_2, \Upsilon_\varepsilon, \Pi_\varepsilon(p)) = (\Lambda_2 + \mathbf{t}) \cap \Upsilon_\varepsilon \cap \Pi_\varepsilon(p) \quad . \tag{4.11}$$

Using the same baseline as in Chap. 4.1.2, the peak optical power gain of a lattice code is defined as

$$\hat{P}_{\mathrm{o,gain}} = \frac{\hat{P}_{\mathrm{o}}^{\mathrm{ref}}}{\hat{P}_{\mathrm{o}}} \tag{4.12}$$

where $\hat{P}_{\mathrm{o}}^{\mathrm{ref}}$ and $\hat{P}_{\mathrm{o}}$ are the peak amplitudes needed for each to achieve a given bit error rate.

Notice that $\hat{P}_{\mathrm{o}}^{\mathrm{ref}} = d_{\mathrm{min}}^{\mathrm{ref}} \hat{\phi}_1$ and $\hat{P}_{\mathrm{o}} = p\hat{\phi}_1$ from (2.12). Similarly, the asymptotic peak optical power gain in the limit as $P_{\mathrm{e}} \to 0$ is

$$\hat{P}_{\mathrm{o,gain}} = \frac{d_{\mathrm{min}}(\Lambda_2)}{p} \quad . \tag{4.13}$$

Similarly, the spectral efficiency (4.1) can also be approximated as,

$$\eta^p \approx \log_2 \frac{V(\Upsilon_\varepsilon \cap \Pi_\varepsilon(p))}{V(\Lambda_2)} = \log_2 \frac{\varepsilon p^2}{2V(\Lambda_2)} \quad . \tag{4.14}$$

4.2   Likelihood of Clipping

The lattice codes constructed in Chap. 4.1.2 and Chap. 4.1.3 violate the non-negative amplitude constraint and both peak and non-negative amplitudes constraints, respectively, with some positive probability whenever $\varepsilon > 0$. In this part, the severity of

clipping is quantified by the likelihood that $x(t) < 0$ and $x(t) > p\hat{\phi}_1$ under the continuous approximation, where $x(t)$ is the output electrical current signal from a sequence of inputs. In [34], an upper bound on $\mathrm{P}(x(t) < 0)$ using Hoeffding's inequality [54] is obtained and a Gaussian approximation is applied for numerical computation of the likelihood of negative amplitude excursion under average optical power constraint. In this thesis, the comparison amongst upper bound on $\mathrm{P}(x(t) < 0)$ by applying one-sided Cantelli's inequality, Bhattacharyya's inequality, and Hoeffding's inequality are presented. In addition, a more accurate and efficient finite series approach [55] is applied to compute the likelihood under average and peak optical power constraints. Results using series approach are compared to Monte-Carlo results.

4.2.1   Average Optical Power Constraint: $\mathrm{P}(x(t) < 0)$

Considering a constraint on the average optical power, the bounded region to form a constellation for a fixed ε is a truncated cone discussed in Chap. 3.2 and shown in Fig. 3.1. This part of work determines $\mathrm{P}(x(t) < 0)$ for such average optical power limited signaling sets.

Since the likelihood of a negative excursion is independent of scaling, without loss of generality, assume the bounded region is $\Upsilon_\varepsilon \cap \Psi^\star(1)$. Furthermore, we apply the continuous approximation and consider that constellation points (a_i, b_i) are drawn independently and equally likely over $\Upsilon_\varepsilon \cap \Psi^\star(1)$. Under these assumptions, RV a_i (in the ϕ_1 direction) satisfies a triangular distribution with lower limit 0, upper limit 1 and mode 1. Given the uniform distribution over $\Upsilon_\varepsilon \cap \Psi^\star(1)$, it is also clear that $\mathrm{P}(b_i | a_i)$ is uniform over $[-\varepsilon a_i, \varepsilon a_i]$.

Notice that $V(\Upsilon_\varepsilon \cap \Psi^\star(1)) = \varepsilon$. The probability density function (pdf) of RV a_i

is

$$
\begin{aligned}
f_a(x) &= \int_{-x\varepsilon}^{x\varepsilon} f_{ab}(x, y)dy \\
&= 2x, \quad x \in [0, 1] \quad .
\end{aligned}
\tag{4.15}
$$

Similarly, the pdf of RV b_i can also be shown as

$$
f_b(x) = \begin{cases}
\dfrac{1}{\varepsilon^2}(x + \varepsilon), & \text{if } x \in [-\varepsilon, 0] \quad , \\[2mm]
-\dfrac{1}{\varepsilon^2}(x - \varepsilon), & \text{if } x \in (0, \varepsilon] \quad .
\end{cases}
\tag{4.16}
$$

The statistics of $x(t) = \sum_{i=-\infty}^{\infty} a_i\phi_1(t - iT) + b_i\phi_2(t - iT)$ in (2.4) are cyclostationary in period T since (a_i, b_i) are selected independently and equiprobably every T. Therefore, it is only needed to consider the statistics of $x(t)$ in the interval $[0, T)$.

Define variable $q = t/T$ for $t \in [0, T)$ and

$$
X^{\mathrm{a}}(q) = x(qT) = \sum_{i=-\infty}^{\infty} a_i\varphi_{1,i}(q) + b_i\varphi_{2,i}(q)
\tag{4.17}
$$

where $(a_i, b_i) \in \Upsilon_\varepsilon \cap \Psi^\star(1)$ and

$$
\begin{aligned}
\varphi_{1,i}(q) &= \phi_1\left((q - i)T\right) \quad , \\
\varphi_{2,i}(q) &= \phi_2\left((q - i)T\right) \quad .
\end{aligned}
$$

Notice that

$$
\begin{aligned}
\varphi_{1,1-i}(1 - q) &= \varphi_{1,i}(q) \\
\varphi_{2,1-i}(1 - q) &= -\varphi_{2,i}(q)
\end{aligned}
$$

since $\phi_1(t)$ is even and $\phi_2(t)$ is odd. Thus

$$
\begin{aligned}
X^{\mathrm{a}}(1-q) &= \sum_{i=-\infty}^{\infty} a_i \varphi_{1,i}(1-q) + b_i \varphi_{2,i}(1-q) \\
&= \sum_{i=-\infty}^{\infty} a_i \varphi_{1,1-i}(q) - b_i \varphi_{2,1-i}(q) \quad .
\end{aligned}
\tag{4.18}
$$

Recall that the conditional pdf of b_i given a_i is even symmetric and $\{(a_i, b_i)\}$ is independently and equiprobably selected at each symbol instant. Thus the statistics of $X^{\mathrm{a}}(q)$ is also even symmetric about $q = 0.5$. For $t = iT$, $i \in \mathbb{Z}$, $x(t)$ is simplified to a single RV, i.e., $a_i \phi_1(0)$, and is strictly non-negative. Thus, for analysis of the likelihood of negativity of $X^{\mathrm{a}}(q)$, the domain of q is focused on the interval $(0, 0.5]$.

Define the RVs $Z_i(q)$ as a function of q and ε

$$
Z_i(q) = a_i \varphi_{1,i}(q) + b_i \varphi_{2,i}(q) \quad .
\tag{4.19}
$$

Thus, $X^{\mathrm{a}}(q)$ in (4.17) is the sum of independent RVs $\{Z_i(q)\}$. The minimum and maximum of $Z_i(q)$ for given q and ε can be obtained through linear programming in the form as

$$
\begin{aligned}
&\text{minimize/maximize} \quad \varphi_{1,i}(q) a_i + \varphi_{2,i}(q) b_i \\
&\text{subject to} \quad (a_i, b_i) \in \Upsilon_\varepsilon \cap \Psi^\star(1)
\end{aligned}
$$

Each $Z_i(q)$ can be shown to have a bounded triangular distribution with lower limit $p_i^{\mathrm{l}}(q) = \min(0, \alpha_i(q))$, mode $p_i^{\mathrm{m}}(q) = \max(0, \alpha_i(q))$, and upper limit $p_i^{\mathrm{u}}(q) = \beta_i(q)$

where

$$\alpha_i(q) = \varphi_{1,i}(q) - \varepsilon |\varphi_{2,i}(q)| \quad , \tag{4.20}$$

$$\beta_i(q) = \varphi_{1,i}(q) + \varepsilon |\varphi_{2,i}(q)| \quad . \tag{4.21}$$

For notational simplicity, hereafter ε and q are omitted. From previous work on the study of triangular distributions [56] [57, Chp.1], the pdf of Z_i can be written as

$$f_{Z_i}(x) = \begin{cases} 0 & x < 0 \quad , \\ \dfrac{2(x - p_i^{\mathrm{l}})}{(p_i^{\mathrm{u}} - p_i^{\mathrm{l}})(p_i^{\mathrm{m}} - p_i^{\mathrm{l}})} & p_i^{\mathrm{l}} \le x \le p_i^{\mathrm{m}} \quad , \\ \dfrac{2(p_i^{\mathrm{u}} - x)}{(p_i^{\mathrm{u}} - p_i^{\mathrm{l}})(p_i^{\mathrm{u}} - p_i^{\mathrm{m}})} & p_i^{\mathrm{m}} < x \le p_i^{\mathrm{u}} \quad , \\ 0 & x > \beta_i \quad . \end{cases}$$

As an example, Fig. 4.1 shows the pdfs of Z_i where $i \in \{-1, 0, 1, 2\}$ for $q = 0.4$ and $\varepsilon = 0.3$. For $i = 0, 1$, $\alpha_i > 0$. For $i \neq 0, 1$, $\alpha < 0$ and thus Z_i has mode point 0.

4.2.2   Approaches to Find Likelihood of Clipping

The characteristic function of a sum of independent RVs is equal to the product of the individual characteristic function of each RV [58]. Since the pdf of a RV and its characteristic function are a Fourier transform pair and $\{Z_i\}$ are independent, the pdf of X^{a} is

$$f_{X^{\mathrm{a}}} = \cdots f_{Z_0} * f_{Z_1} * f_{Z_2} \cdots \quad . \tag{4.22}$$

It is a challenging task to obtain a closed form for this infinite convolution. However, we only focus on the likelihood of negativity of X^{a}, or equivalently, $F_{X^{\mathrm{a}}}(0)$, where
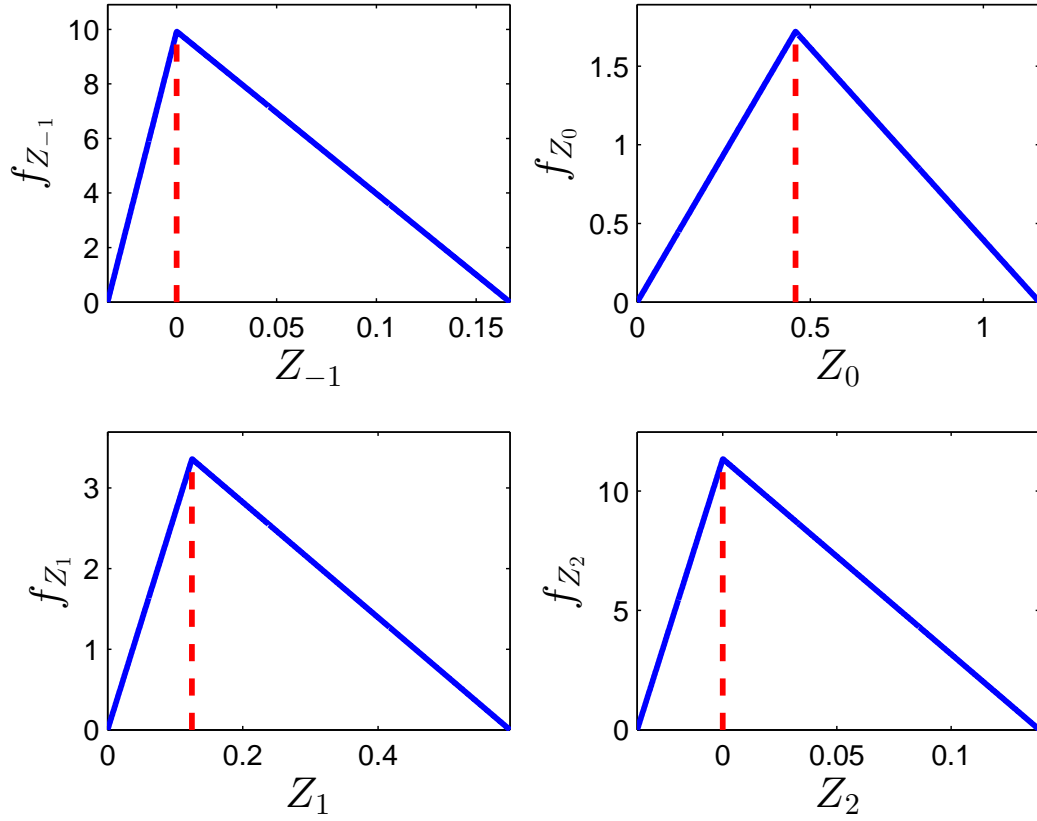
Figure 4.1: pdf of triangular distributed RVs Z_i, where $i = \{-1, 0, 1, 2\}$, $\varepsilon = 0.3$, $q = 0.4$ applying the continuous approximation.

F_{X^a} is the cumulative distribution function (cdf) of X^a. Consider splitting the terms in $X^a = \sum_i Z_i$ into two parts denoted as S and R such that

$$
\begin{aligned}
S &= \sum_{j \in \mathcal{V}} Z_j \\
R &= X^a - S
\end{aligned}
$$

where $\mathcal{V}$ is the finite set of index j such that RV Z_j has non-negative support, i.e. $\alpha_j > 0$, and R is termed the *residual sum*. Thus the sufficient and necessary condition

to $j \in \mathcal{V}$ is

$$|q - j| \leq \frac{\sqrt{3}}{\varepsilon 2\pi} \quad . \tag{4.23}$$

It is clear that RVs S and R are mutually independent. From elementary probability theory [59, Chp.7.2],

$$
\begin{aligned}
F_{X^{\mathrm{a}}}(0) &= \int_{-\infty}^{0} f_{X^{\mathrm{a}}}(\tau) d\tau \\
&= \int_{-\infty}^{0} \int_{-\infty}^{\infty} f_S(u) f_R(\tau - u) du d\tau \\
&= \int_{-\infty}^{\infty} f_S(u) F_R(-u) du
\end{aligned}
\tag{4.24}
$$

where $F_R(\tau)$ is the cdf of R. Since the domain of each $Z_j \in S$ is bounded over $[0, \beta_j]$, the support of S is also bounded in the interval $[0, \sum_{j \in \mathcal{V}} \beta_j]$. Then (4.24) is simplified to a definite integral from 0 to $\sum_{j \in \mathcal{V}} \beta_j$. It is tractable to numerically compute the pdf of S. An upper bound on $\mathrm{P}\left(X^{\mathrm{a}} < 0\right)$ can be achieved by finding an upper bound of $F_R(u)$ over the domain $[-\sum_{j \in \mathcal{V}} \beta_j, 0]$.

As an example, Fig. 4.2 illustrates the numerically computed pdf of $S = Z_0 + Z_1$ for a given $q = 0.5$ and $\varepsilon = 0.3$. The pdf of S is computed via the convolution of two triangular distributions f_{Z_0} and f_{Z_1}.

Cantelli's Upper Bound

In probability theory, Cantelli's inequality [60] which is also called *one-sided Cheby-shev's* inequality states that for any real random variable Y with mean μ and variance
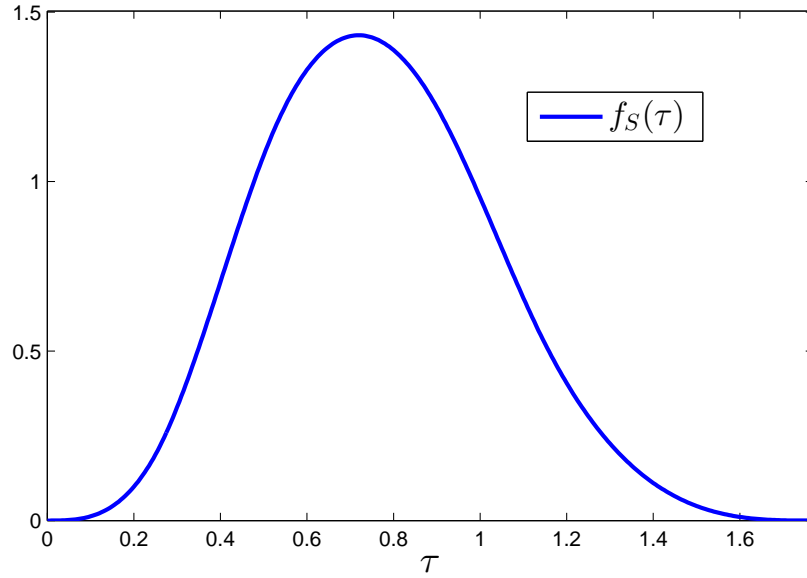
Figure 4.2: Numerically computed $f_S(\tau)$ for a given $q = 0.5$ and $\varepsilon = 0.3$ over the interval $\tau \in [0, \beta_0 + \beta_1]$.

σ_Y^2, and any positive number $c > 0$,

$$\mathrm{P}\left(Y - \mu \geq c\right) \leq \frac{\sigma_Y^2}{\sigma_Y^2 + c^2} \tag{4.25}$$

$$\mathrm{P}\left(Y - \mu \leq -c\right) \leq \frac{\sigma_Y^2}{\sigma_Y^2 + c^2} \tag{4.26}$$

The inequality has great utility because it can be applied to completely arbitrary distributions and thus an upper bound of $F_R(-\tau)$ over $\tau \in [0, \sum_{j \in \mathcal{V}} \beta_j]$ can be obtained given variance and mean of R denoted as σ_R^2 and μ_R, respectively.

The closed form of μ_R is derived as follow

$$
\begin{aligned}
\mu_R &= \mathrm{E}\left[X^{\mathrm{a}}\right] - \mathrm{E}\left[S\right] \\
&= \mathrm{E}\left[a_i\right] \sum_{i=-\infty}^{\infty} \varphi_{1,i} + \mathrm{E}\left[b_i\right] \sum_{i=-\infty}^{\infty} \varphi_{2,i} - \mathrm{E}\left[S\right] \\
&= \frac{2}{3}\left(\overline{\phi}_1 - \sum_{j\in\mathcal{V}} \varphi_{1,j}\right) \quad .
\end{aligned}
\tag{4.27}
$$

The last step arises since $\mathrm{E}\left[a_i\right] = 2/3$ and $\mathrm{E}\left[b_i\right] = 0$ which are described in Appendix. A.1 and the fact $\sum_{i=-\infty}^{\infty} \varphi_{1,i}$ is a constant $\overline{\phi}_1$ [61].

The derivation of variance of R is presented in Appendix A.1, $\mathrm{Var}\left[R\right]$ takes the form

$$
\sigma_R^2 = \frac{\overline{\phi}_1^2}{54}\left(2\cos^2 \pi q + 1 + 12\varepsilon^2 \sin^2 \pi q\right) - \sum_{j\in\mathcal{V}} \frac{\varphi_{1,j}^2}{18} + \frac{\varepsilon^2 \varphi_{2,j}^2}{6} \quad .
\tag{4.28}
$$

Notice that μ_R must be positive for any $q \in (0, 0.5]$ since $\varphi_{1,i} > 0$ and $\tau + \mu_R > 0$ holds for any non-negative τ. From (4.26), the upper bound of $F_R(-\tau)$ via Cantelli's inequality is

$$
\begin{aligned}
F_R(-\tau) &= \mathrm{P}\left(R - \mu_R \leq -(\tau + \mu_R)\right) \\
&\leq \frac{\sigma_R^2}{\sigma_R^2 + (\tau + \mu_R)^2} \quad .
\end{aligned}
\tag{4.29}
$$

Hence an upper bound on $\mathrm{P}\left(X^{\mathrm{a}} < 0\right)$ can be computed by numerical integration of (4.24) which takes the form as

$$
\mathrm{P}\left(X^{\mathrm{a}} < 0\right) \leq \int_0^{\sum_{j\in\mathcal{V}} \beta_j} f_S(\tau) \frac{\sigma_R^2}{\sigma_R^2 + (\tau + \mu_R)^2} \tau \quad .
\tag{4.30}
$$

Bhattacharyya's Upper Bound

In [62], Bhattacharyya extended Cantelli's inequality and derived an one-sided Cheby-shev's inequality when the first four order moments are known. For any real random variable Y with zero mean and variance σ_Y^2, denote μ_3 and μ_4 as the third and fourth central moments, respectively. Let $\text{Skew}\,[Y] = \mu_3/\sigma_Y^3$ and $\text{Kurt}\,[Y] = \mu_4/\sigma_Y^4$ be the corresponding Pearson measure of skewness and kurtosis, respectively, where σ_Y represents the standard deviation of Y. Notice that the kurtosis is bounded below by the squared skewness plus one [63]:

$$\text{Kurt}\,[Y] \geq \text{Skew}\,[Y]^2 + 1 \quad . \tag{4.31}$$

For every non-negative real c satisfying $c^2 - \text{Skew}\,[Y]\,c - 1 > 0$,

$$\text{P}\,(Y \geq c\sigma_Y) \leq \frac{\text{Kurt}\,[Y] - \text{Skew}\,[Y]^2 - 1}{(\text{Kurt}\,[Y] - \text{Skew}\,[Y]^2 - 1)(1 + c^2) + (c^2 - \text{Skew}\,[Y]\,c - 1)^2} \quad . \tag{4.32}$$

Notice that the classical Cantelli's inequality is given by $\text{P}\,(Y \geq c\sigma_Y) \leq 1/(1 + c^2)$. Thus the Bhattacharyya's inequality is an improvement over the classical bound using Cantelli's inequality.

To compute the upper bound of $F_R(-\tau)$ using Bhattacharyya's inequality, mean μ_R, variance σ_R^2, skewness $\text{Skew}\,[R]$, and kurtosis $\text{Kurt}\,[R]$ are needed. Let $\mu_3(R)$ and $\mu_4(R)$ be the third and fourth central moments of R respectively. It is equivalent to build a zero-mean random variable $R - \mu_R$ and the variance, skewness, and kurtosis of $R - \mu_R$ are unchanged since μ_R is a constant.

For a fixed $q \in (0, 0.5]$ and $\tau \in [0, \sum_{j \in \mathcal{V}} \beta_j]$, using (4.32) and the property that

$\mathrm{Kurt}\,[-R] = \mathrm{Kurt}\,[R]$ and $\mathrm{Skew}\,[-R] = -\mathrm{Skew}\,[R]$,

$$
\begin{aligned}
F_R(-\tau) &= \mathrm{P}\,(R \leq -\tau) \\
&= \mathrm{P}\,(-(R - \mu_R) \geq \tau + \mu_R) \\
&\leq \frac{\mathrm{Kurt}\,[R] - \mathrm{Skew}\,[R]^2 - 1}{(\mathrm{Kurt}\,[R] - \mathrm{Skew}\,[R]^2 - 1)(1 + c^2) + (c^2 + \mathrm{Skew}\,[R]\,c - 1)^2} \quad (4.33)
\end{aligned}
$$

where positive number $c = (\tau + \mu_R)/\sigma_R$. The closed-form of skewness and the numerical approach to compute the approximation of kurtosis are provided in detail in Appendices A.2 and A.3. Notice additionally the above inequality holds only if $c^2 + \mathrm{Skew}\,[R]\,c - 1 > 0$. Thus an upper bound applying Bhattacharyya's inequality can be computed numerically by substituting (4.33) into (4.24).

Hoeffding's Upper Bound

As all the Z_i inside the sum $R = \sum_{i \notin \mathcal{V}} Z_i$ have a bounded support, Hoeffding's inequality [54] [64, Chp.2.6] can be applied to get another upper bound of $F_R(-\tau)$ for $\tau \in (0, \sum_{j \in \mathcal{V}} \beta_j]$.

Hoeffding's inequality provides an upper bound on the probability that the sum of independent RVs deviates from its statistical expectation value. Let $Y_1, \ldots, Y_n$ be n mutual independent RVs such that Y_i is strictly bounded by the interval $[u_i, v_i]$ for all $1 \leq i \leq n$. Denote the sum of Y_i as

$$
W = \sum_{i=1}^{n} Y_i \quad .
$$

Then for every $c > 0$,

$$\mathrm{P}\left(W - \mu_W \geq c\right) \leq \exp\left(-\frac{2c^2}{\sum_{i=1}^{n}(v_i - u_i)^2}\right) \tag{4.34}$$

where μ_W is the expectation value of W.

The upper bound of $F_R(-\tau)$ using Hoeffing's inequality can be obtained through a similar fashion as in Chap. 4.2.2 and 4.2.2. Since each $Z_i, i \notin \mathcal{V}$ in R is bounded by the interval $[\alpha_i, \beta_i]$,

$$\begin{aligned}
F_R(-\tau) &= \mathrm{P}\left(-(R - \mu_R) \geq \tau + \mu_R\right) \\
&\leq \exp\left(-\frac{2(\tau + \mu_R)^2}{\sum_{i \notin \mathcal{V}}(\beta_i - \alpha_i)^2}\right) \quad .
\end{aligned} \tag{4.35}$$

Using (4.20) and (4.21), the denominator term in the exponential power (4.35) can be expressed in the form as

$$\begin{aligned}
\sum_{i \notin \mathcal{V}}(\beta_i - \alpha_i)^2 &= \sum_{i=-\infty}^{\infty} 4\varepsilon^2 \varphi_{2,i}^2 - \sum_{j \in \mathcal{V}} 4\varepsilon^2 \varphi_{2,j}^2 \\
&= \frac{16\varepsilon^2 \overline{\phi}_1^2 \sin^2 \pi q}{3}\left[1 - \sum_{j \in \mathcal{V}} \mathrm{sinc}^2(q - j)\right] \quad .
\end{aligned} \tag{4.36}$$

The second step arises from

$$\varphi_{2,i}^2(q) = \frac{4\overline{\phi}_1^2}{3\pi^2} \cdot \frac{\sin^4 \pi q}{(q - i)^2} \quad ,$$

$$\sum_{i=-\infty}^{\infty} \frac{1}{(q - i)^2} = \frac{\pi^2}{\sin^2 \pi q} \quad .$$

Using (4.24)(4.35) and (4.36), an upper bound on $\mathrm{P}\left(X^{\mathrm{a}} < 0\right)$ applying Hoeffding's

inequality can be numerically computed.

Gaussian Approximation Method

In [34], a Gaussian approximation method to numerically compute $P\left(X^{\mathrm{a}} < 0\right)$ is proposed. The idea is to approximate the distribution of residual sum R using an Gaussian distribution. In addition, the mean and variance of R are chosen to be the parameters of the Gaussian distribution.

Fig. 4.3 presents the histogram plot of $R_{N_{\mathrm{T}}}$ with Gaussian curve fitting using parameters μ_R and σ_R^2 for a fixed $\varepsilon = 0.3$ and q. Recall (4.23), i.e.

$$j \in \mathcal{V} \iff |q - j| \leq \frac{\sqrt{3}}{\varepsilon 2\pi}$$

the index j such that $j \in \mathcal{V}$ for $\varepsilon = 0.3$ and all $q \in [0.1, 0.5]$ is $j \in \{0, 1\}$. It shows that the Gaussian curve fits the distribution of R well. Since S is strictly bounded to an non-negative finite set $[0, \sum_{j \in \mathcal{V}} \beta_j]$, it suffices to focus on the distribution of $F_R(-\tau)$ to the same interval.

Then $F_R(-\tau)$ can be approximated as the cdf of a Gaussian distributed RV using parameters μ_R and σ_R^2 :

$$F_R(-\tau) \approx 1 - \frac{1}{2}\mathrm{erfc}\left(-\frac{\tau + \mu_R}{\sigma_R\sqrt{2}}\right) \tag{4.37}$$

where $\mathrm{erfc}\left(x\right)$ is the complementary error function defined as

$$\mathrm{erfc}\left(x\right) = \frac{2}{\sqrt{\pi}} \int_x^{\infty} \exp\left(-u^2\right) du \quad .$$
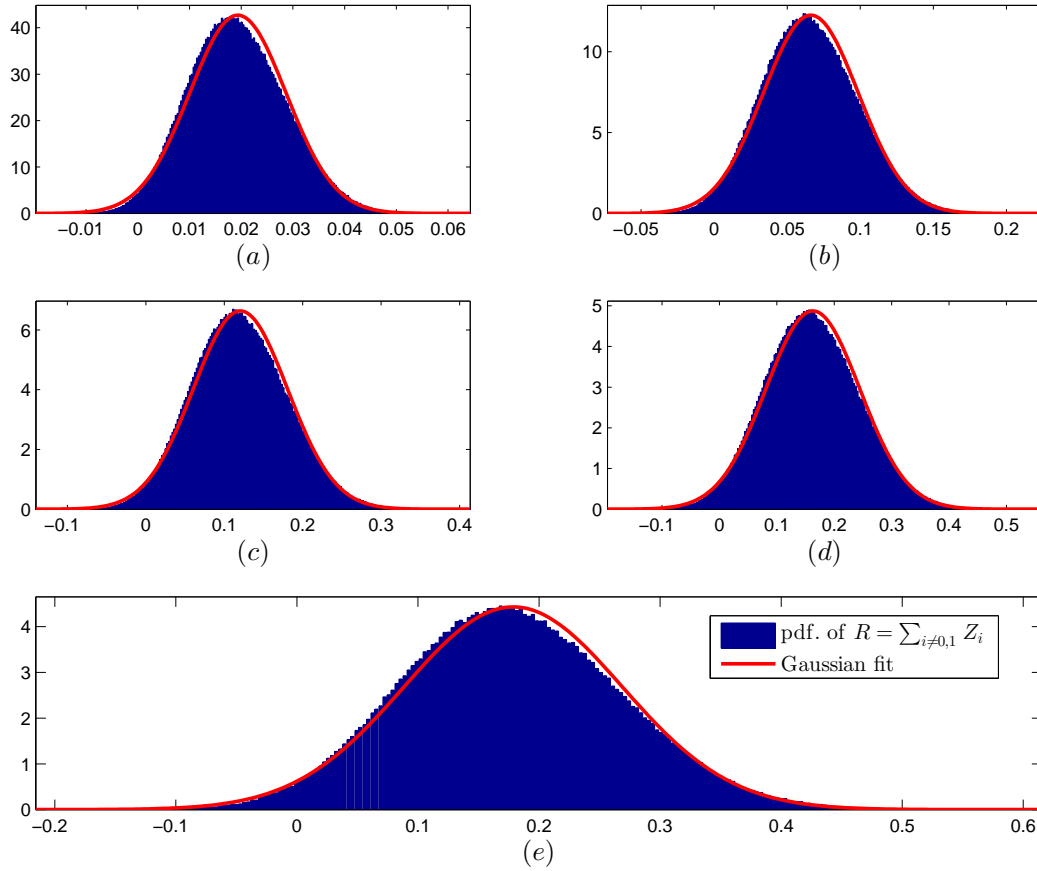
Figure 4.3: pdf of R (blue bar) and Gaussian fitting curves (red solid) using mean and variance of R, given $\varepsilon = 0.3$ and $N_T = 128$. (a)$q = 0.1$; (b)$q = 0.2$; (c)$q = 0.3$; (d)$q = 0.4$; (e)$q = 0.5$

Finite Series Approach

In [55], a convergent infinite series for the computation of the complementary cumulative distribution function (ccdf) of a sum of independent but not necessary identically distributed random variables was introduced. Since X^a (4.17) is the sum of independent $\{Z_i\}$, the series method can be applied to numerically compute $F_{X^a}(0) = P(X^a < 0)$. Notice that this computation must be done for every choice of q and ε.

The strictly bandlimited signals are duration unlimited and thus unachievable in practice. For numerical computation, the bases $\phi_1(t)$ and $\phi_2(t)$ are truncated in time domain to N_T lobes such that

$$\frac{\displaystyle\int_{-N_\mathrm{T}T}^{N_\mathrm{T}T}|\phi_i(t)|^2 dt}{\displaystyle\int_{-\infty}^{\infty}|\phi_i(t)|^2 dt} \geq \kappa, \quad i = 1, 2 \tag{4.38}$$

where κ is a fraction coefficient typically chosen close to unity. The denominator in (4.38) represents the energy of basis function. Using Parseval's theorem and from Fig. 2.3, the energy of $\phi_1(t)$ and $\phi_2(t)$ are

$$\begin{aligned}
\int_{-\infty}^{\infty}|\phi_1(t)|^2 dt &= 2\int_0^{1/T}|G_1(f)|^2 df \\
&= 2\int_0^{1/T} 2T^3(f - 1/T)^2 df = \frac{4}{3} \quad, \tag{4.39} \\
\int_{-\infty}^{\infty}|\phi_2(t)|^2 dt &= 2\int_0^{1/T}|G_2(f)|^2 df \\
&= 2\int_0^{1/T}\frac{2T}{3} df = \frac{4}{3} \quad. \tag{4.40}
\end{aligned}$$

The numerator in (4.38) can be computed symbolically via using a symbolic mathematics computational engine [65] and computed numerically. The integral of the

truncated basis functions takes the form as

$$
\int_{-N_\mathrm{T}T}^{N_\mathrm{T}T} |\phi_1(t)|^2 dt = 2\bar{\phi}_1^2 T \int_0^{N_\mathrm{T}} \mathrm{sinc}^4(u)du
$$

$$
= \frac{4}{\pi}\left[-\frac{2\mathrm{Si}(2u) - 4\mathrm{Si}(4u)}{3} - \frac{\sin^4 u}{3u^3} - \frac{2\cos u \sin^3 u}{3u^2} - \frac{2\sin^2 u(1 + 2\cos 2u)}{3u}\right]\Bigg|_0^{\pi N_\mathrm{T}}
$$

$$
\int_{-N_\mathrm{T}T}^{N_\mathrm{T}T} |\phi_2(t)|^2 dt = 2\bar{\phi}_1^2 T \frac{4\pi^2}{3} \int_0^{N_\mathrm{T}} u^2 \mathrm{sinc}^4(u)du
$$

$$
= \frac{16}{3\pi}\left[\mathrm{Si}(2u) - \frac{\mathrm{Si}(4u)}{2} - \frac{\sin^4 u}{u}\right]\Bigg|_0^{\pi N_\mathrm{T}}
$$

where

$$
\mathrm{Si}(x) \triangleq \int_0^x \frac{\sin u}{u} du
$$

is the sine integral function function.

Fig. 4.4 presents the log-scale of $1 - \kappa$ versus number of one-sided truncated lobes. From the plot, for the same N_T, the energy of the truncated $\phi_1(t)$ is more close to 1 than that of $\phi_2(t)$. For example, $\kappa > 99.999\%$ for $\phi_1(t)$ when $N_\mathrm{T} = 10$. However, for $\phi_2(t)$ the fractional energy is only approximate 98% for the same N_T. With increased N_T, $\int_{-N_\mathrm{T}T}^{N_\mathrm{T}T} |\phi_1(t)|^2 dt$ converges rapidly to 100%. To achieve $\kappa > 99.9\%$ for the two truncated basis functions, N_T should be selected to be greater than 152.

The truncation of basis functions to $2N_\mathrm{T}$ lobes is equivalent to truncate the infinite sum in (4.17) from index $-N_\mathrm{T} + 1$ to N_T. Define the truncated sum of X^a as

$$
X_{N_\mathrm{T}}^\mathrm{a} = \sum_{i=-N_\mathrm{T}+1}^{N_\mathrm{T}} Z_i \tag{4.41}
$$

The support for $X_{N_\mathrm{T}}^\mathrm{a}$ is lower by $B_\mathrm{L} = \sum_{i=-N_\mathrm{T}+1}^{N_\mathrm{T}} \min(0, \alpha_i)$ and upper bounded by
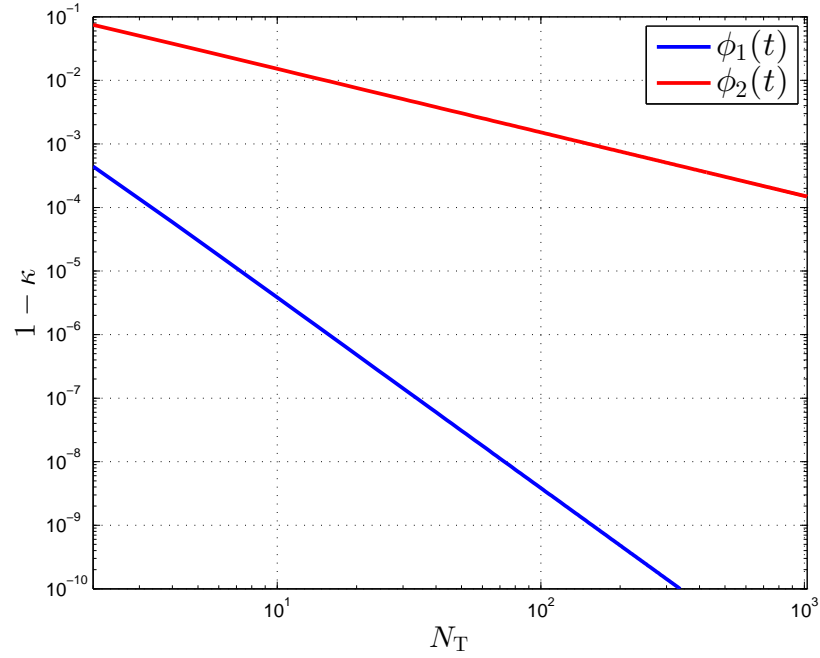
Figure 4.4: Log-scale plot of $1 - \kappa$ versus N_{T} for $\phi_1(t)$ and $\phi_2(t)$.

$B_{\mathrm{U}} = \sum_{i=-N_{\mathrm{T}}+1}^{N_{\mathrm{T}}} \beta_i$.

Let $G_{X^{\mathrm{a}}_{N_{\mathrm{T}}}}(x)$ be the ccdf of $X^{\mathrm{a}}_{N_{\mathrm{T}}}$ and it is defined as

$$G_{X^{\mathrm{a}}_{N_{\mathrm{T}}}}(x) = \mathrm{P}\left(X^{\mathrm{a}}_{N_{\mathrm{T}}} \geq x\right) = 1 - F_{X^{\mathrm{a}}_{N_{\mathrm{T}}}}(x) \quad .$$

Using [55, Eq.6], given any real λ, $F_{X^{\mathrm{a}}_{N_{\mathrm{T}}}}(\lambda)$ takes the form as

$$F_{X^{\mathrm{a}}_{N_{\mathrm{T}}}}(\lambda) = \frac{1}{2}$$
$$-\sum_{\substack{n=1 \\ n \text{ odd}}}^{\infty} \frac{\exp(-j\frac{2\pi n\lambda}{T_B}) \prod_{i=-N_{\mathrm{T}}+1}^{N_{\mathrm{T}}} \psi_i\left(\frac{2\pi n}{T_B}\right) - \exp(j\frac{2\pi n\lambda}{T_B}) \prod_{i=-N_{\mathrm{T}}+1}^{N_{\mathrm{T}}} \psi_i\left(-\frac{2\pi n}{T_B}\right)}{n\pi j}$$

(4.42)

53

where $T_B = 2\max(B_{\mathrm{U}} - \lambda, \lambda - B_{\mathrm{L}})$, j here represents the imaginary unit, and $\psi_i(\nu)$ is the characteristic function of each triangularly distributed Z_i which takes the form [57, Chp.1]

$$\psi_i(\nu) = -2\frac{(p_i^{\mathrm{u}} - p_i^{\mathrm{m}})e^{jp_i^{\mathrm{l}}\nu} - (p_i^{\mathrm{u}} - p_i^{\mathrm{l}})e^{jp_i^{\mathrm{m}}\nu} + (p_i^{\mathrm{m}} - p_i^{\mathrm{l}})e^{jp_i^{\mathrm{u}}\nu}}{(p_i^{\mathrm{u}} - p_i^{\mathrm{l}})(p_i^{\mathrm{m}} - p_i^{\mathrm{l}})(p_i^{\mathrm{u}} - p_i^{\mathrm{m}})\nu^2} \tag{4.43}$$

Substituting $\lambda = 0$ into (4.42), the likelihood $\mathrm{P}\left(X_{N_{\mathrm{T}}}^{\mathrm{a}} < 0\right)$ may be written as

$$F_{X_{N_{\mathrm{T}}}^{\mathrm{a}}}(0) = \frac{1}{2} - \sum_{\substack{n=1 \\ n \text{ odd}}}^{\infty} \frac{\displaystyle\prod_{i=-N_{\mathrm{T}}+1}^{N_{\mathrm{T}}} \psi_i\left(\frac{2\pi n}{T_B}\right) - \prod_{i=-N_{\mathrm{T}}+1}^{N_{\mathrm{T}}} \psi_i\left(-\frac{2\pi n}{T_B}\right)}{n\pi j} \tag{4.44}$$

where $T_B = 2\max(B_{\mathrm{U}}, -B_{\mathrm{L}})$.

Due to computational precision limitation of machine, it is impossible to calculate infinite series to get the likelihood in (4.44). In practice, to estimate this likelihood the summation can be calculated iteratively for $n = 1, 3, 5, \ldots$ and terminated when the absolute value of any summand is less than a predefined threshold δ. Thus, the numerical results using truncated finite series is an approximation of $\mathrm{P}\left(X^{\mathrm{a}} < 0\right)$. The performance and accuracy of the finite series will be presented and analyzed in the next part.

Simulation Results

In this section, upper bound on $\mathrm{P}\left(X^{\mathrm{a}} < 0\right)$ (4.24) using three different inequalities will be presented compared to the results using Gaussian approximation and Monte-Carlo simulations. Also the finite series is applied and the accuracy is analyzed with comparison to Monte-Carlo results.

Fig. 4.5a presents the numerically computed upper bound of $\mathrm{P}\left(R < \tau\right), \tau < 0$

compared to Gaussian approximation for a fixed $q = 0.5$ and $\varepsilon = 0.3$. The upper bound using Bhattacharyya's inequality is tighter than the results of Cantelli's inequality since higher order moments are introduced. The bound applying Hoeffding's inequality is loose compared to other two inequalities over $\tau \in [0.4, 0]$ and becomes tighter with decreased τ. Fig. 4.5b depicts the upper bound of $\mathrm{P}\,(X^{\mathrm{a}} < 0)$ via applying three different inequalities as a function of q and $\varepsilon = 0.3$ with $N_{\mathrm{T}} = 128$. In general, the highest $\mathrm{P}\,(X^{\mathrm{a}} < 0)$ occurs at $q = 0.5$ for all methods. Among the three upper bound, the Bhattacharyya's inequality is tightest. However, there exists a gap with the order of approximate 10^3 between the Bhattacharyya's upper bound and Monte-Carlo simulation results. The Gaussian approximation is closest to the Monte-Carlo results for all q.

Fig. 4.6a presents $\mathrm{P}\,(X^{\mathrm{a}} < 0)$ as a function of ε for a variety of q estimated via Monte-Carlo simulations and via finite series (4.44) with $N_{\mathrm{T}} = 128$ and $\delta = 10^{-20}$. Fig. 4.6b is the plot of $\mathrm{P}\,(X^{\mathrm{a}} < 0)$ as a function of q for a fixed ε. The Monte-Carlo simulations were performed with identically truncated $\phi_1(t)$ and $\phi_2(t)$ and repeated 10^9 times for each given ε and q. Numerical results indicate that the estimates of $\mathrm{P}\,(X^{\mathrm{a}} < 0)$ using series and Monte-Carlo simulations match closely, suggesting finite series (4.44) is a good and accurate estimate.

Notice that for all ε, the worst case, i.e. the maximum likelihood of negative amplitude excursion occurs at $q = 0.5$. For any given ε, as q decreases to 0, the likelihood of clipping also tends to zero as analyzed in Chap. 3.1 since X^{a} is guaranteed to be non-negative when $\varepsilon \to 0$. For a given q, the likelihood of negative amplitude excursion increase rapidly with ε. Larger values of ε lead to more negativity introduced into $X^{\mathrm{a}}(q)$ which is consistent to the description in Chap. 3.1. Thus, for any q, Fig. 4.6
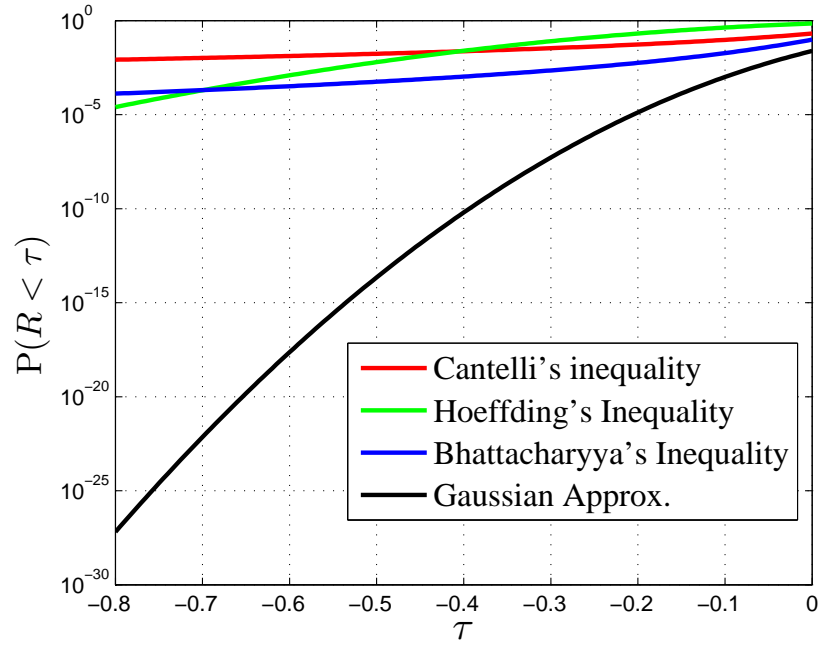
(a) Upper bound of $P(R < \tau)$ and Gaussian approximation.
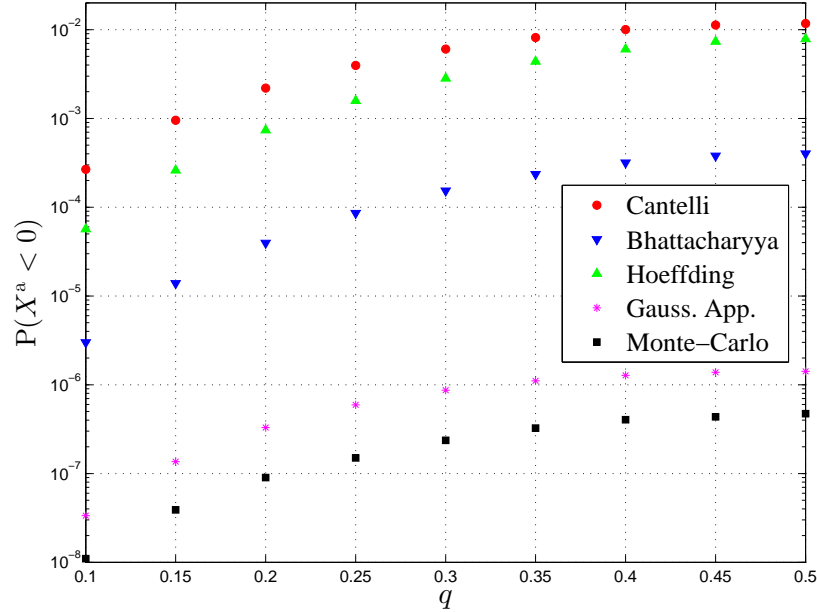
(b) Upper bound of $P(X^a < 0)$ and results using Gaussian approximation and Monte-Carlo simulations.

Figure 4.5: (a) Upper bound of $P(R < \tau), \tau < 0$ using three inequalities, and Gaussian approximation for a fixed $\varepsilon = 0.3$ and $q = 0.5$; (b) Upper bound of $P(X^a < 0)$ using Cantelli's, Bhattacharyya's, and Hoeffding's inequality, and results using Gaussian approximation and Monte-Carlo simulations as a function of q for a fixed $\varepsilon = 0.3$.
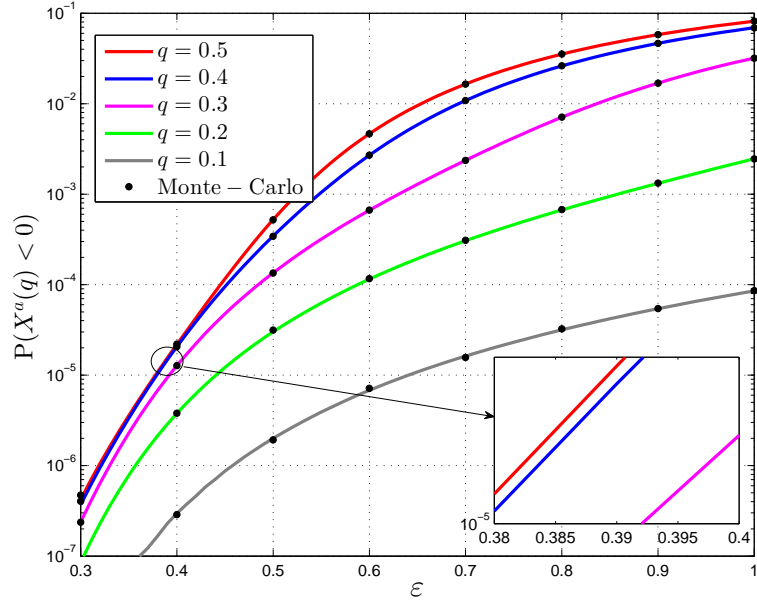
(a) $\mathrm{P}\left(X^{\mathrm{a}}(q) < 0\right)$ as a function of ε for a given q.
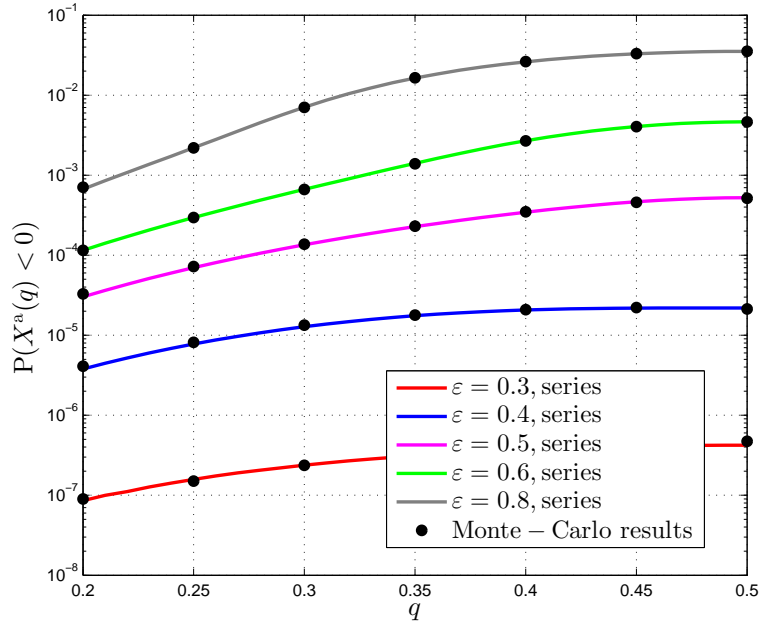
(b) $\mathrm{P}\left(X^{\mathrm{a}}(q) < 0\right)$ as a function of q for a given ε.

Figure 4.6: (a) Likelihood of negative amplitude excursion as a function of ε for a fixed $q \in \{0.1, 0.2, 0.3, 0.4, 0.5\}$; (b) Likelihood of negative amplitude excursion as a function of q for a given $\varepsilon \in \{0.3, 0.4, 0.5, 0.8\}$.

57

quantifies the trade-off between increasing the spectral efficiency of the lattice code (through increasing ε) and the amount of clipping distortion introduced (as measured by the likelihood of clipping). For example, when $\varepsilon \leq 0.4$, $P\left(X^{\mathrm{a}} < 0\right) < 10^{-4}$ for all q, and as shown in Chap. 5, the impact of clipping distortion on system performance is negligible for selected ε.

In addition, the complexity in terms of MATLAB script running time of the finite series approach is much lower than that of Monet-Carlo simulations. As an example, the running time to get numerical computation results using series approach for a fixed $\varepsilon = 0.5$, $N_{\mathrm{T}} = 128$ and $\delta = 10^{-20}$ (the magenta solid curve in Fig. 4.6b) is less than 8 seconds while the time consumption to get Monte-Carlo simulations (black solid circles in Fig. 4.6b) requires several hours. The platform to run script is a laptop equipped with Intel Core i5-2410M 2.3GHz dual-core processors and 8 GB 1333MHz memory.

4.2.3   Peak Amplitude Constraint: $P(x(t) < 0 \cup x(t) > p\hat{\phi}_1)$

In an analogous fashion to Chap. 4.2.1, the likelihood of clipping in the peak limited channel is quantified here when signals are selected from the bounded region $\Upsilon_\varepsilon \cap \Pi_\varepsilon(p)$. All the results are computed merely by using series method due to its good performance. Firstly, define

$$
X^{\mathrm{p}}(q) \;=\; \sum_{i=-\infty}^{\infty} a_i \varphi_{1,i}(q) + b_i \varphi_{2,i}(q) \tag{4.45}
$$

$$
\;=\; \sum_{i=-\infty}^{\infty} Z_i(q) \tag{4.46}
$$
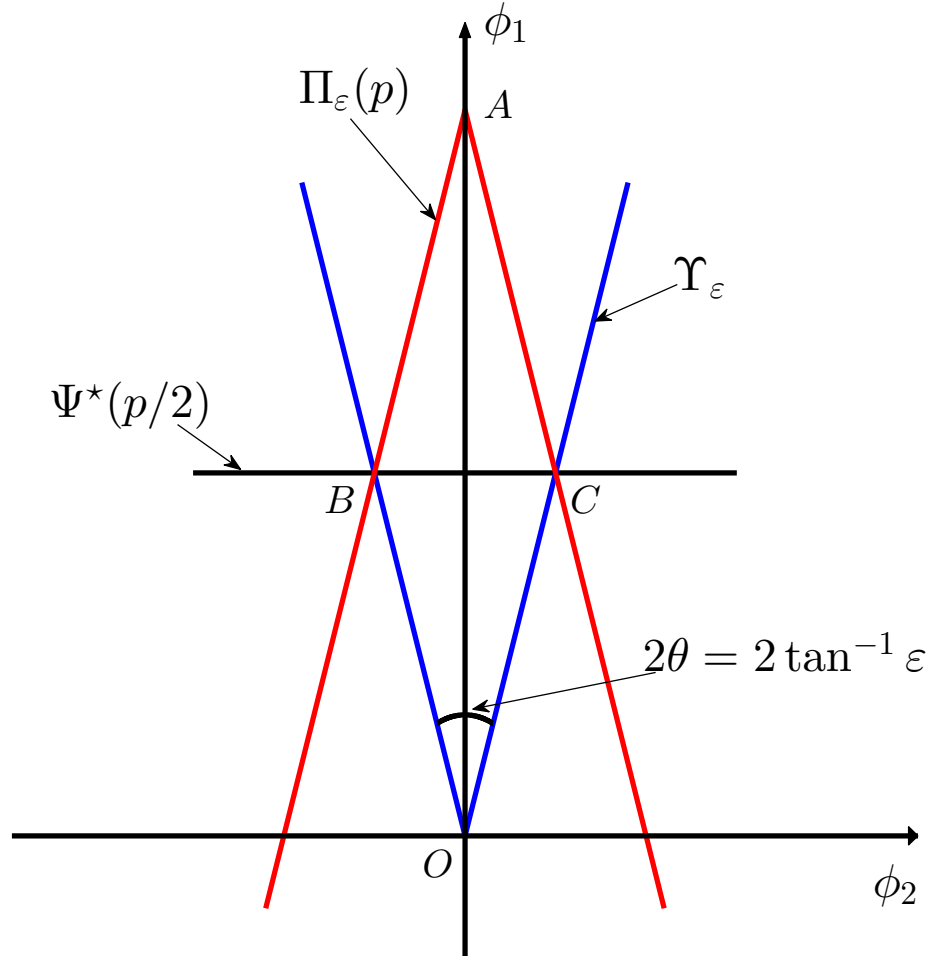
Figure 4.7: Essentially non-negative and peak-limited bounding regions. The rhombus $ABOC$ is $\Upsilon_\varepsilon \cap \Pi_\varepsilon(p)$ while the triangle BOC is $\Upsilon_\varepsilon \cap \Psi^\star(p/2)$.

where $(a_i, b_i) \in \Upsilon_\varepsilon \cap \Pi_\varepsilon(p)$ are chosen independently and equally likely over the region. Thus, employing the continuous approximation, the following theorems bound $\mathrm{P}(X^{\mathrm{p}}(q) < 0 \cup X^{\mathrm{p}}(q) > p\hat{\phi}_1)$.

Theorem 1. *For a given ε and any $h, p > 0$,*

$$\mathrm{P}(X^{\mathrm{a}}(q) < 0) \geq \mathrm{P}(X^p(q) < 0).$$

Proof. Consider the regions depicted in Figure 4.7. For any point $(a_r, b_r) \in \Upsilon_\varepsilon \cap \Psi^\star(p/2)$, i.e., triangle BOC, there exists a "mirror" point (a_m, b_m) in triangle ABC, where $b_r = b_m$ and $a_m + a_r = p$. Notice that $\forall t \in \mathbb{R}$

$$a_r \phi_1(t) + b_r \phi_2(t) \leq a_m \phi_1(t) + b_m \phi_2(t) \tag{4.47}$$

that is, the signals corresponding to points in triangle ABC are *more positive* than those in BOC.

Consider selecting points uniformly and independently over $\Upsilon_\varepsilon \cap \Psi^\star(p/2)$ with resulting probability of negative excursion $\mathrm{P}(X^a(q) < 0)$. Additionally, consider splitting the elemental probability associated to every point in triangle BOC with its mirrored counterpart in triangle ABC. Clearly, this results in points being selected uniformly and independently over $\Upsilon_\varepsilon \cap \Pi_\varepsilon(p)$. In addition, since every mirror point is necessarily more positive, as noted in (4.47), the likelihood of negative excursion, i.e., $\mathrm{P}(X^p(q) < 0)$, must be reduced. □

Theorem 2. *If $\Omega \subseteq \Upsilon_\varepsilon \cap \Pi_\varepsilon(p)$ is symmetric about both ϕ_1-axis and $\Psi^\star(p/2)$, and points are chosen independently and equiprobably then*

$$\mathrm{P}(X^p(q) < 0) = \mathrm{P}(X^p(q) > p\hat{\phi}_1) \quad .$$

Proof. Since Ω is symmetric about ϕ_1-axis and $\Psi^\star(p/2)$, Ω is an affine transform of itself, i.e. $\Omega = -\Omega + p\vec{\phi}_1$, where $\vec{\phi}_1$ is a unit vector in ϕ_1 direction. Thus, following

are equivalent events

$$
\begin{aligned}
\mathrm{P}(X^p(q) < 0) &= \mathrm{P}(-X^p(q) > 0) \\
&= \mathrm{P}(-X^p(q) + p\hat{\phi}_1 > p\hat{\phi}_1) \\
&= \mathrm{P}(X^p(q) > p\hat{\phi}_1)
\end{aligned}
$$

where the last step arises since $\sum_i \phi_1(t - iT) = \hat{\phi}_1$ [61]. $\square$

Since the events $\{X^p(q) < 0\}$ and $\{X^p(q) > p\hat{\phi}_1\}$ are disjoint, the likelihood of their union is the sum of probabilities. Additionally, via Thm. 2, the likelihood of the two events are identical.

Finite Series Approach

An approximation of $\mathrm{P}(X^p(q) < 0)$ can be computed via [55], as in Sec. 4.2.1, using a finite series under both non-negativity and peak optical power constraints. The minimum and maximum possible value of $Z_i(q)$ for a given q and ε can also be obtained via linear programming

$$
\text{minimize/maximize} \quad \varphi_{1,i}(q)a_i + \varphi_{2,i}(q)b_i \tag{4.48}
$$

$$
\text{subject to} \quad (a_i, b_i) \in \Upsilon_\varepsilon \cap \Pi_\varepsilon(p) \quad . \tag{4.49}
$$

Fig. 4.8 illustrates the linear programming of $\varphi_{1,i}(q)a_i + \varphi_{2,i}(q)b_i$ with the constraint (a_i, b_i) selected from region $\Upsilon_\varepsilon \cap \Pi_\varepsilon(p)$ for any given q and $\varepsilon > 0$. The maximum possible value of $Z_i(q)$, i.e. upper limit of the support, is obtained corresponding to
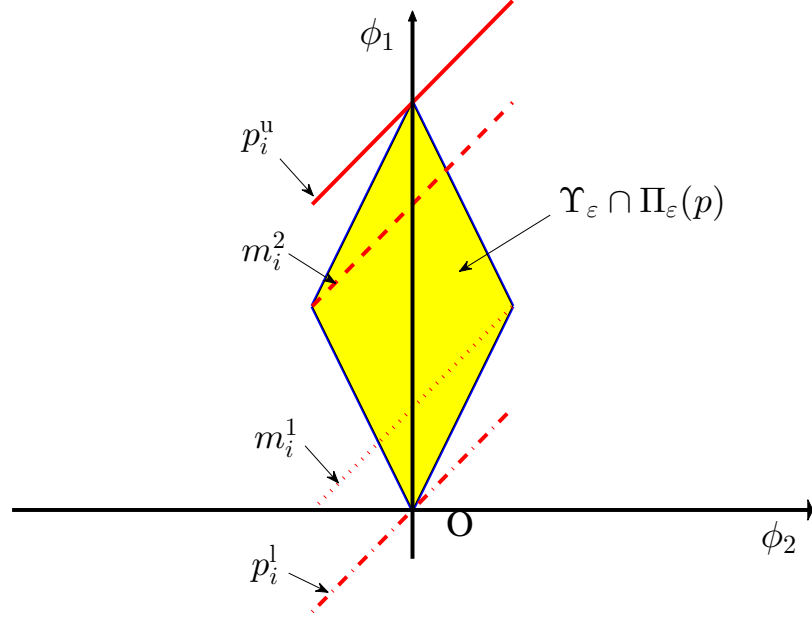
Figure 4.8: Linear programming of $\varphi_{1,i}(q)a_i + \varphi_{2,i}(q)b_i$ subject to the constraint $(a_i, b_i) \in \Upsilon_\varepsilon \cap \Pi_\varepsilon(p)$ for a fixed q and ε.

the red solid line. Similarly, the lower limit, left mode, and right mode points correspond to the dashed-dot, dot, and dashed lines respectively. From a geometric view, it is clear that each Z_i in this case has an isosceles trapezoidal distribution [66] as illustrated in Fig. 4.9. Hereafter, q is omitted for simplicity.

The characteristic function of each Z_i can be shown to take the for

$$\psi_i(\nu) = \frac{\xi_i}{\nu^2} \left[\frac{e^{jm_i^1\nu} - e^{jp_i^l\nu}}{m_i^1 - p_i^l} - \frac{e^{jp_i^u\nu} - e^{jm_i^2\nu}}{p_i^u - m_i^2} \right] \tag{4.50}$$

where we define

$$\gamma_i = \frac{p}{2}\left(\varphi_{1,i} - \varepsilon\left|\varphi_{2,i}\right|\right)$$
$$\rho_i = \frac{p}{2}\left(\varphi_{1,i} + \varepsilon\left|\varphi_{2,i}\right|\right)$$
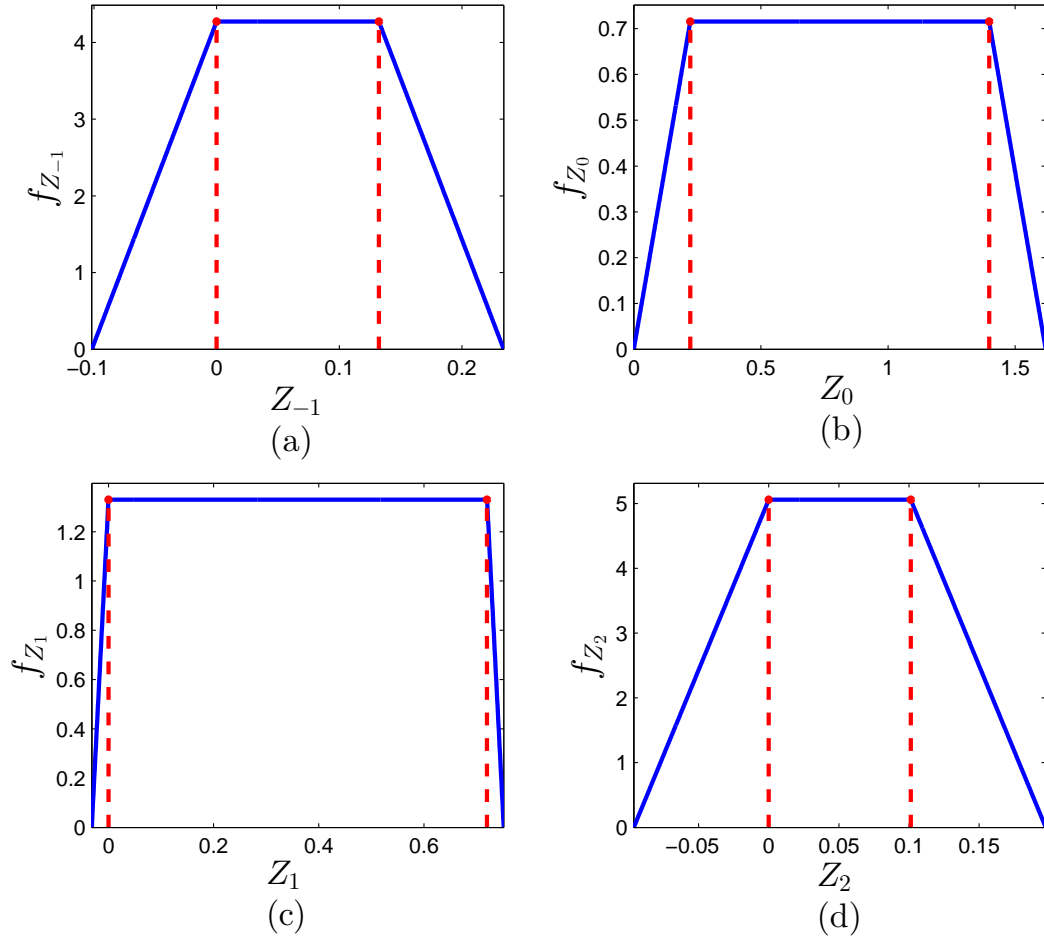
Figure 4.9: pdf of trapezoidal distributed $Z_i, i \in \{-1, 0, 1, 2\}$ for a fixed $\varepsilon = 0.5, q = 0.4$, and $T = 1$. Applying the continuous approximation, each (a_i, b_i) is selected uniformly and independently from $\Upsilon_\varepsilon \cap \Pi_\varepsilon(2)$.

and parameters $\xi_i = 2/(p_i^{\mathrm{u}} + m_i^2 - m_i^1 - p_i^{\mathrm{l}})$, $p_1 = \min(0, \gamma_i)$, $p_2 = \max(\rho_i, p\phi_{1,i})$, $m_1 = \max(0, \gamma_i)$, and $m_2 = \min(\rho_i, p\phi_{1,i})$ are the lower limit, upper limit, left mode, and right mode point of Z_i. A similar series approximation can also be formulated to compute $\mathrm{P}(X^{\mathrm{p}} > p\hat{\phi}_1)$ as (4.44).
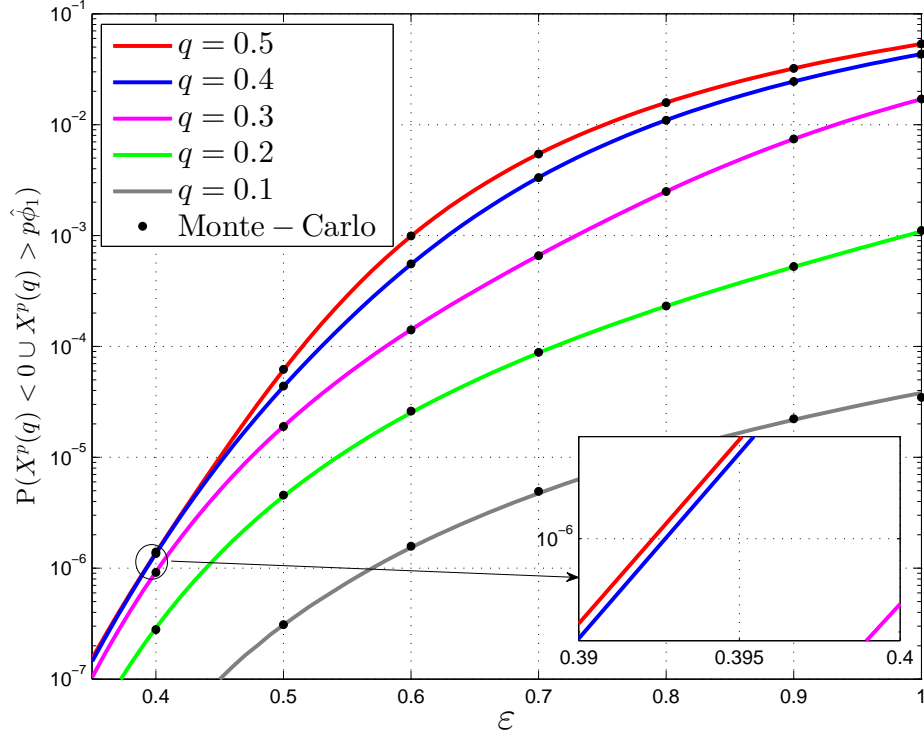
Figure 4.10: Comparison of $P(X^p(q) < 0 \cup X^p(q) > p\hat{\phi}_1)$ as a function of ε for a fixed $q \in \{0.1, 0.2, 0.3, 0.4, 0.5\}$ using Monte-Carlo simulations and finite series with $N_T = 128$. Symbols are selected independently and equally likely over $\Upsilon_\varepsilon \cap \Pi_\varepsilon(p)$.

Simulation Results

In this part, only finite series approach is utilized to compute the approximation of likelihood of clipping under the peak amplitude constraint.

Fig. 4.10 presents $P(X^p < 0 \cup X^p > p\hat{\phi}_1)$. The parameters used for these results are identical to those in Sec. 4.2.1. Notice that the results from Monte-Carlo simulations closely match those computed via the series approximation. The results have a similar behaviour to $P(X^a < 0)$ in Fig. 4.6 with the likelihood of clipping rising with increasing ε and having a maximum for $q = 0.5$.

Comparing Fig. 4.6a to Fig. 4.10, for a given q and ε, it is apparent that $P(X^a <$

$0) > \mathrm{P}(X^{\mathrm{p}} < 0 \ \cup \ X^{\mathrm{p}} > p\hat{\phi}_1)$ which is in fact a stronger bound than that in Thm. 1.

4.3 Summary

In this chapter, essentially non-negative and peak-limited lattice codes under average and peak amplitude constraints are defined for IM/DD channels. Asymptotic average and peak optical power efficiency in the limit $P_{\mathrm{e}} \to 0$ and spectral efficiency applying the continuous approximation are derived. All the computations are based on the assumption that the clipping distortion introduced into system is negligible.

The likelihood of clipping under average and peak optical power constraints are computed. Three different inequalities are applied to numerically compute the upper bound of $\mathrm{P}\left(x(t) < 0\right)$ under average optical power constraint and it is shown that Bhattacharyya's inequality provides the tightest bound. The results applying finite series approach to compute the approximation of likelihood of clipping under average and peak amplitude constraints match closely to the Monte-Carlo simulation results and the running time of this method is tolerable. In Chap. 5, numerical system simulations and its performance analysis will be presented.

Chapter 5

Performance Analysis

This chapter presents examples of essentially non-negative lattice codes formed via the intersection of a two-dimensional hexagonal lattice A_2,

$$\left\{ (a, b) = d_{\min} \cdot (m, n) \begin{pmatrix} 1 & 0 \\ 1/2 & \sqrt{3}/2 \end{pmatrix}, (m, n) \in \mathbb{Z}^2 \right\}$$

and bounded region defined in Chap. 3.2 or 3.3 depending on different constraints. Notice that the fundamental volume of the lattice is $V(A_2) = \frac{\sqrt{3}}{2} d_{\min}^2$. Non-negative M-PAM using S2, parametric linear (PL) [67] and raised-cosine (RC) Nyquist pulses with sampling receiver in [32] are also presented as reference schemes. The impact of clipping distortion is quantified through Monte-Carlo simulations under both average and peak amplitude constraints.

5.1   Results under Average Optical Power Constraint

In this part, Monte-Carlo simulation results are presented to analyze the signaling scheme performance under average optical power constraint. DC bias is introduced to reduce the clipping distortion but increase the radiated optical power as well. Thus, the trade-off between power efficiency and impact of clipping distortion is also quantified in this part.

5.1.1   Performance without Added DC Bias

Figure 5.1 presents the average optical power gain (4.3) versus spectral efficiency (4.1) for reference schemes and essentially non-negative hexagonal lattice codes. Notice that the strict non-negativity constraint is satisfied for schemes of M-PAM using PL and RC pulses by adding DC bias. S2 M-PAM scheme implies the inherent non-negativity since S2 pulse is non-negative for all t. Thus, the three reference schemes are not impacted by the clipping process of the optical modulator model (2.5). All discrete constellations points were constructed following (4.2) using the A_2 lattice with translate $\mathbf{t} = \mathbf{0}$.

To estimate $\overline{P}_\mathrm{o}$ for the discrete constellations, Monte-Carlo simulations were performed in MATLAB [68]. Constellation points were selected independently and equiprobably from Ω^a and a ten times oversampled estimate of $x(t)$ is generated via (2.4). All negative amplitude excursions of the resulting $x(t)$ are clipped at zero following (2.5). In addition, the basis functions and receive filters are truncated to $N_\mathrm{T} = 512$ one-sided lobes. The average optical power gain is numerically computed via (4.3) and quantifies the excess optical power needed over the baseline to achieve a bit error rate of $P_\mathrm{e} \approx 10^{-6}$. The spectral efficiency for the discrete essentially
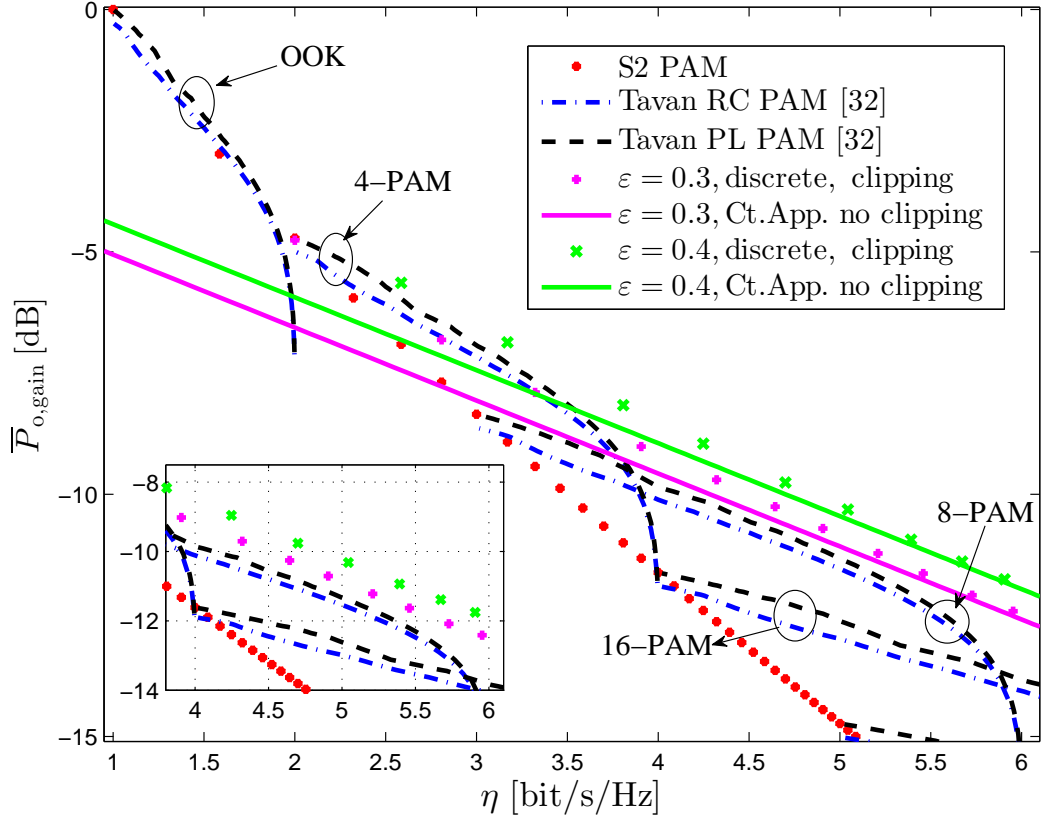
Figure 5.1: Average optical power gain versus spectral efficiency using essentially non-negative hexagonal lattice codes for $P_e \approx 10^{-6}$ without added DC bias, $\varepsilon = \{0.3, 0.4\}$.

non-negative lattice codes is computed using the definition in (4.1).

The solid red circles represent the power versus spectral efficiency using the scheme of one-dimensional M-PAM with S2 pulse and sampling receiver. The black and blue dashed curves represent the power versus spectral efficiency using the M-PAM PL and M-PAM RC schemes, respectively, where $M \in \{2, 4, 8, 16\}$. The average optical power gain for M-PAM PL and RC schemes are plotted using the closed form expressions in Tavan's paper [32] and by varying the excess bandwidth parameter. The magenta and green solid lines are the asymptotic average optical power gain versus spectral efficiency curves using the hexagonal lattices for $\varepsilon = 0.3$ and $\varepsilon = 0.4$,

respectively. The continuous approximation (Ct.App.) is applied to compute the asymptotic average optical power gain (4.9) and spectral efficiency (4.10) under the assumption of negligible clipping impact for the computation of such asymptotic curves. The magenta and green discrete plots are the numerically computed average optical power gain using hexagonal lattice codes versus spectral efficiency by taking the clipping into consideration for $\varepsilon = 0.3$ and $\varepsilon = 0.4$, respectively.

From Fig. 5.1, essentially non-negative hexagonal lattice codes have an average optical power gain over previous approaches. Comparing to M-PAM scheme using the S2 pulse, a gain of more than 3 dB can be achieved for $\varepsilon = 0.4$ when $\eta > 3.8$ bit/s/Hz and similar gains are achieved for $\varepsilon = 0.3$ when $\eta > 4.6$ bit/s/Hz. Notice that the power gain of essentially non-negative lattice codes over M-PAM S2 scheme increase rapidly with rising spectral efficiency.

For strictly non-negative PL and RC PAM schemes, essentially non-negative lattice codes are more power efficient especially for large η. The gain of essentially non-negative lattice over PL PAM scheme can be obtained for $\varepsilon = 0.4$ when $\eta > 2.5$ and for $\varepsilon = 0.3$ when $\eta > 3.9$. At a spectral efficiency of approximately 5.9, essentially non-negative lattice codes realize an approximate 2 dB gain over $16-$PAM PL scheme for $\varepsilon = 0.4$. Notice that the gain of essentially non-negative lattice codes over RC and PL techniques also grows with increasing η.

For comparison, the asymptotic average optical power gains are plotted in Fig. 5.1 versus spectral efficiency (4.10). Notice also, that as expected, the continuous approximation is loose for small η and becomes increasingly accurate for higher spectral efficiencies, i.e. larger size of constellation. These approximations may, thus, be useful in estimating optical power gain in VLC systems which are bandlimited and operate
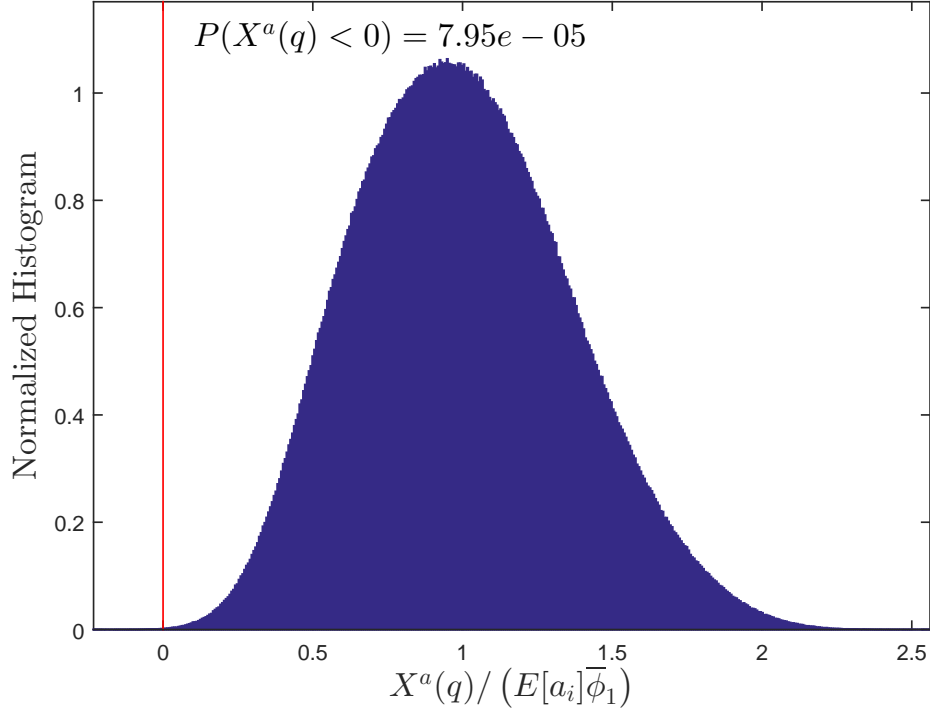
Figure 5.2: Normalized histogram of $X^{\mathrm{a}}(q)/(\mathrm{E}\,[a_i]\,\overline{\phi}_1)$ using a discrete constellation constructed by essentially non-negative hexagonal lattices for a given $q = 0.5$ and $\varepsilon = 0.4$ at $\eta = 5.91$.

at high spectral efficiencies.

To visualize the impact of clipping distortion, Fig. 5.2 presents an example of the normalized histogram of $X^{\mathrm{a}}(q)/(\mathrm{E}\,[a_i]\,\overline{\phi}_1)$ for a discrete constellation for a fixed $q = 0.5$ and $\varepsilon = 0.4$ at spectral efficiency $\eta = 5.91$ (i.e., $|\Omega^{\mathrm{a}}| = 60$). The conditions of the simulation are identical to those used to compute the average optical power gain in Figure 5.1 to achieve a BER of 10^{-6}. Notice that the likelihood of negative excursion for this discrete constellation is approximately 8×10^{-5}. This is in close agreement to the estimate of 2×10^{-5} in Fig. 4.6 which was found via the continuous approximation.

5.1.2   Performance with Added DC Bias

The selection of ε is a critical parameter governing the performance of our scheme. Larger ε increases the spectral efficiency by providing more degrees of freedom for modulation and thus increasing $|\Omega^{\mathrm{a}}|$. However, clipping distortion also increases with larger ε as evidenced by the increase of $\mathrm{P}(X^{\mathrm{a}}(q) < 0)$ in Fig. 4.6. In particular, we have noticed that clipping distortion becomes sufficiently severe to eliminate any gains over previous approaches for $\varepsilon \geq 0.5$.

An intuitive approach to reduce the impact of clipping distortion is to decrease the likelihood of negative amplitude excursion under average amplitude constraint. This can be realized via adding a constant bias component μ_0 to electrical current signal $x(t)$. Fig. 5.3 presents a normalized histogram of $X^{\mathrm{a}}(q)/(\mathrm{E}\,[a_i]\,\overline{\phi}_1)$ for a given $q = 0.5$ and $\varepsilon = 0.4$ with $N_{\mathrm{T}} = 128$ applying the continuous approximation without added DC bias. Each symbol (a_i, b_i) in Monte-Carlo simulations is assumed to be selected independently and uniformly from region $\Upsilon_\varepsilon \cap \Psi^\star(h)$. Since a_i satisfies a triangular distribution, $\mathrm{E}\,[a_i] = 2h/3$ [57].

The clipping distortion is indeed reduced by increasing DC component. However, this part of constant bias does not carry any information but increases the instantaneous radiated optical power. Thus, the average optical power efficiency decreases with increasing bias and there exists a trade-off between clipping distortion and average optical power efficiency.

Denote $x_{\mathrm{b}}(t)$ as the current signal generated in (2.4) plus a DC bias μ_0. Since
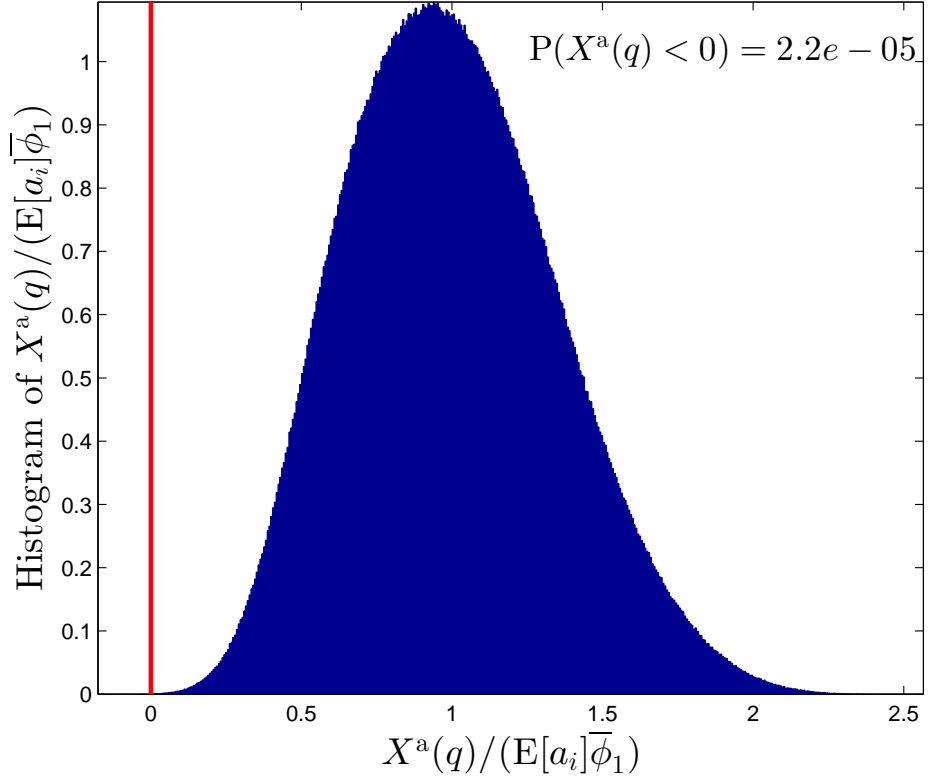
Figure 5.3: Normalized histogram of $X^{\mathrm{a}}(q)/(\mathrm{E}\,[a_i]\,\overline{\phi}_1)$ for a given $q = 0.5$ and $\varepsilon = 0.4$ with $N_{\mathrm{T}} = 128$ by applying the continuous approximation without added DC bias.

$\sum_i \phi_1(t - iT) = \sqrt{2/T} = \overline{\phi}_1,$

$$
\begin{aligned}
x_{\mathrm{b}}(t) &= \mu_0 + \sum_{i=-\infty}^{\infty} a_i \phi_1(t - iT) + b_i \phi_2(t - iT) & (5.1) \\
&= \sum_{i=-\infty}^{\infty} (a_i + \mu_0/\overline{\phi}_1)\phi_1(t - iT) + b_i \phi_2(t - iT) & . \quad (5.2)
\end{aligned}
$$

The geometric interpretation of adding bias μ_0 to $x(t)$ in the above equation is the up-shifting of constellation Ω^{a} by $\mu_0/\overline{\phi}_1$ in ϕ_1-axis. Since μ_0 is a constant, the pdf of $x_{\mathrm{b}}(t)$ in (5.1) is definitely right-shifted of the pdf of $x(t)$ in (2.4) by μ_0 for a fixed t. Thus, the likelihood of negative amplitude excursion is decreased via adding
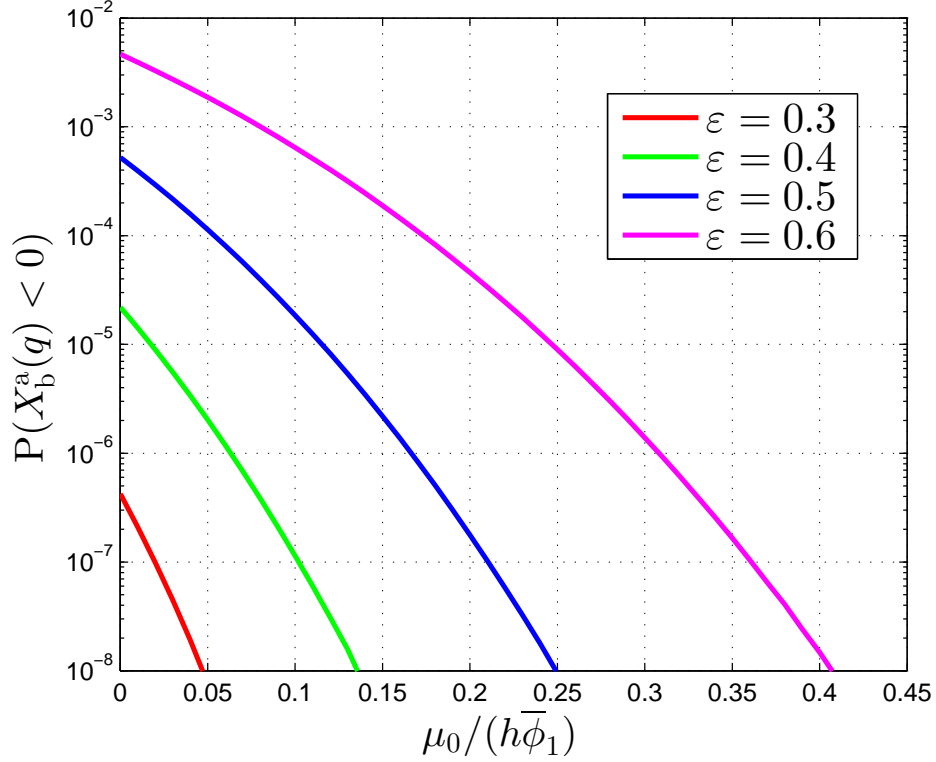
Figure 5.4: Likelihood of negative amplitude excursion as a function of normalized DC bias for a given $q = 0.5$ and $\varepsilon \in \{0.3, 0.4, 0.5, 0.6\}$.

DC bias.

To compute the likelihood of clipping after adding bias, define

$$X_{\text{b}}^{\text{a}}(q) = X^{\text{a}}(q) + \mu_0 \quad .$$

Since $P\left(X_{\text{b}}^{\text{a}}(q) < 0\right) = P\left(X^{\text{a}} < -\mu_0\right)$, the likelihood of negative amplitude excursion with DC bias can be computed directly via substituting $\lambda = -\mu_0$ into (4.42).

Fig. 5.4 presents the likelihood $P\left(X_{\text{b}}^{\text{a}}(q) < 0\right)$ as a function of normalized bias for a given $q = 0.5$ and variety of ε applying continuous approximation, where (a_i, b_i) is selected independently and uniformly from $\Upsilon_\varepsilon \cap \Psi^\star(h)$, $h > 0$. For $\varepsilon = 0.5$, the

Figure 5.5: Average optical power gain versus spectral efficiency using essentially non-negative hexagonal lattice codes for $P_e \approx 10^{-6}$, no DC bias for $\varepsilon \in \{0.3, 0.4\}$ and DC bias is added for $\varepsilon = 0.5$.

likelihood of negative amplitude excursion is improved from approximate 5×10^{-4} without added DC component to 10^{-5} by adding $\mu_0 \approx 0.12 h\overline{\phi}_1$. For a given ε, bit error rate, and constellation set, there exists an optimal DC bias, which provides the maximum possible average optical power gain. This optimization is difficult to solve analytically but simple to implement numerically.
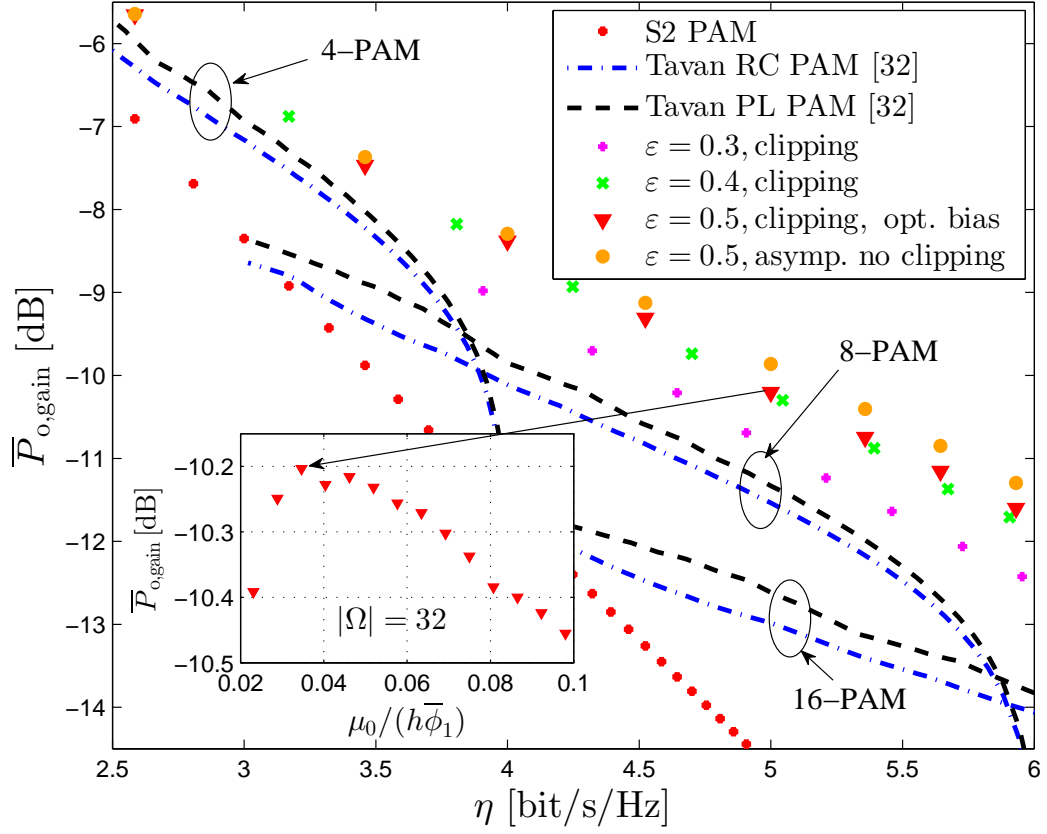
Fig. 5.5 presents the average optical power gain versus spectral efficiency using essentially non-negative hexagonal lattice codes to achieve $P_e \approx 10^{-6}$ with and without added DC bias. The magenta and green discrete plots are power versus spectral

efficiency for $\varepsilon = 0.3$ and $\varepsilon = 0.4$ without added DC bias, respectively, as the same in Fig. 5.1. The red triangular plots represent the average optical power gain versus spectral efficiency with a numerically searched optimal DC bias at each different η. For example, the sub-figure illustrates the average optical power gain versus normalized DC bias for a given $P_e \approx 10^{-6}$, $\varepsilon = 0.5$, and $\eta = 5$. The optimal normalized bias is approximate 0.036 and the achieved average optical power gain over baseline is -10.21 dB.

In addition, the discrete orange circles are the asymptotic average optical power gain as $P_e \to 0$ versus spectral efficiency using essentially non-negative hexagonal lattice codes under assumption of negligible clipping distortion for $\varepsilon = 0.5$ without added DC bias. This asymptotic average optical power gain of hexagonal lattice takes the form,

$$\overline{P}_{\text{o,gain}}(\Omega^{\text{a}})\big|_{P_e \to 0} = \frac{1}{2\mathrm{E}\left[a_i/d_{\min}(\Omega^{\text{a}})\right]} \quad .$$

where a_i is the component of each lattice code in ϕ_1-axis. The gain over M-PAM PL scheme can be achieved for $\varepsilon = 0.5$ by adding an optimal DC bias at $\eta > 2.5$. For example, a gain of 0.5 dB over 4-PAM PL scheme is obtained at $\eta = 3.46$. The result using hexagonal lattice with optimal bias is close to the asymptotic average optical power gain and thus the clipping distortion does not impact the power efficiency a lot. Additionally, an approximate 1.3 dB and 1.1 dB gain over 8-PAM PL scheme is achieved at $\eta = 4$ and $\eta = 5$, respectively. For $\eta > 5$, the power efficiency performance by adding bias for $varepsilon = 0.5$ is close to that without DC bias for $\varepsilon = 0.4$. However, schemes using essentially non-negative lattice codes with optimal DC bias for $\varepsilon = 0.5$ are still more power efficient than those for $\varepsilon = 0.4$ without bias. Notice also, that there is still an approximate 2.1 dB gain over 16-PAM PL scheme

at $\eta = 5.91$ for $\varepsilon = 0.5$ with bias.

5.2   Results under Peak Optical Power Constraint

In a similar fashion to Chap. 5.1, the gain of essentially peak-limited lattice codes over existing techniques is given in Fig. 5.6. The lattice codes are constructed as in (4.11) using the region $\Upsilon_\varepsilon \cap \Pi_\varepsilon(p)$ and ensuring that there exists one lattice at peak vertex, i.e $(p, 0)$. This was done to ensure the symmetry of the constellations and to ensure that the peak optical power of the lattice scheme is $p\hat{\phi}_1$.

For strictly non-negative schemes M-PAM using S2, PL and RC pulses, the peak optical power gain is equivalent to the average optical power gain due to constellation symmetricity [32, Thm.4]. This statement is also true for the essentially peak-limited lattice codes in this thesis under the assumption that the likelihood of clipping $P(x(t) < 0 \cup x(t) > p\hat{\phi}_1)$ is negligible and the lattice constellation is strictly symmetric about ϕ_1-axis and $\Pi_\varepsilon(h/2)$.

Fig. 5.6 illustrates the simulation results of peak optical power gain versus the spectral efficiency for a fixed ε and $P_e \approx 10^{-6}$. These results were obtained in the same manner as described in Sec. 5.1 using the negative and peak amplitude clipping modulation model in (2.10).

Notice that when $\eta > 4$, essentially peak-limited lattice codes have a significant peak optical power gain over the S2 M-PAM scheme for $\varepsilon \in \{0.3, 0.4, 0.5\}$. For $\eta > 3.5$, gains over 4-, 8-, and 16-PAM schemes using the PL pulse are realized. In general, the peak optical power gains of the designed hexagonal lattice codes increase with η. For example, for $\varepsilon = 0.5$ and $\eta > 6$, essentially peak-limited lattice codes provide more than 2 dB gain over the 16-PAM PL scheme. Notice additionally
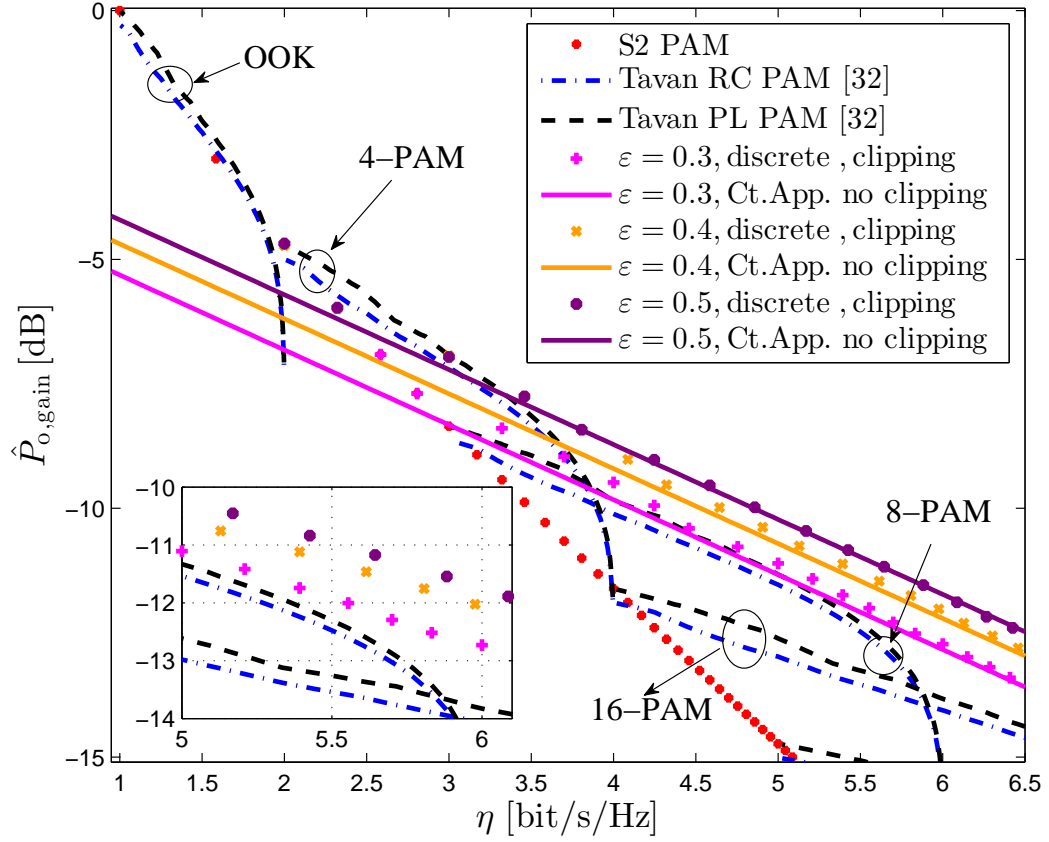
Figure 5.6: Peak optical power gain versus spectral efficiency using essentially peak-limited hexagonal lattice codes for $\varepsilon \in \{0.3, 0.4, 0.5\}$ and reference schemes for a given $P_e \approx 10^{-6}$.

that the performance of the discrete essentially peak-limited lattice codes is closely predicted at high η by (4.13) and (4.14) derived in Chap. 4 by applying the continuous approximation.

Another important feature to note is that larger values of ε can be used to construct essentially peak-limited lattice codes than for the average optical power constraint in Sec. 5.1. Indeed, this fact is clear since for a given ε, the likelihood of clipping is smaller in the peak-limited case as seen in Figs. 4.6 and 4.10.

The normalized histogram of $X^p(q)/(p\hat{\phi}_1)$ at $q = 0.5$ is plotted in Fig. 5.7 for
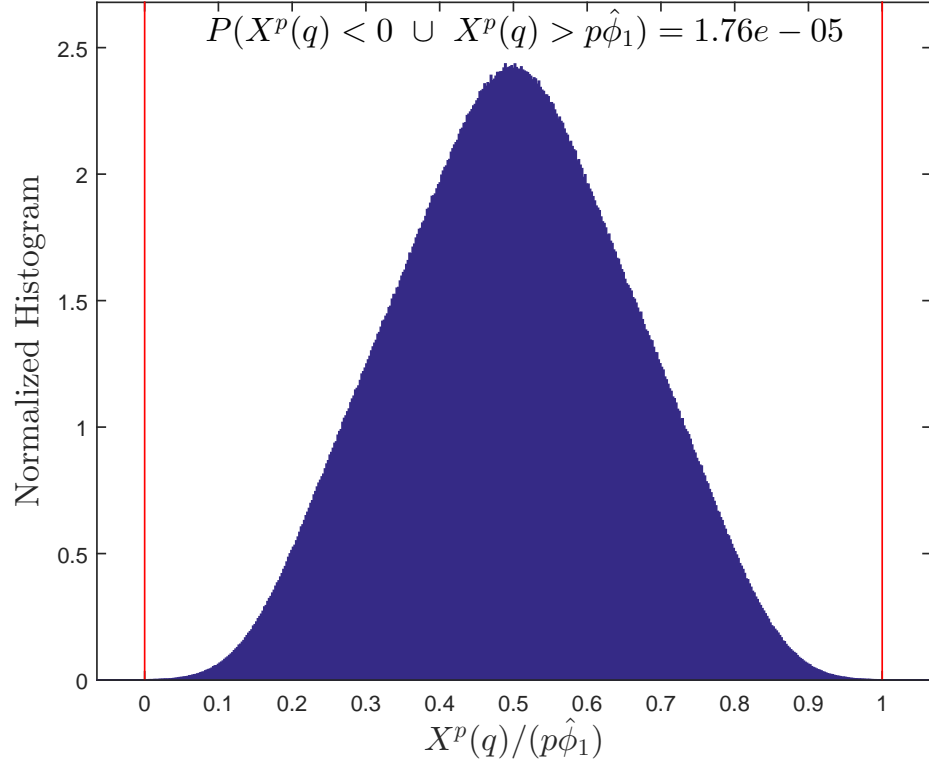
Figure 5.7: Normalized histogram of $X^{\mathrm{p}}(q)/(p\hat{\phi}_1)$ using a discrete constellation constructed by essentially peak-limited hexagonal lattices for a given $q = 0.5$ and $\varepsilon = 0.4$ at $\eta = 5.97$.

$\varepsilon = 0.4$ and spectral efficiency $\eta = 5.97$ (i.e., $|\Omega^{\mathrm{p}}| = 63$). The simulation to compute the histogram was done with identical conditions as for those in Fig. 5.6. The resulting distribution is symmetric and has approximately equal likelihood of clipping on negative and positive sides (as required in Thm. 2). Additionally, this plot numerically validates Thm. 1 which demonstrates that essentially peak-limited lattice codes are less likely to have negative amplitude clipping than those design for average optical power limited channels.

5.3   Summary

In this chapter, some two-dimensional lattice codes constructed by the intersection of hexagonal lattice and bounded region under average and peak optical power constraints are presented. Performance of the modulation schemes is examined by running Monte-Carlo simulations. Average and peak optical power gain over baseline versus spectral efficiency for a $P_e \approx 10^{-6}$ using hexagonal lattice modulation schemes are analyzed and compared to previous studied works in [32].

Under average optical power constraint and without added constant bias, an approximate 2 dB average optical power gain is obtained over 16-PAM PL scheme with added DC bias for a signal space parameter $\varepsilon = 0.4$ and power efficiency $\eta \approx 5.91$. The impact of clipping distortion rises with increased ε and severely decreases the power efficiency for $\varepsilon \geq 0.5$. The clipping distortion can be reduced by adding a DC bias but with the price of higher radiated optical power. There exists a trade-off between clipping distortion and average optical power efficiency. By adding an optimal DC bias, an approximate 1.1 dB gain over 8-PAM PL scheme is obtained for $\varepsilon = 0.5$ and $\eta = 5$ and 2.1 dB gain over 16-PAM PL scheme is achieved for $\varepsilon = 0.5$ and $\eta \approx 5.93$. Compared to the non-bias scheme for $\varepsilon = 0.4$ at $\eta \approx 5.91$, an approximate 0.1 dB gain by adding optimal DC bias for $\varepsilon = 0.5$ is achieved.

Under peak optical power constraint, a more than 2 dB peak optical power gain is obtained over 16-PAM PL scheme under high spectral efficiency regime, e.g. $\eta > 6$, for a given $\varepsilon = 0.5$. Larger ε can be selected to construct lattice codes under peak optical power constraint than for the average optical power constraint.

Chapter 6

Conclusions and Future Work

6.1 Conclusions

In this thesis, a novel method is proposed for signaling on bandlimited optical intensity channels under average and peak optical power constraints. By relaxing the strict non-negativity constraint on intensity channels, a degree of freedom is added to the S2 PAM scheme to improve the power and spectral efficiency with comparison to previously studied schemes. These *essentially* non-negative and peak-limited lattice codes satisfy the channel constraints with high probability. In fact, the likelihood that the lattice codes violate channel constraints are included in the design of the signal space. A tractable numerical method based on finite series is then applied to compute the likelihood of clipping.

To compare the proposed schemes with previously designed cases, asymptotic power gains and spectral efficiencies are estimated by applying continuous approximation. Several essentially non-negative and essentially peak-limited discrete hexagonal lattice constellations are designed and their performance using clipping models

is quantified via Monte-Carlo simulations.

Under an average optical power constraint, for a given error tolerance $P_{\mathrm{e}} \approx 10^{-6}$ and $\varepsilon = 0.4$, the essentially non-negative lattice codes have more than a 2 dB optical power gain over previous approaches with gain increasing as η. The impact of clipping distortion on system performance is shown to be negligible for $\varepsilon < 0.4$. Larger ε provides more degrees of freedom efficiency but at the cost of increased negativity.

Under a peak optical power constraint and for a given ε, the likelihood of negative excursion is significantly smaller than that under an average optical power constraint with the same ε. The designed essentially peak-limited lattice codes show a significant gain in peak power gain over previous schemes which become significant at high η.

These results are especially significant for a variety of bandwidth constrained IM/DD channels which have sufficient signal-to-noise ratios to operate reliably at high spectral efficiencies. In particular, VLC channels have these features and future work includes prototyping the designed essentially non-negative and peak-limited schemes for visible light communications.

6.2　Future Work

The thesis is a starting point for multi-dimensional modulation design for bandlimited optical intensity channel. Here are some suggestions for the future work:

- How to model the clipping distortion under average and peak optical power constraints is a challenge since clipping distortion is generating due to intensity modulator and closely correlated to the electrical current signal. Finding a model to approximate clipping distortion and take it into account for maximum likelihood detection.

- The sampling receiver in the thesis is sub-optimal since no matched filter is utilized. The basis function $\phi_2(t)$ is also a root-Nyquist pulse and its corresponding matched filter can be applied. However, the cross-correlation of filter outputs must be considered and the realization complexity should be measured.

- The likelihood of clipping under average optical power constraint is periodic with period T and even symmetric about $t = (k + 1/2)T, k \in \mathbb{Z}$. A periodic non-DC bias can be added to electrical current at transmitter to reduce the clipping distortion. The additional power consumption by adding non-DC bias is required to be less than using DC bias. Finding an optimized bias to improve power efficiency over previous studied work for high spectral efficiency.

- Designing higher order dimensional signal space and modulation schemes to increase system spectral efficiency.

- All the simulations and power gain in thesis are uncoded results. Designing channel coding/decoding schemes, such as LDPC code, to improve the BER performance.

Appendix A

Variance, Skewness, and Kurtosis of X^{a} and R

This appendix presents detailed derivation of the variance, skewness and Pearson measure of kurtosis of $X^{\mathrm{a}}(q)$ and $R(q)$ applying continuous approximation for a given $q \in (0, 0.5]$ and $\varepsilon > 0$. To compute the skewness and kurtosis, closed-forms of the third and fourth central moments of $X^{\mathrm{a}}(q)$ are presented.

For notation simplicity, q is omitted hereafter. Each (a_i, b_i) is assumed to be independently and uniformly selected over the bounded region $\Upsilon_{\varepsilon} \cap \Psi^{\star}(1)$. Recall that $R = X^{\mathrm{a}} - S$, where $S = \sum_{j \in \mathcal{V}} Z_j$ and $Z_i = a_i \phi_{1,i} + b_i \phi_{2,i}$. Notice that a_i and b_i subject to triangular distributions as discussed in Chap. 4.2, their expectation and

variance can be computed via [69, 70],

$$E[a_i] = \frac{2}{3} \tag{A.1}$$

$$E[b_i] = 0 \tag{A.2}$$

$$\text{Var}[a_i] = \frac{1}{18} \tag{A.3}$$

$$\text{Var}[b_i] = \frac{\varepsilon^2}{6} \tag{A.4}$$

which will be applied throughout this appendix.

A.1   Variance of X^{a} and R

Since the variance of a sum of independent RVs is equal to the sum of variance of each individual [71, Eq.(2.16)],

$$\text{Var}[X^{\mathrm{a}}] = \sum_{i=-\infty}^{\infty} \text{Var}[Z_i] \tag{A.5}$$

$$\text{Var}[R] = \text{Var}[X^{\mathrm{a}}] - \sum_{j \in \mathcal{V}} \text{Var}[Z_j] \tag{A.6}$$

where $\{Z_i\}$ is mutual independent. The variance of Z_i can be written as

$$\text{Var}[Z_i] = \text{Var}[a_i]\,\varphi_{1,i}^2 + \text{Var}[b_i]\,\varphi_{2,i}^2 + 2\varphi_{1,i}\varphi_{2,i}\mu_{1,1}(a_i, b_i) \tag{A.7}$$

where $\mu_{1,1}(X,Y)$ is the $(1,1)$ bivariate moment about the mean $(\mathrm{E}\,[X]\,,\mathrm{E}\,[Y])$, or equivalent to the covariance of X and Y. Thus,

$$\mu_{1,1}(a_i, b_i) \;=\; \mathrm{E}\,[a_i b_i] - \mathrm{E}\,[a_i]\,\mathrm{E}\,[b_i]$$

$$=\; 0 \tag{A.8}$$

where the last step arises since $\mathrm{E}\,[b_i] = 0$ and conditional expectation equation $\mathrm{E}\,[a_i b_i] = \mathrm{E}\,[\mathrm{E}\,[a_i b_i | a_i]] = 0$. In addition, since $b_i | a_i$ is symmetrically distributed over $[-\varepsilon a_i, \varepsilon a_i]$, $\mu_{n,1}(a_i, b_i) = 0$ for any integer $n \geq 1$.

The variance of Z_i can be obtained via substituting (A.3),(A.4) and (A.8) into (A.7),

$$\mathrm{Var}\,[Z_i] = \frac{\varphi_{1,i}^2}{18} + \frac{\varepsilon^2 \varphi_{2,i}^2}{6} \quad . \tag{A.9}$$

Thus, the variance of Z_i can be simplified as

$$\mathrm{Var}\,[X^{\mathrm{a}}] = \frac{1}{18}\sum_{i=-\infty}^{\infty}\varphi_{1,i}^2 + \frac{\varepsilon^2}{6}\sum_{i=-\infty}^{\infty}\varphi_{2,i}^2 \quad . \tag{A.10}$$

The terms $\sum_{i=-\infty}^{\infty}\varphi_{1,i}^2$ and $\sum_{i=-\infty}^{\infty}\varphi_{2,i}^2$ can be obtained from poly-Gamma functions [72, Chp.6.4] [73] which take the forms :

$$\psi^{(n)}(m) = (-1)^{n+1}n!\sum_{k=0}^{\infty}(m+k)^{-n-1} \qquad m \neq 0, -1, -2, \dots$$

$$\psi^{(n)}(1-m) + (-1)^{n+1}\psi^{(n)}(m) = (-1)^n\pi\frac{d^n}{dm^n}\cot(\pi m)$$

where $\psi^{(n)}(z)$ is the n-th derivative of Digamma function $\psi(z)$. Thus,

$$\sum_{k=-\infty}^{\infty} \frac{1}{(k+m)^{n+1}} = \frac{(-1)^n \pi}{\Gamma(n+1)} \frac{d^n}{dm^n} \cot(\pi m) \tag{A.11}$$

where $\Gamma(n+1) = 1 \cdot 2 \cdot 3 \cdots (n-1)n = n!$ is the Gamma function. Summations $\sum_i (q-i)^{-2}$ and $\sum_i (q-i)^{-4}$ can be computed using (A.11),

$$\sum_{i=-\infty}^{\infty} \frac{1}{(q-i)^2} = -\pi \frac{d}{dq} \cot \pi q = \frac{\pi^2}{\sin^2 \pi q} \quad , \tag{A.12}$$

$$\sum_{i=-\infty}^{\infty} \frac{1}{(q-i)^4} = \frac{-1}{3!} \pi \frac{d^3}{dq^3} \cot \pi q$$

$$= \frac{\pi^4 \left(2 \cos^2 \pi q + 1\right)}{3 \sin^4 \pi q} \quad . \tag{A.13}$$

Using (A.12) and (A.13),

$$\sum_{i=-\infty}^{\infty} \varphi_{1,i}^2 = \frac{\sin^4 \pi q}{\pi^4} \overline{\phi}_1^2 \sum_{i=-\infty}^{\infty} \frac{1}{(q-i)^4} = \frac{2 \cos^2 \pi q + 1}{3} \overline{\phi}_1^2 \quad , \tag{A.14}$$

$$\sum_{i=-\infty}^{\infty} \varphi_{2,i}^2 = \frac{4\pi^2}{3} \frac{\sin^4 \pi q}{\pi^4} \overline{\phi}_1^2 \sum_{i=-\infty}^{\infty} \frac{1}{(q-i)^2} = \frac{4 \sin^2 \pi q}{3} \overline{\phi}_1^2 \quad . \tag{A.15}$$

Thus, substituting (A.14) and (A.15) to (A.10) ,

$$\mathrm{Var}\left[X^{\mathrm{a}}\right] = \frac{\overline{\phi}_1^2}{54} \left(2 \cos^2 \pi q + 1 + 12\varepsilon^2 \sin^2 \pi q\right) \quad . \tag{A.16}$$

Substituting (A.16) into (A.6), the variance of R takes the form as

$$\mathrm{Var}\left[R\right] = \frac{\overline{\phi}_1^2}{54} \left(2 \cos^2 \pi q + 1 + 12\varepsilon^2 \sin^2 \pi q\right) - \sum_{j \in \mathcal{V}} \frac{\phi_{1,j}^2}{18} - \sum_{j \in \mathcal{V}} \frac{\varepsilon^2 \phi_{2,j}^2}{6} \quad . \tag{A.17}$$

A.2   Skewness of X^{a} and R

Skewness is a measure of symmetry. The negative skew means the left tail of distribution is longer, or more precisely, the mass of the distribution is concentrated on the right. Similarly, the positive skew means the right tail of distribution is longer and a zero skew indicates the distribution is strictly symmetric. From definition, the skewness of X^{a} is its third standardized moment in the form as

$$\mathrm{Skew}\left[X^{\mathrm{a}}\right] = \frac{\mu_3(X^{\mathrm{a}})}{\mathrm{Var}\left[X^{\mathrm{a}}\right]^{3/2}} \tag{A.18}$$

where $\mu_3(\cdot)$ denotes the third central moment. An additivity property holds for the third central moment [74] that

$$\mu_3(A+B) = \mu_3(A) + \mu_3(B) \quad \text{provided } A, B \text{ are independent.}$$

Since $\{Z_i\}$ is mutual independent ,

$$\mu_3(X^{\mathrm{a}}) \;=\; \sum_{i=-\infty}^{\infty} \mu_3(Z_i) \tag{A.19}$$

$$\mu_3(R) \;=\; \mu_3(X^{\mathrm{a}}) - \sum_{j\in\mathcal{V}} \mu_3(Z_j) \tag{A.20}$$

where the third central moment of each Z_i can be written as the

$$\mu_3(Z_i) = \varphi_{1,i}^3 \mu_3(a_i) + \varphi_{2,i}^3 \mu_3(b_i) + 3\varphi_{1,i}^2 \varphi_{2,i} \mu_{2,1}(a_i, b_i)$$
$$+ 3\varphi_{1,i}\varphi_{2,i}^2 \mu_{1,2}(a_i, b_i) \quad . \tag{A.21}$$

Notice that $\mu_3(b_i) = 0$ since b_i has a symmetric distribution and $\mu_{2,1}(a_i, b_i) = 0$. The

third order central moment of a_i is

$$\mu_3(a_i) = \int_0^1 2a(a - \frac{2}{3})^3 da = -\frac{1}{135} \quad . \tag{A.22}$$

The term $\mu_{1,2}(a_i, b_i)$ can be calculated as follow:

$$
\begin{aligned}
\mu_{1,2}(a_i, b_i) &= \mathrm{E}\left[(a_i - \mathrm{E}\,[a_i])(b_i - \mathrm{E}\,[b_i])^2\right] \\
&= \mathrm{E}\left[a_i b_i^2\right] - \mathrm{E}\,[a_i]\,\mathrm{E}\left[b_i^2\right] \\
&= \int_0^1 \int_{-\varepsilon a}^{\varepsilon a} \frac{1}{\varepsilon} ab^2 \, db \, da - \frac{2}{3}\frac{\varepsilon^2}{6} \\
&= \frac{\varepsilon^2}{45} \quad .
\end{aligned}
\tag{A.23}
$$

Thus (A.19) can be simplified as

$$\mu_3(X^{\mathrm{a}}) = -\frac{1}{135} \sum_{i=-\infty}^{\infty} \varphi_{1,i}^3 + \frac{\varepsilon^2}{15} \sum_{i=-\infty}^{\infty} \varphi_{1,i}\varphi_{2,i}^2 \tag{A.24}$$

where

$$\sum_{i=-\infty}^{\infty} \varphi_{1,i}^3 = \bar{\phi}_1^3 \frac{\sin^6 \pi q}{\pi^6} \sum_{i=-\infty}^{\infty} \frac{1}{(q-i)^6} \quad , \tag{A.25}$$

$$\sum_{i=-\infty}^{\infty} \varphi_{1,i}\varphi_{2,i}^2 = \bar{\phi}_1^3 \frac{4\pi^2 \sin^6 \pi q}{3\pi^6} \sum_{i=-\infty}^{\infty} \frac{1}{(q-i)^4} \quad . \tag{A.26}$$

Using the same approach in Appendix. A.1, the closed-form of $\sum_i (q - i)^{-6}$ is

$$
\begin{aligned}
\sum_{i=-\infty}^{\infty} \frac{1}{(q-i)^6} &= \frac{-1}{5!}\pi \frac{d^5}{dq^5} \cot(\pi q) \\
&= \frac{\pi^6 \left(2\cos^4 \pi q + 11 \cos^2 \pi q + 2\right)}{15 \sin^6 \pi q} \quad .
\end{aligned}
\tag{A.27}
$$

Using (A.13)(A.25)(A.26)(A.27) and (A.24), the closed-form of third central moment of X^{a} is

$$\mu_3(X^{\mathrm{a}}) = \frac{\overline{\phi}_1^3}{135} \left[4\varepsilon^2 \left(1 + \cos^2 \pi q - 2\cos^4 \pi q \right) - \frac{2\cos^4 \pi q + 11\cos^2 \pi q + 2}{15} \right] \quad . \tag{A.28}$$

Thus the skewness of X^{a} can be obtained by substituting (A.28) and (A.16) into (A.18). Similarly, the third central moment of R takes the form as

$$\mu_3(R) = \mu_3(X^{\mathrm{a}}) + \frac{1}{135} \sum_{j \in \mathcal{V}} \phi_{1,j}^3 - \frac{\varepsilon^2}{15} \sum_{j \in \mathcal{V}} \phi_{1,j} \phi_{2,j}^2 \quad . \tag{A.29}$$

In addition, the skewness of R can be computed via substituting (A.17) and (A.29) into the definition

$$\mathrm{Skew}\,[R] = \frac{\mu_3(R)}{\mathrm{Var}\,[R]^{3/2}} \quad . \tag{A.30}$$

A.3   Kurtosis of X^{a} and R

Kurtosis is a descriptor of the shape of a probability distribution and there are different ways of quantifying it. In this work, the Pearson measure of kurtosis is applied and such kurtosis is defined as

$$\mathrm{Kurt}\,[X^{\mathrm{a}}] = \frac{\mu_4(X^{\mathrm{a}})}{\mathrm{Var}\,[X^{\mathrm{a}}]^2} \tag{A.31}$$

where $\mu_4(\cdot)$ is the fourth central moment operator. Unlike the case of variance and skewness, the additivity property for the sum of independent RVs does not hold for

the fourth central moment, i.e.

$$\mu_4(Z_i + Z_j) \neq \mu_4(Z_i) + \mu_4(Z_j)$$

even if Z_i and Z_j are mutual independent. Also $\varphi_{1,i}$ and $\varphi_{2,i}$ are written as $\varphi_{1,i}$ and $\varphi_{2,i}$, respectively. Expand the X^a in terms of infinite sum of Z_i,

$$
\begin{aligned}
\mu_4(X^a) =\ & \mathrm{E}\left[(Z_i - \mathrm{E}[Z_i])^4\right] \\
=\ & \sum_{i=-\infty}^{\infty} \mu_4(Z_i) + \binom{4}{3} \sum_{i=-\infty}^{\infty}\sum_{i<j}^{\infty} \mu_{3,1}(Z_i, Z_j) + \mu_{1,3}(Z_i, Z_j) \\
& + \binom{4}{2} \sum_{i=-\infty}^{\infty}\sum_{i<j}^{\infty} \mu_{2,2}(Z_i, Z_j) \\
& + \binom{4}{2}\binom{2}{1} \sum_{i=-\infty}^{\infty}\sum_{i<j}^{\infty}\sum_{j<k}^{\infty} \mu_{2,1,1}(Z_i, Z_j, Z_k) \\
& + \binom{4}{2}\binom{2}{1} \sum_{i=-\infty}^{\infty}\sum_{i<j}^{\infty}\sum_{j<k}^{\infty} \mu_{1,2,1}(Z_i, Z_j, Z_k) \\
& + \binom{4}{2}\binom{2}{1} \sum_{i=-\infty}^{\infty}\sum_{i<j}^{\infty}\sum_{j<k}^{\infty} \mu_{1,1,2}(Z_i, Z_j, Z_k) \\
& + \binom{4}{1}\binom{3}{1}\binom{2}{1} \sum_{i=-\infty}^{\infty}\sum_{i<j}^{\infty}\sum_{j<k}^{\infty}\sum_{k<l}^{\infty} \mu_{1,1,1,1}(Z_i, Z_j, Z_k, Z_l)
\end{aligned}
\tag{A.32}
$$

where $\binom{n}{r}$ denotes combination, $\mu_{i,j,k}$ and $\mu_{i,j,k,l}$ are multivariate moments which are defined as

$$
\begin{aligned}
\mu_{i,j,k}(X, Y, Z) &= \mathrm{E}\left[(X - \mathrm{E}[X])^i (Y - \mathrm{E}[Y])^j (Z - \mathrm{E}[Z])^k\right] \\
\mu_{i,j,k,l}(W, X, Y, Z) &= \mathrm{E}\left[(W - \mathrm{E}[W])^i (X - \mathrm{E}[X])^j (Y - \mathrm{E}[Y])^k (Z - \mathrm{E}[Z])^l\right]
\end{aligned}
$$

Notice that all the multivariate moment terms except for $\mu_{2,2}(Z_i, Z_j)$ in (A.32)

are zero since $\{Z_i\}$ are mutual independent. Thus the fourth central moment of X^{a} and R can be simplified as

$$\mu_4(X^{\mathrm{a}}) \;=\; \sum_{i=-\infty}^{\infty} \mu_4(Z_i) + 6 \sum_{i=-\infty}^{\infty} \sum_{i<j}^{\infty} \mu_{2,2}(Z_i, Z_j) \quad , \tag{A.33}$$

$$\mu_4(R) \;=\; \sum_{i \notin \mathcal{V}} \mu_4(Z_i) + 6 \sum_{i \notin \mathcal{V}} \sum_{i<j, j \notin \mathcal{V}} \mu_{2,2}(Z_i, Z_j) \quad . \tag{A.34}$$

For close-form of $\sum_i \mu_4(Z_i)$, since any triangularly distributed RV has a constant kurtosis $12/5$ [75] and $\mathrm{Kurt}\,[Z_i] = \mu_4(Z_i)/\mathrm{Var}\,[Z_i]^2$,

$$\begin{aligned}
\sum_{i=-\infty}^{\infty} \mu_4(Z_i) &= \sum_{i=-\infty}^{\infty} \mathrm{Kurt}\,[Z_i]\,\mathrm{Var}\,[Z_i]^2 \\
&= \frac{2}{5} \sum_{i=-\infty}^{\infty} \left[\frac{\varphi_{1,i}^4}{54} + \frac{\varepsilon^2 \varphi_{1,i}^2 \varphi_{2,i}^2}{9} + \frac{\varepsilon^4 \varphi_{2,i}^4}{6} \right] \quad .
\end{aligned} \tag{A.35}$$

Similarly, terms $\sum_i \phi_{1,i}^4$, $\sum_i \phi_{1,i}^2 \phi_{2,i}^2$, and $\sum_i \phi_{2,i}^4$ can be computed using the same approach, i.e. poly-Gamma function, as in Appendix. A.2 and A.1,

$$\begin{aligned}
\sum_{i=-\infty}^{\infty} \varphi_{1,i}^4 &= \overline{\phi}_1^4 \frac{\sin^8 \pi q}{\pi^8} \frac{(-\pi)}{7!} \frac{d^7}{dq^7} \cot \pi q \\
&= \frac{\overline{\phi}_1^4}{315} \left(4 \cos^6 \pi q + 114 \cos^4 \pi q + 180 \cos^2 \pi q + 17 \right) \quad , \tag{A.36} \\
\sum_{i=-\infty}^{\infty} \varphi_{1,i}^2 \varphi_{2,i}^2 &= \overline{\phi}_1^4 \frac{4\pi^2}{3} \frac{\sin^8 \pi q}{\pi^8} \sum_{i=-\infty}^{\infty} \frac{1}{(q-i)^6} \\
&= \frac{4 \overline{\phi}_1^4 \sin^2 \pi q}{45} \left(2 \cos^4 \pi q + 11 \cos^2 \pi q + 2 \right) \quad , \tag{A.37} \\
\sum_{i=-\infty}^{\infty} \varphi_{2,i}^4 &= \overline{\phi}_1^4 \frac{16\pi^4}{9} \frac{\sin^8 \pi q}{\pi^8} \sum_{i=-\infty}^{\infty} \frac{1}{(q-i)^4} \\
&= \frac{16 \overline{\phi}_1^4 \sin^4 \pi q}{27} \left(2 \cos^2 \pi q + 1 \right) \quad . \tag{A.38}
\end{aligned}$$

Thus, the closed-form of $\sum_i \mu_4(Zi)$ is obtained by substituting (A.36)–(A.38) into (A.35).

For computation of $\sum_{i=} \sum_{i<j} \mu_{2,2}(Z_i, Z_j)$, since Z_i and Z_j are independent,

$$
\sum_{i=-\infty}^{\infty} \sum_{i<j}^{\infty} \mu_{2,2}(Z_i, Z_j) = \sum_{i=-\infty}^{\infty} \sum_{i<j}^{\infty} \text{Var}\,[Z_i]\,\text{Var}\,[Z_j]
$$

$$
= \sum_{i=-\infty}^{\infty} \sum_{i<j}^{\infty} \frac{\varphi_{1,i}^2 \varphi_{1,j}^2}{324} + \frac{\varepsilon^2}{108}\left(\varphi_{1,i}^2 \varphi_{2,j}^2 + \varphi_{1,j}^2 \varphi_{2,i}^2\right) + \frac{\varepsilon^4 \varphi_{2,i}^2 \varphi_{2,j}^2}{36} \qquad \text{(A.39)}
$$

where

$$
\sum_{i=-\infty}^{\infty} \sum_{i<j}^{\infty} \varphi_{2,i}^2 \varphi_{2,j}^2 = \frac{\overline{\phi}_1^4 16\pi^4}{9} \frac{\sin^8 \pi q}{\pi^8} \sum_{i=-\infty}^{\infty} \sum_{i<j}^{\infty} \frac{1}{(q-i)^2(q-j)^2} \quad , \qquad \text{(A.40)}
$$

$$
\sum_{i=-\infty}^{\infty} \sum_{i<j}^{\infty} \varphi_{1,i}^2 \varphi_{2,j}^2 = \frac{\overline{\phi}_1^4 4\pi^2}{3} \frac{\sin^8 \pi q}{\pi^8} \sum_{i=-\infty}^{\infty} \sum_{i<j}^{\infty} \frac{1}{(q-i)^4(q-j)^2} \quad , \qquad \text{(A.41)}
$$

$$
\sum_{i=-\infty}^{\infty} \sum_{i<j}^{\infty} \varphi_{1,j}^2 \varphi_{2,i}^2 = \frac{\overline{\phi}_1^4 4\pi^2}{3} \frac{\sin^8 \pi q}{\pi^8} \sum_{i=-\infty}^{\infty} \sum_{i<j}^{\infty} \frac{1}{(q-i)^2(q-j)^4} \quad , \qquad \text{(A.42)}
$$

$$
\sum_{i=-\infty}^{\infty} \sum_{i<j}^{\infty} \varphi_{1,i}^2 \varphi_{1,j}^2 = \overline{\phi}_1^4 \frac{\sin^8 \pi q}{\pi^8} \sum_{i=-\infty}^{\infty} \sum_{i<j}^{\infty} \frac{1}{(q-i)^4(q-j)^4} \quad . \qquad \text{(A.43)}
$$

To compute the summations in (A.40) to (A.43), partial fraction expansion is applied. For example, let $F_1(q) = \frac{1}{(q-i)^2(q-j)^2}$ and expand it in the form as

$$
F_1(q) = \frac{C_1}{q-i} + \frac{C_2}{(q-i)^2} + \frac{C_3}{q-j} + \frac{C_4}{(q-j)^2} \qquad \text{(A.44)}
$$

where

$$
\begin{aligned}
C_1 &= \left.\frac{dF_1(q)(q-i)^2}{dq}\right|_{q=i} = \frac{-2}{(i-j)^3} \quad, \\
C_2 &= \left.F_1(q)(q-i)^2\right|_{q=i} = \frac{1}{(i-j)^2} \quad, \\
C_3 &= \left.\frac{dF_1(q)(q-j)^2}{dq}\right|_{q=j} = \frac{-2}{(j-i)^3} = -C_1 \quad, \\
C_4 &= \left.F_1(q)(q-j)^2\right|_{q=j} = \frac{1}{(j-i)^2} = C_2 \quad.
\end{aligned}
$$

Thus

$$
\begin{aligned}
\sum_{i=-\infty}^{\infty}\sum_{i<j}^{\infty}\frac{1}{(q-i)^2(q-j)^2} &= 2\sum_{i=-\infty}^{\infty}\frac{1}{(q-i)^2}\sum_{n=1}^{\infty}\frac{1}{n^2} \\
&= \frac{\pi^4}{3\sin^2 \pi q} \quad.
\end{aligned}
$$

The last step is resulted from specific value of Riemann-zeta function [76, Chp.9.54] [77–79] that

$$
\sum_{i=1}^{\infty}\frac{1}{n^2} = \frac{\pi^2}{6} \quad.
$$

Substituting (A.45) into (A.40),

$$
\sum_{i=-\infty}^{\infty}\sum_{i<j}^{\infty}\varphi_{2,i}^2\varphi_{2,j}^2 = \frac{16\overline{\phi}_1^{4}\sin^6 \pi q}{27} \quad. \tag{A.45}
$$

Similarly, let $F_2(q) = \frac{1}{(q-i)^4(q-j)^2}$ and $F_3(q) = \frac{1}{(q-i)^2(q-j)^4}$. The partial fraction expansion of $F_2(q)$ can be written as

$$
F_2(q) = \frac{C_1}{q-i} + \frac{C_2}{(q-i)^2} + \frac{C_3}{(q-i)^3} + \frac{C_4}{(q-i)^4} + \frac{C_5}{q-j} + \frac{C_6}{(q-j)^2} \tag{A.46}
$$

where

$$
\begin{aligned}
C_1 &= \frac{1}{(4-1)!}\frac{d^3}{dq^3}F_2(q)(q-i)^4\Big|_{q=i} = \frac{-4}{(i-j)^5} \quad, \\
C_2 &= \frac{1}{(4-2)!}\frac{d^2}{dq^2}F_2(q)(q-i)^4\Big|_{q=i} = \frac{3}{(i-j)^4} \quad, \\
C_3 &= \frac{d}{dq}F_2(q)(q-i)^4\Big|_{q=i} = \frac{-2}{(i-j)^3} \quad, \\
C_4 &= F_2(q)(q-i)^4\Big|_{q=i} = \frac{1}{(i-j)^2} \quad, \\
C_5 &= \frac{d}{dq}F_2(q)(q-j)^2\Big|_{q=j} = \frac{-4}{(j-i)^5} \quad, \\
C_6 &= F_2(q)(q-j)^2\Big|_{q=i} = \frac{1}{(j-i)^4} \quad.
\end{aligned}
$$

Notice that the partial fraction expansion of $F_3(q)$ can be obtained directly through swapping i and j in (A.46). Thus,

$$
\sum_{i=-\infty}^{\infty}\sum_{i<j}^{\infty} \frac{1}{(q-i)^4(q-j)^2} + \frac{1}{(q-j)^4(q-i)^2}
$$
$$
= 2\left(\sum_{i=-\infty}^{\infty}\frac{1}{(q-i)^2}\sum_{n=1}^{\infty}\frac{4}{n^4} + \sum_{i=-\infty}^{\infty}\frac{1}{(q-i)^4}\sum_{n=1}^{\infty}\frac{1}{n^2} \right) \quad.
$$

Similarly, using the same approach as to obtain (A.45), it can be shown that

$$
\sum_{i=-\infty}^{\infty}\sum_{i<j}^{\infty} \varphi_{1,i}^2\varphi_{2,j}^2 + \varphi_{1,j}^2\varphi_{2,i}^2 = \frac{8\bar{\phi}_1^4 \sin^4 \pi q}{3}\left(\frac{2\sin^2 \pi q}{45} + \frac{2\cos^2 \pi q + 1}{18} \right) \quad,\text{(A.47)}
$$
$$
\sum_{i=-\infty}^{\infty}\sum_{i<j}^{\infty} \varphi_{1,i}^2\varphi_{1,j}^2 = 2\bar{\phi}_1^4\left(\frac{2\sin^6 \pi q}{189} + \frac{(1+2\cos^2 \pi q)\sin^4 \pi q}{270} \right) \quad.\text{(A.48)}
$$

Using (A.31) and (A.35)–(A.48), the closed-form of kurtosis of X^{a} is obtained. Notice that it is complicated to compute the closed-form of $\mu_4(R)$ due to non-additivity

property of fourth central moment. However, it is simple to numerically compute the fourth central moment of a truncated residual sum, R_{N_T} using (A.34). Thus, an approximation of Kurt $[R]$ via

$$\mathrm{Kurt}\,[R] \approx \frac{\mu_4(R_{N_\mathrm{T}})}{\mathrm{Var}\,[R_{N_\mathrm{T}}]^{3/2}} \quad . \tag{A.49}$$

Bibliography

[1] V. W. Chan, "Free-space optical communications," *J. Lightw. Technol.*, vol. 24, no. 12, pp. 4750–4762, Dec. 2006.

[2] E. Ip, A. P. T. Lau, D. J. Barros, and J. M. Kahn, "Coherent detection in optical fiber systems," *Opt. Express*, vol. 16, no. 2, pp. 753–791, 2008.

[3] J. Kahn, "Modulation and detection techniques for optical communication systems," in *Optical Amplifiers and Their Applications/Coherent Optical Technologies and Applications, Technical Digest.* Optical Society of America, 2006, p. CThC1.

[4] ——, "1 Gbit/s PSK homodyne transmission system using phase-locked semiconductor lasers," *IEEE Photon. Technol. Lett.*, vol. 1, no. 10, pp. 340–342, Oct. 1989.

[5] J. Kahn, A. Gnauck, J. Veselka, S. Korotky, and B. Kasper, "4-Gb/s PSK homodyne transmission system using phase-locked semiconductor lasers," *IEEE Photon. Technol. Lett.*, vol. 2, no. 4, pp. 285–287, Apr. 1990.

[6] S. Norimatsu, K. Iwashita, and K. Noguchi, "An 8 Gb/s qpsk optical homodyne detection experiment using external-cavity laser diodes," *IEEE Photon. Technol. Lett.*, vol. 4, no. 7, pp. 765–767, Jul. 1992.

[7] A. Nahata, D. H. Auston, T. F. Heinz, and C. Wu, "Coherent detection of freely propagating terahertz radiation by electro-optic sampling," *Appl. Phys. Lett.*, vol. 68, no. 2, pp. 150–152, 1996.

[8] L. G. Kazovsky, G. Kalogerakis, and W.-T. Shaw, "Homodyne phase-shift-keying systems: past challenges and future opportunities," *J. Lightwave Technol.*, vol. 24, no. 12, pp. 4876–4884, Jun. 2006.

[9] C. Cox, E. Ackerman, R. Helkey, and G. E. Betts, "Techniques and performance of intensity-modulation direct-detection analog optical links," *IEEE Trans. Microw. Theory Tech.*, vol. 45, no. 8, pp. 1375–1383, Aug. 1997.

[10] S. C. J. Lee, S. Randel, F. Breyer, and A. M. Koonen, "PAM-DMT for intensity-modulated and direct-detection optical communication systems," *IEEE Photon. Technol. Lett.*, vol. 21, no. 23, pp. 1749–1751, Dec. 2009.

[11] H. Burchardt, N. Serafimovski, D. Tsonev, S. Videv, and H. Haas, "VLC: Beyond point-to-point communication," *IEEE Commun. Mag.*, vol. 52, no. 7, pp. 98–105, July 2014.

[12] Y. Tanaka, T. Komine, S. Haruyama, and M. Nakagawa, "Indoor visible light data transmission system utilizing white LED lights," *IEICE Trans. Commun.*, vol. 86, no. 8, pp. 2440–2454, Aug. 2003.

[13] T. Komine and M. Nakagawa, "Fundamental analysis for visible-light communication system using LED lights," *IEEE Trans. Consum. Electron.*, vol. 50, no. 1, pp. 100–107, Feb. 2004.

[14] H. Elgala, R. Mesleh, and H. Haas, "An LED model for intensity-modulated optical communication systems," *IEEE Photon. Technol. Lett.*, vol. 22, no. 11, pp. 835–837, June 2010.

[15] D. C. O'Brien, L. Zeng, H. Le-Minh, G. Faulkner, J. W. Walewski, and S. Randel, "Visible light communications: Challenges and possibilities," in *2008 IEEE 19th Int. Symp. Personal, Indoor and Mobile Radio Communications (PIMRC)*. IEEE, 2008, pp. 1–5.

[16] F. R. Gfeller and U. Bapst, "Wireless in-house data communication via diffuse infrared radiation," *Proc. IEEE*, vol. 67, no. 11, pp. 1474–1486, Nov. 1979.

[17] G. W. Marsh and J. M. Kahn, "50-Mb/s diffuse infrared free-space link using on-off keying with decision-feedback equalization," *IEEE Photonics Technol. Lett.*, vol. 6, no. 10, pp. 1268–1270, Oct. 1994.

[18] J. M. Kahn, W. J. Krause, and J. B. Carruthers, "Experimental characterization of non-directed indoor infrared channels," *IEEE Trans. Commun.*, vol. 43, no. 2/3/4, pp. 1613–1623, Feb./Mar./Apr. 1995.

[19] J. M. Kahn and J. R. Barry, "Wireless infrared communications," *Proc. IEEE*, vol. 85, no. 2, pp. 265–298, Feb. 1997.

[20] W. O. Popoola and Z. Ghassemlooy, "BPSK subcarrier intensity modulated free-space optical communications in atmospheric turbulence," *J. Lightw. Technol.*, vol. 27, no. 8, pp. 967–973, Apr. 2009.

[21] A. A. Farid and S. Hranilovic, "Outage capacity optimization for free-space optical links with pointing errors," *J. Lightw. Technol.*, vol. 25, no. 7, pp. 1702–1710, Jul. 2007.

[22] X. Zhu and J. M. Kahn, "Free-space optical communication through atmospheric turbulence channels," *IEEE Trans. Commun.*, vol. 50, no. 8, pp. 1293–1300, Aug. 2002.

[23] M. S. Moreolo, R. Muñoz, and G. Junyent, "Novel power efficient optical OFDM based on Hartley transform for intensity-modulated direct-detection systems," *J. Lightwave Technol.*, vol. 28, no. 5, pp. 798–805, Mar. 2010.

[24] D.-Z. Hsu, C.-C. Wei, H.-Y. Chen, W.-Y. Li, and J. Chen, "Cost-effective 33-Gbps intensity modulation direct detection multi-band OFDM LR-PON system employing a 10-Ghz-based transceiver," *Opt. Express*, vol. 19, no. 18, pp. 17 546–17 556, Sept. 2011.

[25] H. Park and J. R. Barry, "Modulation analysis for wireless infrared communications," in *1995 IEEE International Conference on Communications (ICC), Seattle,'Gateway to Globalization'*, vol. 2.   IEEE, 1995, pp. 1182–1186.

[26] S. Hranilovic and F. R. Kschischang, "Optical intensity-modulated direct detection channels: signal space and lattice codes," *IEEE Trans. Inf. Theory*, vol. 49, no. 6, pp. 1385–1399, June 2003.

[27] W. Mao and J. M. Kahn, "Lattice codes for amplified direct-detection optical systems," *IEEE Trans. Commun.*, vol. 56, no. 7, pp. 1137–1145, July 2008.

[28] J. Karout, E. Agrell, and M. Karlsson, "Power efficient subcarrier modulation for intensity modulated channels," *Opt. Express*, vol. 18, no. 17, pp. 17 913–17 921, Sept. 2010.

[29] J. Karout, E. Agrell, K. Szczerba, and M. Karlsson, "Optimizing constellations for single-subcarrier intensity-modulated optical systems," *IEEE Trans. Inf. Theory*, vol. 58, no. 7, pp. 4645–4659, 2012.

[30] J. Karout, G. Kramer, F. R. Kschischang, and E. Agrell, "A two-dimensional signal space for intensity-modulated channels," *IEEE Commun. Lett.*, vol. 16, no. 9, pp. 1361–1364, Sept. 2012.

[31] S. Hranilovic, "Minimum-bandwidth optical intensity Nyquist pulses," *IEEE Trans. Commun.*, vol. 55, no. 3, pp. 574–583, Mar. 2007.

[32] M. Tavan, E. Agrell, and J. Karout, "Bandlimited intensity modulation," *IEEE Trans. Commun.*, vol. 60, no. 11, pp. 3429–3439, Nov. 2012.

[33] C. B. Czegledi, M. R. Khanzadi, and E. Agrell, "Bandlimited power-efficient signaling and pulse design for intensity modulation," *IEEE Trans. Commun.*, vol. 62, no. 9, pp. 3274–3284, 2014.

[34] D. Zhang and S. Hranilovic, "A two-dimensional signal space for bandlimited optical intensity channels," in *2015 IEEE Int. Conf. Commun. Workshop (ICCW)*, June 2015, pp. 1404–1409.

[35] ——, "Bandlimited Optical Intensity Modulation under Average and Peak Power Constraints," manuscript submitted Feb. 2016 to IEEE Transaction on Communications.

[36] D. Jagerman and L. Fogel, "Some general aspects of the sampling theorem," *IRE Trans. Inf. Theory*, vol. 2, no. 4, pp. 139–146, 1956.

[37] A. Papoulis, "Generalized sampling expansion," *IEEE Trans. Circuits Syst.*, vol. 24, no. 11, pp. 652–654, Nov. 1977.

[38] H. Nyquist, "Certain topics in telegraph transmission theory," *Trans. American Institute Electrical Engineers*, vol. 47, no. 2, pp. 617–644, Apr. 1928.

[39] J. Grubor, S. Randel, K.-D. Langer, and J. W. Walewski, "Broadband information broadcasting using LED-based interior lighting," *IEEE/OSA J. Lightw. Technol.*, vol. 26, no. 24, pp. 3883–3892, Dec. 2008.

[40] H. Elgala, R. Mesleh, and H. Haas, "A study of LED nonlinearity effects on optical wireless transmission using ofdm," in *IFIP Int. Conf. Wireless Opt. Commun. Netw.* IEEE, Apr. 2009, pp. 1–5.

[41] B. Inan, S. Jeffrey Lee, S. Randel, I. Neokosmidis, A. M. Koonen, and J. W. Walewski, "Impact of LED nonlinearity on discrete multitone modulation," *IEEE J. Opt. Commun. Netw.*, vol. 1, no. 5, pp. 439–451, Oct. 2009.

[42] H. Qian, S. Cai, S. Yao, T. Zhou, Y. Yang, and X. Wang, "On the benefit of DMT modulation in nonlinear VLC systems," *Opt. Express*, vol. 23, no. 3, pp. 2618–2632, Feb. 2015.

[43] M. S. Mossaad, S. Hranilovic, and L. Lampe, "Visible light communications using OFDM and multiple LEDs," *IEEE Trans. Commun.*, vol. 63, no. 11, pp. 4304–4313, Nov. 2015.

[44] A. V. Oppenheim and A. S. Willsky, *Signals and Systems.* Prentice Hall, 1997.

[45] M. Plancherel and M. Leffler, "Contribution à l'étude de la représentation d'une fonction arbitraire par des intégrales définies," *Rendiconti del Circolo Matematico di Palermo*, vol. 30, no. 1, pp. 289–335, 1910.

[46] K. Yosida, *Functional analysis*, 6th ed. Springer-Verlag, 1980, ch. VI, pp. 151–155.

[47] Wikipedia, "Plancherel theorem," https://en.wikipedia.org/wiki/Plancherel_theorem.

[48] J. R. Barry, E. A. Lee, and D. G. Messerschmitt, *Digital communication.* Springer Science & Business Media, 2004.

[49] G. D. Forney Jr and L.-F. Wei, "Multidimensional constellations. i. introduction, figures of merit, and generalized cross constellations," *IEEE J. Sel. Areas Commun.*, vol. 7, no. 6, pp. 877–892, 1989.

[50] G. D. Forney Jr, R. G. Gallager, G. R. Lang, F. M. Longstaff, and S. U. Qureshi, "Efficient modulation for band-limited channels," *IEEE J. Select. Areas Commun.*, vol. 2, no. 5, pp. 632–647, Sept. 1984.

[51] A. R. Calderbank and L. H. Ozarow, "Nonequiprobable signaling on the gaussian channel," *IEEE Trans. Inform. Theory*, vol. 36, no. 4, pp. 726–740, July 1990.

[52] F. R. Kschischang and S. Pasupathy, "Optimal nonuniform signaling for Gaussian channels," *IEEE Trans. Inform. Theory*, vol. 39, no. 3, pp. 913–929, May 1993.

[53] M. Gardner, "The binary Gray code," *Knotted Doughnuts and Other Mathematical Entertainments*, pp. 11–27, 1986.

[54] W. Hoeffding, "Probability inequalities for sums of bounded random variables," *J. Amer. Statist. Assoc.*, vol. 58, no. 301, pp. 13–30, 1963.

[55] N. C. Beaulieu, "An infinite series for the computation of the complementary probability distribution function of a sum of independent random variables and its application to the sum of rayleigh random variables," *IEEE Trans. Commun.*, vol. 38, no. 9, pp. 1463–1474, Sept. 1990.

[56] D. Johnson, "The triangular distribution as a proxy for the beta distribution in risk analysis," *Journal of the Royal Statistical Society: Series D (The Statistician)*, vol. 46, no. 3, pp. 387–398, 1997.

[57] S. Kotz and J. R. Van Dorp, *Other Continuous Families of Distributions with Bounded Support and Applications.* World Scientific, 2004.

[58] C. Walck, "Handbook on statistical distributions for experimentalists," 2007, available at http://www.fysik.su.se/~walck/suf9601.pdf.

[59] C. M. Grinstead and J. L. Snell, *Introduction to Probability.* American Mathematical Soc., 2012.

[60] I. R. Savage, "Probability inequalities of the Tchebycheff type," *Journal of Research of the National Bureau of Standards-B. Mathematics and Mathematical Physics B*, vol. 65B, no. 3, pp. 211–222, 1961.

[61] K. Krishnan, "A simple result in quadrature," *Nature*, vol. 162, no. 4110, pp. 215–215, 1948.

[62] B. Bhattacharyya, "One sided Chebyshev inequality when the first four moments are known," *Communications in Statistics-Theory and Methods*, vol. 16, no. 9, pp. 2789–2791, 1987.

[63] J. Shohat, "Inequalities for moments of frequency functions and for various statistical constants," *Biometrika*, vol. 21, no. 1/4, pp. 361–375, Dec. 1929.

[64] S. Boucheron, G. Lugosi, and P. Massart, *Concentration inequalities: A nonasymptotic theory of independence.* Oxford University Press, Oxford, 2013.

[65] "Mathematica 8.0," Wolfram Research, Inc., Champaign, Illinois, 2010. [Online]. Available: https://www.wolfram.com

[66] J. R. van Dorp and S. Kotz, "Generalized trapezoidal distributions," *Metrika*, vol. 58, no. 1, pp. 85–97, Aug. 2003.

[67] N. C. Beaulieu and M. O. Damen, "Parametric construction of Nyquist-I pulses," *IEEE Trans. Commun.*, vol. 52, no. 12, pp. 2134–2142, Dec. 2004.

[68] "Matlab version 8.1.0.604 (R2013a)," The MathWorks, Inc., Natick, Massachusetts, 2013. [Online]. Available: http://www.mathworks.com/products/matlab

[69] C. Forbes, M. Evans, N. Hastings, and B. Peacock, *Statistical distributions*, 4th ed.   John Wiley & Sons, 2010, ch. 44, pp. 189–190.

[70] Wikipedia, "Triangular distribution." [Online]. Available: \url{https://en.wikipedia.org/wiki/Triangular_distribution}

[71] S. M. Ross, *Introduction to Probability Models*, 9th ed.   Academic press, 2007.

[72] M. Abramowitz, I. A. Stegun *et al.*, *Handbook of mathematical functions*.   Dover New York, 1972, vol. 1, no. 5.

[73] T. Fujita, Y. Yano *et al.*, "Special values of the Hurwitz zeta function via generalized Cauchy variables," *Kyoto Journal of Mathematics*, vol. 52, no. 3, pp. 465–477, 2012.

[74] Wikipedia, "Central moment." [Online]. Available: \url{https://en.wikipedia.org/wiki/Central_moment}

[75] E. W. Weisstein, "Triangular distribution," http://mathworld.wolfram.com/TriangularDistribution.html.

[76] A. Jeffrey and D. Zwillinger, *Table of integrals, series, and products*.   Academic Press, 2007.

[77] Wikipedia, "Particular values of Riemann zeta function," https://en.wikipedia.org/wiki/Particular_values_of_Riemann_zeta_function.

[78] R. J. Dwilewicz and J. Mináč, "Values of the Riemann zeta function at integers," *Materials matemàtics*, vol. 26, no. 6, pp. 1–26, Nov. 2009.

[79] D. Zagier, "Values of zeta functions and their applications," in *First European Congress of Mathematics Paris, July 6–10, 1992.*   Springer, 1994, pp. 497–512.